

Stress Corrosion Crack Detection in Alloy 600  
in High Temperature Caustic

by

Bruce W. Brisson

B.S. Mechanical Engineering  
Syracuse University

SUBMITTED TO THE DEPARTMENT OF NUCLEAR ENGINEERING IN PARTIAL  
FULFILLMENT OF THE REQUIREMENTS FOR THE DEGREE OF

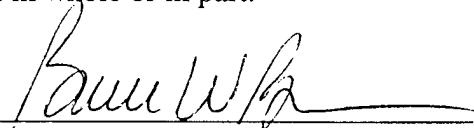
NUCLEAR ENGINEER  
and  
MASTER OF SCIENCE IN NUCLEAR ENGINEERING  
AT THE  
MASSACHUSETTS INSTITUTE OF TECHNOLOGY

JUNE 1996

© 1996 Bruce W. Brisson. All Rights Reserved.

The author hereby grants to MIT permission to reproduce and to distribute publicly paper and  
electronic copies of this thesis document in whole or in part.

Signature of Author: \_\_\_\_\_



Department of Nuclear Engineering  
May 2, 1996

Certified By: \_\_\_\_\_



R.G. Ballinger  
Associate Professor of Nuclear Engineering  
Thesis Supervisor

Certified By: \_\_\_\_\_



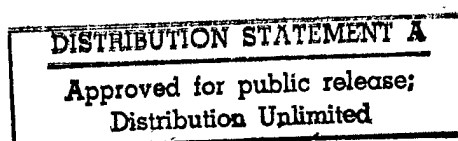
R. M. Latanision  
Professor of Materials Science and Engineering  
Thesis Reader

Accepted By: \_\_\_\_\_

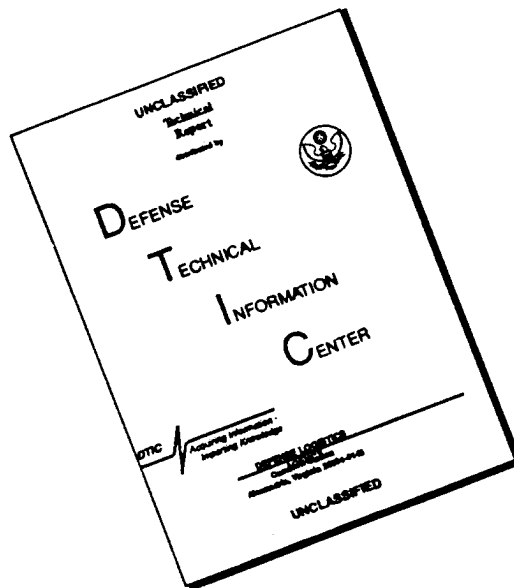
J. P. Freidberg  
Professor of Nuclear Engineering  
Chairman, Committee for Graduate Students

DTIC QUALITY INSPECTED 3

19960910 136



# DISCLAIMER NOTICE



THIS DOCUMENT IS BEST QUALITY AVAILABLE. THE COPY FURNISHED TO DTIC CONTAINED A SIGNIFICANT NUMBER OF PAGES WHICH DO NOT REPRODUCE LEGIBLY.

# Stress Corrosion Crack Detection in Alloy 600 In High Temperature Caustic

by

Bruce William Brisson

Submitted to the Department of Nuclear Engineering  
on May 1996 in partial fulfillment of the  
Requirements for the Degree of Nuclear Engineer and  
Master of Science in Nuclear Engineering

## Abstract

Alloy 600, the material used for pressurized water reactor steam generator tubing, is susceptible to environmentally assisted stress corrosion cracking. Intergranular stress corrosion cracking (IGSCC) attacks the tubes in areas of high residual stress, and in crevice regions. No method has been successfully developed to monitor steam generator tubing in-situ for crack initiation and growth. Essentially all available published IGSCC crack growth data for alloy 600 is based on non-tubing material. Although it is very likely that the current data base is applicable to tubing processing, differences between tube and other geometries make a comparison between tubing and other data important for verification purposes. However, obtaining crack initiation and growth data from tubing is difficult due to the geometry and the thin wall thickness.

In this research the goal was to develop a system to monitor crack initiation and growth under in-situ steam generator conditions in tubing and, having developed such a system, to then obtain data on actual alloy 600 tubing for comparison to published results for non-tubing material.

A nickel autoclave system capable of testing pressurized tube samples was constructed. The system is capable of operating in either recirculating or static mode as assembled. The operating environment was 10% NaOH (with 0.1%  $\text{Na}_2\text{CO}_3$  added) with a hydrogen over-pressure. The test sample was internally pressurized and electrically isolated from the rest of the system. Crack initiation and growth was monitored using an alternating current potential drop (ACPD) method especially developed for this purpose. Sample polarization to +150mV with respect to nickel was imposed to accelerate crack initiation.

Mill annealed alloy 600 tubing was chosen as the test material. A special heat of material, fabricated for industry-wide research by the Electric Power Research Institute was used. The material, heat 96834, was mill annealed at  $927 \pm 14^\circ\text{C}$ .

The program was divided into two phases: (1) system/methods development, and (2) crack growth measurement.

A multi-frequency ACPD system was developed for the detection of initiation and propagation of short cracks in alloy 600 tubing in high temperature caustic environments typical of an operating steam generator tube to tube sheet crevice. The system was then used to monitor crack initiation and growth in alloy 600 tubing.

Limited IGSCC crack growth data for the tube samples was obtained. Average values of  $K_I$  ranged from 4.2 to 17.7 MPa $\sqrt{\text{m}}$  with growth rates from 1.6 to 12.3 mm/yr.

The data obtained compare well with other, non-tubing, data in the sense that there is overlap between the data from this program and the general body of data in the literature. However, the data developed here indicates (limited as the data is) that a power law dependence of crack growth rate on  $K$  may be appropriate. The general body of literature data is too scattered to show any such dependence.

Thesis Supervisor: Ronald Ballinger

Title: Associate Professor of Nuclear Engineering and Materials Science and Engineering

## Acknowledgments

I cannot sufficiently express my gratitude for the material support and advice given by numerous companies and individuals in constructing and operating the equipment for this thesis. I would especially like to thank the Electric Power Research Institute and Dr. McIlree for their generous financial support and advice, Peter Stahle, our lab engineer, for his expertise and guidance in the many disciplines it required to make things go, and Dr. Hui Au for his technical expertise in software development.

I extend my sincere thanks and gratitude to Professor Ronald Ballinger, my thesis advisor, for his guidance and persistent encouragement that "things really would work". Without his expertise and constant remedies to apparent dead ends, this thesis would not have been possible.

Finally, I would like to dedicate this work to my wife Mary and my father, Marcel:

To Mary, I owe an unpayable debt for her constant encouragement, endless hours proof reading my papers and thesis, and somehow managing our four small children when I needed to study, write or stay at the lab late. I will never forget the love and support.

To my father, Marcel, who encouraged me from first grade on and was always there when I needed him, but passed away before I started at MIT, Thanks Dad.

## Table of Contents

ABSTRACT .....	2
ACKNOWLEDGMENTS .....	4
TABLE OF CONTENTS .....	5
LIST OF FIGURES .....	7
LIST OF TABLES .....	10
1. INTRODUCTION .....	11
2. BACKGROUND .....	14
2.1 Nuclear Steam Generator Materials and Environment .....	14
2.1.1 Steam Generator Construction .....	14
2.1.2 Steam Generator Chemistry.....	16
2.1.3 Material Properties of Alloy 600 Steam Generator Tubes...	18
2.2 Stress Corrosion Cracking Theories .....	22
2.2.1 Film Rupture Theory for Crack Initiation.....	22
2.2.2 Crack Propagation by Anodic Dissolution.....	26
2.2.3 Crack Propagation by Microvoid Formation.....	28
2.2.4 Impurities in Secondary Steam Generator Water.....	30
2.3 Role of Inhibitors .....	32
2.4 Crack Measurement by Potential Drop Methods .....	34
2.4.1 Theory of DC Potential Drop.....	34
2.4.2 Theory of AC Potential Drop.....	36
2.5 Present Research .....	43
3. EXPERIMENTAL APPARATUS .....	45
3.1 Mechanical System Description .....	45
3.1.1 Autoclave and Heating System.....	47
3.1.2 Recirculation Loop.....	48
3.1.3 Static System.....	49
3.1.4 Sample Pressurization System.....	50
3.2 Control Systems .....	51
3.3 Safety Systems .....	52
3.4 Test Sample .....	54

3.4.1 Material.....	54
3.4.2 Sample Construction.....	57
3.5 Alternating Current Potential Drop (ACPD) System .....	58
<b>4. EXPERIMENTAL PROCEDURE .....</b>	<b>61</b>
4.1 ACPD Proof of Principle Testing .....	61
4.2 Crack Initiation and Growth Measurements .....	68
<b>5. RESULTS .....</b>	<b>70</b>
5.1 ACPD Proof of Principle Testing .....	70
5.2 Crack Initiation and Growth Measurements .....	78
<b>6. DISCUSSION .....</b>	<b>88</b>
6.1 ACPD Proof of Principle .....	88
6.2 Crack Growth Rates .....	91
<b>7. CONCLUSIONS .....</b>	<b>95</b>
<b>8. FUTURE WORK .....</b>	<b>96</b>
<b>REFERENCES .....</b>	<b>97</b>
<b>A-1. SYSTEM OPERATING CHARACTERISTICS .....</b>	<b>101</b>
A-1-1 Omega CN9000A Heater Controller Parameter Settings .....	101
A-1-2 Heatup Plots .....	103
A-1-3 Autoclave Head Seal Ring Failures .....	104
<b>A-2. OPERATING PROCEDURES .....</b>	<b>106</b>
A-2-1 System Start-up Procedure - Static Operation .....	107
A-2-2 System Start-up Procedure - Recirculation .....	110
A-2-3 System Shutdown Procedure - Static Operation .....	113
A-2-4 System Shutdown Procedure - Recirculation .....	114
A-2-5 Emergency Shutdown Procedures .....	115
A-2-6 Sample Pressurization System Operation .....	116
A-2-7 Injection System Operation .....	118
A-2-8 Electroless Nickel Plating Technique .....	119
<b>A-3. DETAILED SYSTEM DRAWINGS .....</b>	<b>121</b>
<b>A-4. AXIAL FATIGUE PRE-CRACK SAMPLE PREPARATION PROCEDURE .</b>	<b>142</b>
<b>A-5. ERROR ANALYSIS .....</b>	<b>146</b>

## List of Figures

2-1	TYPICAL AREAS OF STEAM GENERATOR TUBE FAILURE BY STRESS CORROSION ATTACK .....	15
2-2	EVANS DIAGRAM FOR ALLOY 600 SHOWING THE EFFECT OF CHROMIUM CONCENTRATION ON CORROSION CURRENT DENSITY AND PASSIVITY .....	20
2-3	SCHEMATIC OF A STEAM GENERATOR TUBE SHOWING TYPICAL AREAS OF HIGH RESIDUAL STRESS .....	25
2-4	TUBULAR CONDUCTOR .....	38
2-5	CURRENT DENSITY AS A FUNCTION OF DISTANCE FROM THE EXTERIOR WALL OF A TUBULAR CONDUCTOR FOR VARIOUS VALUES OF $\beta_B$ .....	39
2-6	"INDUCTIVE COIL" SETUP BY PICK-UP WIRES ON THE TUBE .....	41
3-1	AUTOClave SYSTEM SHOWING RECIRCULATION, STATIC AND PRESSURIZATION SYSTEMS .....	46
3-2	AUTOClave WITH HEATING MANTLE SHOWING RECIRCULATION AND STATIC CONNECTIONS .....	47
3-3	INTERLOCK CONTROL SYSTEM SCHEMATIC .....	53
3-4	EDX OF ALLOY 600 HEAT 96834 (LOW TEMPERATURE ANNEAL) .....	56
3-5	THREE DIMENSIONAL SEM MICROGRAPH OF HEAT 96834 .....	56
3-6	HEAT 96834 SEM MICROGRAPH SHOWING INTRAGRANULAR PRECIPITATES .....	57
3-7	SIMPLIFIED SCHEMATIC OF TEST SAMPLES ILLUSTRATING MACHINING DIFFERENCES IN THE TUBE SECTIONS .....	58
3-8	ACPD TEST STAND .....	59
3-9	ACPD SYSTEM SCHEMATIC .....	60
4-1	WELDED TEST SAMPLE .....	61
4-2	SCHEMATIC OF SAMPLE TUBE INSTALLED INTO AUTOClave HEAD .....	63
4-3	SAMPLE ASSEMBLED INTO AUTOClave HEAD SHOWING ACPD INPUT AND OUTPUT WIRES, THERMOCOUPLE, LEVEL SENSING AND NICKEL REFERENCE ELECTRODE .....	64
4-4	POLARIZATION CURVE FOR ALLOY 600 AT 300°C IN 10% NAOH .....	67
5-1	POTENTIAL DROP FOR THE TEST AND REFERENCE AREAS .....	71
5-2	SAMPLE TEMPERATURE AND WALL STRESS (PERCENT OF 0.2% YIELD STRESS) .....	71
5-3	TEST AREA POTENTIAL DROP NORMALIZED WITH RESPECT TO THE REFERENCE AREA FOR FIGURE 5-2 .....	72



5-4	SAMPLE TEMPERATURE AND WALL STRESS (PERCENT OF 0.2% YIELD STRESS) . . . . .	73
5-5	POTENTIAL DROP FOR TEST AND REFERENCE AREAS . . . . .	74
5-6	NORMALIZED POTENTIAL DROP FOR FIGURE 5-5 . . . . .	74
5-7	STEREOSCOPIC COMPOSITE OF SAMPLE SURFACE SHOWING CRACK EMANATING FROM BENEATH THE REFERENCE AREA PROBE . . . . .	75
5-8	SEM COMPOSITE MICROGRAPH OF THE REFERENCE AREA FRACTURE SURFACE . . . . .	75
5-9	SEM COMPOSITE MICROGRAPH OF THE OPPOSITE SIDE OF THE REFERENCE AREA FRACTURE SURFACE . . . . .	76
5-10	SEM MICROGRAPH OF REGION 1 CLEARLY SHOWING IGSCC IN THIS REGION . . . . .	76
5-11	SEM MICROGRAPH OF AREA 2 SHOWING DUCTILE FAILURE REGION . . . . .	77
5-12	DUCTILE-IGSCC TRANSITION REGION . . . . .	77
5-13	SEM COMPOSITE MICROGRAPH OF IGSCC FRACTURE SURFACE SHOWING ELLIPTICAL CRACK FRONTS . . . . .	79
5-14	NORMALIZED ACPD FOR SAMPLE SHOWING CRACK INITIATION TIME BASED ON INCREASING 10KHZ POTENTIAL DROP . . . . .	79
5-15	SCHEMATIC OF TUBE SAMPLES WITH FATIGUE PRE-CRACKS IN TEST AREA . . . . .	80
5-16	SAMPLE TEMPERATURE AND APPLIED WALL STRESS (PERCENT OF 0.2% YIELD STRESS) . . . . .	81
5-17	POTENTIAL DROP VERSUS TIME FOR TEST AND REFERENCE AREAS . . . . .	82
5-18	STEREO MICROSCOPE IMAGE OF THE THROUGH-WALL CRACK SEEN AT THE BASE OF THE MACHINED NOTCH . . . . .	83
5-19	LOW POWER STEREO MICROSCOPE IMAGE SHOWING THE RELATIVE POSITION OF THE THROUGH WALL CRACK TO THE PROBES . . . . .	83
5-20	NORMALIZED POTENTIAL DROP (TEST AREA WITH RESPECT TO THE REFERENCE AREA) SHOWING AN INCREASING SIGNAL FROM THE ONSET OF TESTING . . . . .	84
5-21	SEM COMPOSITE MICROGRAPH OF FRACTURE SURFACE CLEARLY SHOWING AREA OF IGSCC . . . . .	85
5-22	MAGNIFIED SEM MICROGRAPH OF IGSCC AREA OUTLINING TWO POSSIBLE CRACK GROWTH AREAS . . . . .	85
5-23	MICROGRAPH OF THE PRE-FATIGUE AREA . . . . .	86
5-24	MICROGRAPH OF THE DUCTILE FAILURE REGION . . . . .	86
5-25	MICROGRAPH SHOWING THE PRE-FATIGUE TO IGSCC TRANSITION REGION . . . . .	86

6-1	CALCULATED POTENTIAL DROP VERSUS ACTUAL .....	90
6-2	CALCULATED POTENTIAL DROP VERSUS ACTUAL .....	90
6-3	ALLOY 600 TUBE CRACK GROWTH VERSUS STRESS INTENSITY FROM PHASE TWO TESTING .....	91
6-4	COMPARISON OF CRACK GROWTH DATA VERSUS STRESS INTENSITY (K) .....	93
6-5	ALLOY 600 CRACK GROWTH RATES VERSUS PH .....	94
A-1-1	HEATUP 950726 SHOWING OSCILLATIONS OF THE HEATER CONTROLLER .....	102
A-1-2	HEATUP PLOT SHOWING CONTRAST IN TIME BETWEEN RECIRCULATION AND STATIC MODES .....	103
A-1-3	CHANNEL IN O-RING FROM TEST 950703 .....	104
A-1-4	EROSION DAMAGE TO O-RING FROM TEST 950403.....	104
A-3-1	ALLOY 600 TEST SYSTEM .....	122
A-3-2	SAMPLE PRESSURIZATION CONTROL BOARD TUBING AND TEMPLATE DETAILS .....	123
A-3-3	RECIRCULATION AND STATIC SYSTEM CONTROL BOARD TUBING AND TEMPLATE DETAILS .....	124
A-3-4	ALLOY 600 TEST PLATFORM SCHEMATIC .....	125
A-3-5	SAMPLE PRESSURIZATION SYSTEM COMPONENT ID.....	127
A-3-6	STATIC SYSTEM COMPONENT ID.....	129
A-3-7	RECIRCULATION SYSTEM COMPONENT ID .....	131
A-3-8	INJECTION SYSTEM COMPONENT ID .....	133
A-3-9	EMERGENCY DEPRESSURIZATION AND SAFETY COLLECTION SYSTEM COMPONENT ID .....	135
A-3-10	AUTOClave HEAD DETAIL .....	137
A-3-11	AUTOClave HEAD AND SAMPLE ASSEMBLY DETAIL .....	138
A-3-12	TEST SAMPLE ASSEMBLY DETAIL .....	139
A-3-13	DETAILED CONTROL WIRING SCHEMATIC .....	140
A-4-1	NOTCH DEPTH VERSUS SURFACE CHORD LENGTH .....	143
A-4-2	SCHEMATIC OF FIXTURE USED WITH THE MTS TESTING SYSTEM TO INDUCE FATIGUE CRACKS IN THE TEST SAMPLE.....	144
A-4-3	SIDE PHOTO OF SAMPLE AND FIXTURE MOUNTED IN THE MTS TEST SYSTEM .....	144
A-4-4	FRONT VIEW OF SAMPLE AND FIXTURE INSTALLED IN THE MTS TEST SYSTEM .....	145

## List of Tables

3-1	MECHANICAL PROPERTIES OF HEAT 96834 .....	55
3-2	CHEMICAL COMPOSITION OF ALLOY 600 .....	55
5-1	TABULATED RESULTS FOR STRESS INTENSITY AND GROWTH RATES .....	79
5-2	TABULATED RESULTS FOR STRESS INTENSITY AND GROWTH RATES .....	87
A-1-1	CN9000A PID CONTROLLER PARAMETERS FOR STATIC AUTOCLAVE OPERATION .....	102
A-2-1	STATIC OPERATION STARTUP VALVE LINEUP .....	108
A-2-2	RECIRCULATION OPERATION STARTUP VALVE LINEUP .....	111
A-2-3	INJECTION SYSTEM VALVE LINEUP .....	117
A-3-1	ALLOY 600 TEST PLATFORM COMPONENTS SUMMARY .....	126
A-3-2	SAMPLE PRESSURIZATION SYSTEM COMPONENT ID .....	128
A-3-3	STATIC SYSTEM COMPONENT IDENTIFICATION .....	130
A-3-4	RECIRCULATION SYSTEM COMPONENT ID .....	132
A-3-5	INJECTION SYSTEM COMPONENT ID .....	134
A-3-6	DEPRESSURIZATION AND SAFETY COLLECTION SYSTEM COMPONENT ID .....	136
A-3-7	CONTROL SYSTEM WIRING DETAIL .....	141
A-5-1	TEST DATA WITH ERROR CALCULATIONS .....	147

## 1. Introduction

Since 1967, most pressurized water reactor steam generators have been constructed with tubes made of alloy 600. Alloy 600 is a strong, corrosion resistant nickel based alloy. However, environmentally assisted cracking (EAC) has occurred within tube sheets, just above tube sheets and in tight radius U-bends in this material<sup>1</sup>.

Today, steam generator tube degradation is the life-limiting phenomenon in pressurized water nuclear reactors with U-tube steam generators. Comprising over half the primary to secondary pressure boundary surface area, the steam generator tubes are of critical importance to reactor safety. Extensive investigations by numerous researchers have failed to produce a cohesive failure theory for the cracking phenomenon, known as Stress Corrosion Cracking<sup>2</sup>. Stress Corrosion Cracking has been observed on both the primary and secondary side of the steam generator tubes. Intergranular Stress Corrosion Cracking (IGSCC) on the secondary side periodically occurs at sites of Intergranular Attack (IGA), though either IGA or IGSCC can occur independently.

Because IGSCC is of such concern for reactor safety, frequent shutdowns for steam generator tube inspections must occur to ensure tube integrity. Each maintenance period not only costs millions of dollars in lost power generation, but many man-rem of maintenance personnel exposure. Development of an on-line steam generator tube monitoring system would decrease the periodicity of shutdowns for tube inspections

---

<sup>1</sup> J.T. Adrian Roberts, *Structural Materials in Nuclear Power Systems*, (New York: Plenum Press, 1981), p. 340.

<sup>2</sup> Herbert H. Uhlig and R. Winston Revie, *Corrosion and Corrosion Control*, 3rd Ed, (New York: John Wiley & Sons, 1985), p. 366.

and provide a more reliable warning of impending tube failure.

The scope of this thesis is to provide a proof of principle for detection of stress corrosion cracks in actual steam generator tube material under high temperature, pressure and corrosive environmental conditions utilizing previously developed alternating current potential drop (ACPD) crack detection techniques. If successful, the techniques used to detect the stress corrosion cracks can be expanded and refined into an on-line system in the future.

In order to demonstrate a proof of principle for crack detection by ACPD techniques in a high temperature, corrosive environment, an autoclave system with both static and recirculation capability was constructed. Under in-situ conditions, steam generator tubes require years for stress corrosion cracking to occur. To expedite the process, tube specimens were exposed to highly caustic conditions (10% sodium hydroxide and 0.1%  $\text{Na}_2\text{CO}_3$  added to subcooled deionized water) at  $315^\circ\text{C}$ . Boiling was prevented by maintaining pressure greater than saturation. Prevention of boiling is critical to preventing local concentration of caustic.

The specimens were internally pressurized to obtain a hoop stress up to 145% of yield stress. Based on previous studies of stress corrosion on alloy 600, this allowed crack initiation in weeks<sup>3</sup>. Further reductions in crack

---

<sup>3</sup> M. Payne and P. McIntyre, "Influence of Grain Boundary Microstructure on Susceptibility of Alloy 600 to Intergranular Attack and Stress Corrosion Cracking," *Corrosion-NACE*, XLIV, No. V, (May 1988), pp. 314-319.

initiation time were realized by polarizing the sample to +150 mv with respect to a nickel electrode<sup>4</sup>.

Crack detection was achieved using ACPD techniques previously developed<sup>5</sup>. Pick-up probes were attached on either side of an expected crack initiation site. An additional set of pickup probes were attached away from the test area to serve as a reference signal. The site of crack initiation was controlled by plating the tube specimen with nickel in every area but the crack initiation site. Probe spacing, frequency and current were determined empirically and through prior analytical results to yield optimum AC potential drop sensitivity.

Static system tests were performed to (i) test system integrity to the caustic solution, (ii) determine the ability of the selected temperatures, pressures and solution pH to initiate specimen cracking in a reasonable time frame, (iii) verify the ability of the system to initiate stress corrosion cracking in the specimen and (iv) verify the ability of the ACPD system to identify crack initiation and growth under these conditions. Subsequent testing obtained stress corrosion cracking data for the tube specimens for comparison to data available in the literature.

---

<sup>4</sup> J. B. Lumsden,, S.L. Jeanjaquet, J.P.N. Paine and A. McIlree, "Mechanism and Effectiveness of Inhibitors for SCC in a Caustic Environment", (*Seventh International Symposium on Environmental Degradation of Materials in Nuclear Power Systems - Water Reactors*, Vol 1, Breckenridge, CO: NACE International, August 7-10,1995), pp. 317-325.

<sup>5</sup> R.G. Ballinger and I.S. Hwang, "Characterization of Microstructure and IGSCC of Alloy 600 Steam Generator Tubing", (Final Report, EPRI TR-101983, Palo Alto: Electric Power Research Institute, (February 1993),p. 3-56.

## 2. Background

### 2.1 Nuclear Steam Generator Materials and Environment

The first nuclear steam generator tubes were constructed using austenetic stainless steel<sup>1</sup>. Corrosion related degradation occurred at a relatively rapid rate. The next generation of generators were built with alloy 600 tubing and an evolving water chemistry control program<sup>2</sup>. Though the general corrosion problems were mitigated to a great extent, stress corrosion and other localized corrosions continued to occur.

#### 2.1.1 Steam Generator Construction

The tubes of a typical steam generator used in nuclear applications are of either a recirculating, or U-tube, design (Westinghouse, Combustion Engineering) or a once-through design (Once Through Steam Generator or OTSG manufactured by Babcock and Wilcox)<sup>3</sup>. A typical steam generator has approximately 16000 straight-through tubes (Babcock and Wilcox design) or approximately 8000 to 9000 U-tubes in recirculating designs to provide adequate surface area for heat transfer from the primary to secondary fluid. The tubes can extend in length to 20.7 meters (68 feet) in a straight-through design. Approximately 15 support plates in both designs provide vertical and lateral support and vibration reduction over the tube length. The tubes are normally not welded onto the

---

<sup>1</sup> J.R. Cels, Caustic Stress Corrosion Cracking Studies at 288C(550F) Using the Straining Electrode Technique, *Corrosion-NACE*, V34, No.6 (June 1978), p. 198.

<sup>2</sup> James A. Adams and Eric S. Peterson, Steam Generator Secondary pH During A Steam Generator Tube Rupture, *Nuclear Technology*, Vol 102 (June 1993), p. 305.

<sup>3</sup> J.T.A. Roberts, *Structural Materials in Nuclear Power Systems*, (New York: Plenum Press, 1981), p. 323.

support plates and have clearances up to 0.25 mm (.010 in) between the support plate and tube to allow for thermal expansion. A 38 mm (1.5 in) thick tube sheet separates the primary from the secondary (one upper and one lower in a once-through design). The steam generator tubes are normally on the order of 12 mm to 18 mm in diameter and are heat fitted and tungsten inert gas welded into the tube sheet on the primary side. On the OTSGs manufactured by Babcock and Wilcox, the entire steam generator is stress-relieved in a furnace after final fabrication and welding of the hemispherical heads are completed<sup>4</sup>.

As can be seen in Figure 2-1, crevices between the secondary side of the tube sheet and tubes and on each side of the support plate tubes exist due to the construction described. In addition to the crevice, these areas have high residual or working stresses due to the press fit or constraining nature of the design. These crevices are typically the

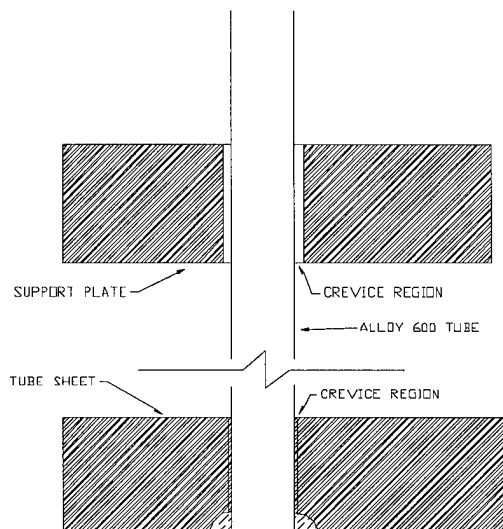


**Figure 2-1: Typical Areas of Steam Generator Tube Failure By Stress Corrosion Attack**

sites for intergranular attack (IGA) and stress corrosion cracking (IGSCC) and are the inherent flaw in steam generator design from a corrosion perspective. Additionally, residual stresses during U-tube bending can increase the localized stress levels many times higher than the hoop and radial stresses induced from the primary to secondary side

<sup>4</sup> Babcock & Wilcox, *Steam: its generation and use* (New York: Babcock & Wilcox, 1978), p. 23-11.



differential pressure. These residual stress areas will be described in more detail later.

### 2.1.2 Steam Generator Chemistry

The secondary side of nuclear steam generators operates in an alkaline environment with a pH typically in the 8.5 to 9.2 range for recirculating steam generators and 8.8 to 9.6 for Babcock and Wilcox once-through steam generators<sup>5</sup>. This pH range maintains a low general corrosion rate for all components in the steam generator since many components are either low alloy or carbon steel, including the steam generator shell.

There are four principal additives used to maintain secondary chemistry<sup>6</sup>. The principal pH control additive is ammonia ( $\text{NH}_4\text{OH}$ ), selected for its compatibility with all materials used in steam generator construction. Ammonia is very volatile and only minimal residuals remain on the heat transfer surfaces and in crevices during power operation. This allows contaminants (such as chlorine or sodium) to concentrate in tube crevices and create a corrosive environment. Other additives, such as morpholine, boric acid and hydrazine are added to provide buffering in the crevices. Morpholine, being less volatile than ammonia, has provided protection of carbon steel components (steam and condensate piping outside the steam generator especially) from erosion/corrosion in areas of two phase flow. Boric acid has been added to reduce the occurrence of "denting" caused by the growth of magnetite in the tube support plate crevices in generators with carbon steel support plates and has also mitigated intergranular attack of alloy 600

---

<sup>5</sup> James P. Adams and Eric S. Peterson, "Steam Generator Secondary pH During A Steam Generator Tube Rupture," *Nuclear Technology*, CII, (June 1993), pp. 304-306.

<sup>6</sup> Ibid, p. 305.

by high caustic<sup>7</sup>. Finally, hydrazine has been added as an oxygen scavenger<sup>8</sup>. Although alloy 600 is not susceptible to chloride stress corrosion cracking, it is still susceptible to oxygen-associated localized corrosion.

Chemistry in a steam generator crevice is not known. The case for a high caustic condition stems from much research and experimentation in this regime. R. Bandy, et.al., conducted tests on alloy 600 in high temperature caustic environments and concluded that the concentration of alkaline species was one of the more important factors governing intergranular corrosion<sup>9</sup>. It should be noted, however, that although the general environment of the tests was alkaline, no measurements of the chemistry in the crevice area were performed and Bandy concluded that "a more thorough knowledge of the crevice chemistry is required"<sup>10</sup>. S.M. Payne, et al., reported that impurities from the secondary water may concentrate in superheated hot leg crevices to 50% by weight of sodium hydroxide<sup>11</sup>. Another possible source for free caustic formation is from ionic impurities introduced from corrosion products in the feed, condensate and chemical addition system and leakage in the condenser. These impurities include sulfur, phosphates, and chlorides, among others<sup>12</sup>. These impurities

---

<sup>7</sup> "Boric Acid Application Guidelines for Intergranular Corrosion Inhibition," EPRI NP 5558, Electric Power Research Institute (1984).

<sup>8</sup> James P. Adams and Eric S. Peterson, "Steam Generator Secondary pH During A Steam Generator Tube Rupture," *Nuclear Technology*, CII, (June 1993), p. 305.

<sup>9</sup> R. Bandy, R. Roberge, and D. van Rooyen, "Intergranular Failures of alloy 600 in High Temperature Caustic Environments," *Corrosion - NACE*, XVI no. III, (March 1985), pp. 142, 149-150.

<sup>10</sup> R. Bandy, R. Roberge, and D. van Rooyen, pp. 142-151.

<sup>11</sup> S. M. Payne and P. McIntyre, "Influence of Grain Boundary Microstructure on the Susceptibility of alloy 600 to Intergranular Attack and Stress Corrosion Cracking," *Corrosion-NACE*, XLIV no. V, (May 1988), pp. 314-319.

<sup>12</sup> J.T.A. Roberts, *Structural Materials in Nuclear Power Systems*, (New York: Plenum Press, 1981), pp. 336-337.

can concentrate in the low flow regions, such as the tube sheet crevice, or in sludge at the top of the tube sheet, and cause locally high alkaline conditions in high heat flux, low flow regions (typically where intergranular corrosion occurs).

### 2.1.3 Material Properties of Alloy 600 Steam Generator Tubes

Alloy 600 is a nickel-chromium-iron alloy containing at least 72% nickel (plus cobalt), 14 to 17% chromium, 6-10% iron, 0.15% carbon (maximum, nominal carbon content is in the 0.08% range<sup>13</sup>) and small percentages of manganese, sulfur, silicon and copper. These concentrations are nominal and actual concentrations vary within this range. The importance of this variation and the small percentages of other materials added in the course of alloy 600 manufacture will play a role in the ability of a particular heat to resist intergranular attack and stress corrosion cracking. Typically in older vintage steam generators, following milling, the tubes are heated to a temperature to allow rearrangement of the individual atoms into a more stable structure. The tubes are then allowed to cool in the furnace. This process is known as mill annealing and softens the tubes to impart added ductility<sup>14</sup>. Steam generator tubes conform to American Society for the Testing of Materials (ASTM) standard B-163 and American Society of Mechanical Engineers (ASME) Boiler and Pressure Vessel Code Section III (Nuclear Vessels) with a minimum tensile strength of 552 MPa (80000 psi) and minimum 0.2% yield strength of 241 MPa (35000 psi) in a mill-annealed condition. Alloy 600 is ductile at room temperature with Charpy V-Notch impact strengths of

---

<sup>13</sup> Wayne Z. Friend, *Corrosion of Nickel and Nickel Based Alloys* (New York: John Wiley & Sons, 1980), p. 143.

<sup>14</sup> L. H. Van Vlack, *Elements of Material Science and Engineering*, 3rd Ed., (Reading, MA: Addison-Wesley Publishing Co., 1975), pp. 374-375.

approximately 250 Joules at typical steam generator secondary side operating temperatures of 224°C to 273°C (inlet and outlet, respectively)<sup>15</sup> for mill-annealed material. It does not embrittle after long exposure at high temperatures. Fatigue strength is affected by grain size and condition and by temperature, with typical values of fatigue strength greater than 325 MPa for 10<sup>8</sup> cycles<sup>16</sup>.

Nickel provides alloy 600 with a resistance to corrosion by a variety of organic and inorganic compounds. It is especially resistant to caustics and caustic solutions, the corrosion resistance being proportional to the nickel content in sodium hydroxide.

Chromium is added to provide resistance to corrosion in high temperature oxidizing environments, and resistance to sulfur compounds (sulfur compounds act as catalyst poisons that ease access of hydrogen into a metal lattice resulting in cracking due to hydrogen embrittlement<sup>17</sup>). The effect of chromium additions to nickel is illustrated in Figure 2-2. The active region of Figure 2-2 is defined as the potential range at which significant corrosion occurs. The point at which the current suddenly drops to a value orders of magnitude lower is called the critical current density and the lower current density is the passive current density. The vertical region of Figure 2-2 where this lower current density exists is known as the passive region and the potential in this range is the

---

<sup>15</sup> Neil E. Todreas and Mujid S. Kazimi, *Nuclear Systems I* (Bristol, PA: Taylor & Francis, 1990), p. 5.

<sup>16</sup> *Inconel*, Inco Alloys International (Huntington, WV: Inco Alloys International, Inc).

<sup>17</sup> Herbert H. Uhlig and R. Winston Revie, *Corrosion and Corrosion Control* (New York: John Wiley & Sons, 1985), p. 142.

passive potential<sup>18</sup>. Passivity for a metal is simply the state where the rate of dissolution in a given environment under steady state conditions becomes less as the electrode potential is increased than the rate at some lower potential<sup>19</sup>. At chromium concentrations greater than 9%, chromium in nickel significantly reduces the current density in the active corrosion region. For chromium concentrations greater than 10%, the critical current density is reduced, the passive potential widens and the passive current density is reduced<sup>20</sup>.

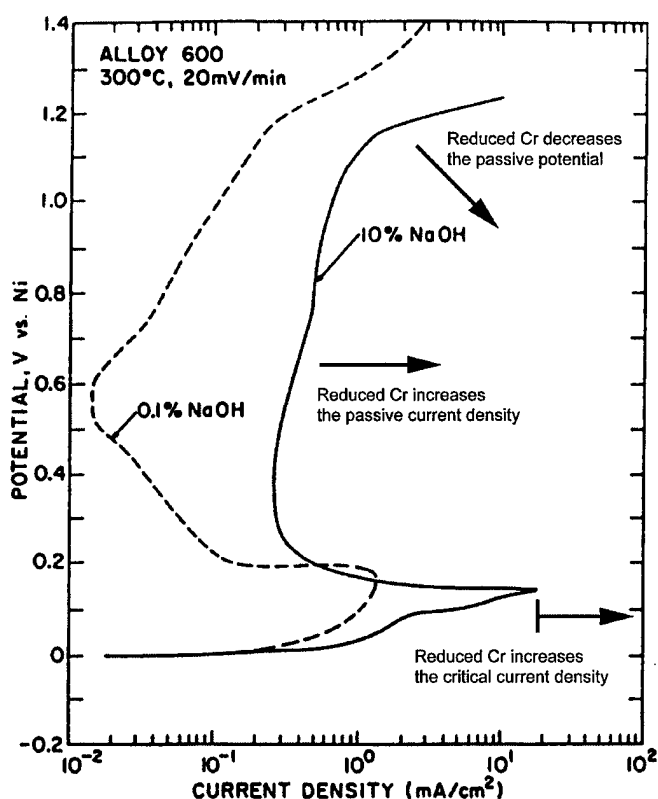


Figure 2-2: Evans Diagram for Alloy 600 Showing the Effect of Chromium Concentration on Corrosion Current Density and Passivity.

<sup>18</sup> Herbert H. Uhlig and R. Winston Revie, *Corrosion and Corrosion Control*, 3rd Ed (New York: John Wiley & Sons, 1985), pp. 61-65.

<sup>19</sup> C. Wagner, Discussions at the First International Symposium on Passivity, Heiligenberg, West Germany, 1957, *Corrosion Science*, Vol 5, (1965), p.751.

<sup>20</sup> Wayne Z. Friend, *Corrosion of Nickel and Nickel Based Alloys* (New York: John Wiley & Sons, 1980), p. 136.

Chromium seems also to be the key factor in providing chloride stress corrosion resistance in alloy 600. This was demonstrated by Piron<sup>21</sup>, who added concentrations of NaCl to a H<sub>2</sub>SO<sub>4</sub> solution containing alloy 600 and nickel 200 which were made to passivate by controlling the potential until a breakdown of passivity occurred as indicated by a large change in the passive current density. The critical NaCl concentrations were found to be an order of magnitude higher for alloy 600 than nickel 200 (2% vs. 0.1%, respectively). Although the nominal concentration of 14% to 17% is specified, heat treatment of the material and differences during manufacture can cause localized regions at the grain boundary which contain concentrations significantly below the nominal, thereby altering the corrosion resistance of alloy 600<sup>22</sup>. The importance of this phenomenon in intergranular corrosion is further explained below.

Iron is present in the stated percentage from the addition of ferrochromium, instead of metallic chromium, during melting. Ferrochromium is used mainly to reduce cost<sup>23</sup>.

Several precipitated phases can be present in the microstructure. These include titanium nitrides, titanium carbides, cyanonitrides, and chromium carbides, with the latter being the most prevalent because of the natural chromium content of alloy 600<sup>24</sup>. The particular concentration of

---

<sup>21</sup> Wayne Z. Friend, *Corrosion of Nickel and Nickel Based Alloys* (New York: John Wiley & Sons, 1980), p. 139.

<sup>22</sup> Wayne Z. Friend, *Corrosion of Nickel and Nickel Based Alloys* (New York: John Wiley & Sons, 1980), p. 143.

<sup>23</sup> Wayne Z. Friend, *Corrosion of Nickel and Nickel Based Alloys* (New York: John Wiley & Sons, 1980), p. 142.

<sup>24</sup> Inco Alloys International, *Inconel*, (Huntington, WV: Inco Alloys International) p. 12.

carbides at the grain boundaries can affect the susceptibility of a particular heat to intergranular corrosion<sup>25</sup>.

## 2.2 Stress Corrosion Cracking Theories

The two prevalent theories which explain IGSCC involve either anodic dissolution along the grain boundary or microvoid formation allowing crack propagation<sup>26,27</sup>. IGSCC, as the name implies, occurs along grain boundaries. Although transgranular cracking is possible, cases have been extremely rare and usually can be attributed to other factors influencing the crack propagation path. In post-mortems of tube failures from IGSCC, three common factors emerged. First, high stresses in the area of failure existed. Second, the material was susceptible to SCC. Finally, high temperatures influenced the damage rate<sup>28</sup>. In each theory, these factors influence a physical phenomenon which allows crack initiation, propagation and eventual failure.

### 2.2.1 Film Rupture Theory for Crack Initiation

Crack initiation is hypothesized to be the result of a film rupture mechanism which allows attack of the material at

---

<sup>25</sup> S. M. Payne and P. McIntyre, "Influence of Grain Boundary Microstructure on the Susceptibility of alloy 600 to Intergranular Attack and Stress Corrosion Cracking," *Corrosion-NACE*, XLIV no. V, (May 1988), pp. 314-319.

<sup>26</sup> R. Bandy, R. Roberge, and D. van Rooyen, "Intergranular Failures of Alloy 600 in High Temperature Caustic Environments," *Corrosion - NACE*, XVI no. III, (March 1985), pp. 142-150.

<sup>27</sup> Y. Shen and P.G. Shewmon, "IGSCC Crack Growth of Alloy 600 and X-750 in Steam," *Corrosion*, Vol. 47, No. 9 (September, 1991), pp. 712-718.

<sup>28</sup> P.L. Andersen, "Effects of Temperature on Crack Growth Rate in Sensitized Type 304 Stainless Steel and Alloy 600," *Corrosion Science*, Vol.49, No.9 (September 1993), pp. 714-725.

the grain boundary<sup>29</sup>. Alloy 600 in a caustic environment passivates, primarily due to the high nickel content<sup>30,31</sup>. Passivation theory holds that a film, most likely of an oxide ( $\text{Cr}_2\text{O}_3$  is generally accepted in this case<sup>32</sup> although spinel oxides of  $\text{Fe}_3\text{O}_4$ ,  $\text{Cr}_3\text{O}_4$ , and  $\text{Ni}_3\text{O}_4$  have also been reported<sup>33</sup>) or hydroxide composition, forms a thin protective layer on the surface of the material. The film lowers the current density significantly and therefore the corrosion rate is reduced significantly<sup>34</sup>. The 14% to 17% chromium content, besides providing resistance to chloride stress corrosion, further lowers the corrosion rate. Experiments have shown that chromium concentrations in nickel greater than 9% significantly reduce the current density in the active corrosion region and for concentrations greater than 10%, the passive potential widens and the passive current density is reduced<sup>35</sup>.

Film rupture can be explained by two mechanisms. The first requires that a strain be applied. The second suggests a

---

<sup>29</sup> R. Bandy, R. Roberge, and D. van Rooyen, "Intergranular Failures of Alloy 600 in High Temperature Caustic Environments," *Corrosion - NACE*, XVI no. III, (March 1985), p. 149.

<sup>30</sup> Wayne Z. Friend, *Corrosion of Nickel and Nickel Based Alloys* (New York: John Wiley & Sons, 1980), p. 157.

<sup>31</sup> International Nickel Co., Inc., "Corrosion Resistance of Nickel and Nickel-Containing Alloys in Caustic Soda and other Alkalies," *Corrosion Engineering Bulletin*, CEB-2, 1971.

<sup>32</sup> Wayne Z. Friend, *Corrosion of Nickel and Nickel Based Alloys* (New York: John Wiley & Sons, 1980), p. 165.

<sup>33</sup> Warren E. Berry, *Corrosion in Nuclear Applications* (New York: John Wiley & Sons, 1971), pp. 185-189.

<sup>34</sup> J. K. Sung, J. Koch, T. Angelu, and G.S. Was, "The Effect of Grain Boundary Chemistry on Intergranular Stress Corrosion Cracking of Ni-Cr-Fe Alloys in 50 Pct NaOH at 140°C" *Metallurgical Transactions A*, Vol. 23A, No. 10, (October 1992), pp. 2887-2904.

<sup>35</sup> Wayne Z. Friend, *Corrosion of Nickel and Nickel Based Alloys* (New York: John Wiley & Sons, 1980), p. 136.



breakdown of the film due to a change in the underlying material composition, thus altering the electrochemical potential<sup>36</sup>.

Film rupture by a strain mechanism requires that a stress be applied to the material. The applied tensile stress levels can be as low as 10% of the yield stress<sup>37</sup>. However, larger stress levels are present in the failure areas when one examines residual stresses induced from manufacture processes.

There are two basic steam generator tube designs used in pressurized water reactors today: U-bend (Westinghouse, Combustion Engineering) and straight-through (Babcock and Wilcox). The U-bend tube experiences the highest SCC rates primarily due to the stress relieving process which occurs in Babcock and Wilcox steam generators<sup>38</sup>. Stresses present in U-bends are from applied and residual stresses (other stresses may be induced from corrosion or mechanical binding also). Typical operating stresses are on the order of 11 MPa in the hoop or circumferential direction and 5 MPa in the axial direction<sup>39</sup>. Both of these applied stresses are well below 172

---

<sup>36</sup> J.K. Sung, J. Koch, T. Angeliu and G.S. Was, "The Effect of Grain Boundary Chemistry on Intergranular Stress Corrosion Cracking of Ni-Cr-Fe Alloys in 50 Pct NaOH at 140°C," *Metallurgical Transactions A*, Vol.23A, No.10, (October, 1992), pp. 2895-2904.

<sup>37</sup> Scaffer, Saxena, Antolovich, Sanders and Warner, *The Science and Design of Engineering Materials*, (Chicago: Irwin, 1995), p. 657.

<sup>38</sup> Babcock and Wilcox, *Steam/its generation and use*, 39th Ed. (New York: Babcock and Wilcox, 1978), p. 31-22.

<sup>39</sup> V.N. Shah, D.B. Lowenstein, A.P.L. Turner, S.R. Ward, J.A. Gorman, P.E. MacDonald, G.H. Weidenhamer, "Assessment of primary water stress corrosion cracking of PWR steam generator tubes," *Nuclear Engineering and Design*, Vol. 134, No. 2-3, pp. 199-216.

to 345 MPa yield stress of alloy 600 following mill annealing<sup>40</sup>.

Residual stresses, however, especially in areas of severe geometry changes (Figure 2-3), can be at or greater than the yield stress. Residual stresses from the bending process tend to occur directly adjacent to the high curvature area. Tubes in rows 1 or 2 have the tightest bend radius, on the order of

55.4 mm. Residual hoop stresses in the extrados or flank can be as high as 100 MPa or higher if significant cold working was performed<sup>41</sup>. Of the approximately 9000 U tubes in a typical steam generator, tubes in rows 1 or 2 suffer the highest SCC failure rate, as expected.

Santarini<sup>42</sup>, Rios<sup>43</sup>, and Shah<sup>44</sup> all found that crack growth rate increased as the strain rate increased following an

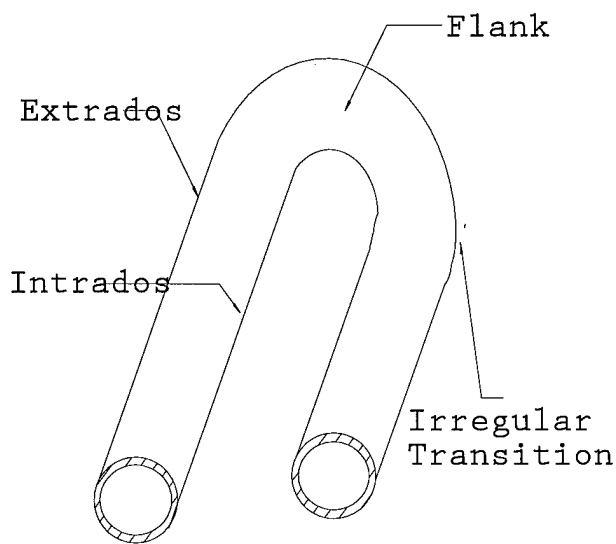


**Figure 2-3: Schematic of a steam generator tube showing areas of high residual stress**

<sup>40</sup> Inconel, Inco Alloys International (Huntington, WV:Inco Alloys International, Inc.).

<sup>41</sup> V.N. Shah, D.B. Lowenstein, A.P.L. Turner, S.R. Ward, J.A. Gorman, P.E. MacDonald, G.H. Weidenhamer, "Assessment of primary water stress corrosion cracking of PWR steam generator tubes," *Nuclear Engineering and Design*, Vol. 134, No. 2-3, pp. 199-216.

<sup>42</sup> R.B. Rebak and Z. Szlarska-Smialwska, "Influence of Stress Intensity and Loading Mode on Intergranular Stress Corrosion Cracking of Alloy 600 in Primary Water of Pressurized Water Reactors," *Corrosion*, Vol. 50, No. 5, (May 1994), pp. 378-393.

<sup>43</sup> R. Rios, T. Magnin, D. Noel, O. DeBouvier, "Critical Analysis of Alloy 600 Stress Corrosion Cracking Mechanisms in Primary Water," *Metallurgical and Materials Transactions A*, Vol. 26, No. 4, (1995), pp. 925-939.

<sup>44</sup> V.N. Shah, op. cit., pp. 199-216.

exponential relationship. This correlation supports a film rupture mechanism and is consistent with the observed stresses at failure sites in U tubes<sup>45</sup>.

The second explanation for film breakdown is electrochemical. In 1984, Woodward<sup>46</sup> identified a potential range of -750mV to -340mV(SCE) in which SCC initiated. Sung<sup>47</sup>, et al, theorize that chromium depletion (due to diffusion forming chromium carbide precipitates) or an excess of carbon migrating toward the grain boundary alters the electrochemical potential. This favors the formation of a less protective nickel-rich hydroxide film vice a protective nickel oxide. The nickel hydroxide film is stable only over a small range of pH. If localized pH were acidic or highly caustic, the nickel hydroxide film would become soluble (unstable), leaving the underlying material unprotected.

### 2.2.2 Crack Propagation by Anodic Dissolution

Once a film rupture occurs, crack propagation in the matrix material can proceed. Bandy<sup>48</sup>, et al, suggested that film rupture is followed by anodic dissolution along the grain boundary and subsequent repassivation when the material is at

---

<sup>45</sup> V.N. Shah, D.B. Lowenstein, A.P.L. Turner, S.R. Ward, J.A. Gorman, P.E. MacDonald, G.H. Weidenhamer, "Assessment of primary water stress corrosion cracking of PWR steam generator tubes," *Nuclear Engineering and Design*, Vol. 134, No. 2-3, pp. 201-205.

<sup>46</sup> J. Woodward, "Rapid Identification of Conditions Causing Intergranular Corrosion or Intergranular Stress Corrosion Cracking in Sensitized Alloy 600," *Corrosion - NACE*, XL, No. XII, (December 1984), pp. 640-643.

<sup>47</sup> J. K. Sung, J. Koch, T. Angeliiu, and G.S. Was, "The Effect of Grain Boundary Chemistry on Intergranular Stress Corrosion Cracking of Ni-Cr-Fe Alloys in 50 Pct NaOH at 140°C," *Metallurgical Transactions A*, Vol. 23A, No. 10, (October 1992), pp. 2887-2904.

<sup>48</sup> R. Bandy, R. Roberge, and D. van Rooyen, "Intergranular Failures of Alloy 600 in High Temperature Caustic Environments," *Corrosion - NACE*, XVI No. III, (March 1985), pp. 142-151.

the passive potential. Subsequent cycles propagate the crack along the grain boundary. Bandy supported his conclusions by demonstrating that the rate of SCC is significantly influenced by the electrochemical potential. With samples in a potential range of +150 to 200 mV versus nickel (around the passive potential for alloy 600 at 300°C), grain boundary grooving occurred. However, for samples held at 0 mV versus nickel, no IGSCC occurred<sup>49</sup>.

Chromium carbides are the most likely candidate for the cathode. The cathodic behavior of the carbides in caustic was demonstrated by Rebak, et al<sup>50</sup>. There are two major forms of carbide which precipitate at the boundary:  $M_7C_3$  and  $M_{23}C_6$ . The major constituent of the M is chromium. The depletion of chromium at the grain boundary due to diffusion and subsequent precipitation as a carbide does not seem to influence the susceptibility of the material to SCC<sup>51</sup>. This leaves the carbon or other precipitates in the carbide as the major culprit. However, several researchers have linked carbon content not only with crack initiation phenomenon, but crack growth rates. Johns and Beckitt found the susceptibility to IGSCC to be "critically dependent on the grain size and carbon content of the material." <sup>52</sup>

---

<sup>49</sup> R. Bandy, R. Roberge, and D. van Rooyen, p. 149.

<sup>50</sup> I. Jang, "Effect of Sulphate and Chloride Ions on the Crevice Chemistry and Stress Corrosion Cracking of Alloy 600 in High Temperature Aqueous Solutions," *Corrosion Science*, Vol. 33, No. 1 (1992), pp. 25-38.

<sup>51</sup> R. Rios, T. Magnin, D. Noel and O. deBouvier, "Critical Analysis of Alloy 600 Stress Corrosion Cracking Mechanisms in Primary Water," *Metallurgical and Materials Transactions A*, Vol.26, No.4, (1995), pp. 928-929.

<sup>52</sup> D.R. Johns and F.R. Beckitt, "Factors Influencing the Thermal Stabilisation of Alloy 600 Tubing Against Intergranular Corrosion," *Corrosion Science*, XXX No. II/III, (1990), pp. 223-237.

The carbides that do form are precipitated out at the grain boundaries. Anodic dissolution would occur in the area of the grain immediately adjacent to the carbide. Once dissolution takes place, the material along the grain boundary and in the grain boundary is removed and a pit or crack is formed. With the cause of the initial film breakdown removed, repassivation can then take place. Like other mechanically induced cracks, stresses tend to concentrate at the crack tip. Strain-induced crack propagation can then occur until a carbide particle is reached which can tend to pin the dislocations at the grain boundary and prevent further crack propagation. Again, electrochemical changes occur to break down the film, dissolution occurs and the process is repeated until failure.

### 2.2.3 Crack Propagation by Microvoid Formation

A second major theory for SCC crack propagation in alloy 600 includes the formation of microvoids along the grain boundary. Generally, the theory holds that small voids from the formation of micro gas pockets, either hydrogen, or more likely methane, are formed in front of the advancing crack<sup>53</sup>. The reaction of hydrogen, formed by electrochemical processes at the crack tip:



and carbon near the grain boundary, forms methane by:



---

<sup>53</sup> Y. Shen and P. G. Shewmon, " Intergranular Stress Corrosion Cracking of Alloy 600 and X-750 in High Temperature Deaerated Water/Steam," *Metallurgical Transactions A*, Vol. 22A, No. 8, (August 1991), pp. 1857-1864.

Lim and Raj<sup>54</sup> demonstrated that the nucleation of such microvoids "can be...aided by the impingement of slip lines along the grain boundary", with a void spacing of 0.2 $\mu$ m. It has also been observed that if carbides are present, the activity of the carbon at the grain boundary is reduced, the methane pressure is reduced and IGSCC is slower. If temperature increases, the stress, and by relation, the strain, increase. Stress-assisted diffusion, especially with stress concentration at the crack tip, may become an important factor in promoting diffusion toward the crack tip. Once hydrogen and carbon interact at the front of the propagating tip, small voids form which are eventually connected by the strain in the material, propagating the crack<sup>55</sup>. As the crack propagates deeper into the material, voids continue to form and join ahead of the advancing crack, eventually leading to material failure.

Although there are several other theories to explain stress corrosion cracking, the two theories presented here are the only ones to incorporate observed microstructural, electrochemical and mechanical phenomena. Determining which is the actual mechanism is difficult. Each incorporates ideas which appeal to certain observed aspects better than the others. For example, dissolution theory does not seem to explain why primary water stress corrosion cracking is more prevalent than secondary side stress corrosion cracking, though microvoid formation seems to readily incorporate an explanation. In reality, there may be more than one mechanism

---

<sup>54</sup> Y. Shen and P. G. Shewmon, " Intergranular Stress Corrosion Cracking of Alloy 600 and X-750 in High Temperature Deaerated Water/Steam," *Metallurgical Transactions A*, Vol. 22A, No. 8, (August 1991), pp. 1857-1864.

<sup>55</sup> Y. Shen and P. G. Shewmon, pp. 1857-1864.

which actually occurs to cause crack initiation and propagation.

#### 2.2.4 Impurities in Secondary Steam Generator Water

The dissolution of the passive layer, and its importance to IGSCC described above, may be accelerated by the introduction of chlorides or other ionic impurities<sup>56</sup>. Chlorides are specifically addressed due to their ability to either prevent the formation of or to break down previously formed passive layers. In theory, chloride ions either increase the permeability of the formed oxide layer, or allow metal ions to pass more easily to the electrolyte if a chemisorbed layer is present<sup>57</sup>. The effect is the same in both cases, allowing corrosion rates to increase by reducing the potential below the passive potential.

Seawater is often used to cool the condensate discharge from the turbines, which is fed back to a steam generator in a typical Rankine cycle. Any tube leaks in the condenser will allow chloride ions into the steam generator (seawater is approximately 19,500 ppm chlorides). Although a typical nuclear plant condensate system is monitored for chloride introduction, it is possible for levels below detectable to slowly concentrate chlorides in the steam generator. Typically, chlorides are controlled in the ppm range to avoid this concentration. However, this is a bulk fluid level and concentration of chloride ions in a crevice due to a low flow

---

<sup>56</sup> Wayne Z. Friend, *Corrosion of Nickel and Nickel Based Alloys* (New York: John Wiley & Sons, 1980), pp. 136-142,

<sup>57</sup> Herbert H. Uhlig and R. Winston Revie, *Corrosion and Corrosion Control* (New York: John Wiley & Sons, 1985), p. 74.

situation can result in levels in the hundreds or thousands of parts per million.

Sulfur appears to be a concern only in acidic, oxidizing environments<sup>58</sup>. Today's steam generator chemistry, combined with deoxygenating water systems, prevent this type of environment from occurring. Despite this, IGSCC still occurs, casting doubt on the importance of sulfur in promoting IGSCC.

Free hydrogen is present in relatively large quantities on the primary side of the steam generator tubes, though in very minute quantities on the secondary side. The surplus of hydrogen results in a highly reducing environment on the primary side. Hydrogen inventories are maintained by (1) injection of  $H_2$  into the primary, (2) water decomposition under a neutron radiation flux and (3) decomposition of some primary pH additives. Hydrogen is effective in removing oxygen by radiolytic recombination in the presence of a gamma flux. Rios, et al,<sup>59</sup> found, however, that hydrogen can only enter the material if a crack has been previously initiated. This suggests that film rupture must occur before hydrogen affects the material. This would imply, along with the previous discussion of microvoid formation, that hydrogen concentration indeed plays an extremely important role in SCC. If the microvoid formation theory is correct, the material in a higher concentration of hydrogen would have increased diffusion into

---

<sup>58</sup> I. Jang, "Effect of Sulphate and Chloride Ions on the Crevice Chemistry and Stress Corrosion Cracking of Alloy 600 in High Temperature Aqueous Solutions," *Corrosion Science*, Vol. 33, No. 1 (1992), pp. 25-38.

<sup>59</sup> R. Rios, T. Magnin, D. Noel, O. DeBouvier, "Critical Analysis of Alloy 600 Stress Corrosion Cracking Mechanisms in Primary Water," *Metallurgical and Materials Transactions A*, Vol. 26, No. 4, (1995), pp. 925-939.



the material (since the gradient would be definitely into the material). This could promote faster void formation and subsequent crack propagation. It is interesting to note that PWSCC occurs the most frequently of all SCC<sup>60</sup>. This would then support the relatively larger SCC failures on the primary side versus the secondary side.

### 2.3 Role of Inhibitors

It is speculated that the addition of various compounds to the secondary steam generator environment may mitigate or terminate intergranular stress corrosion cracking. Recently, several researchers have investigated the use of Titanium compounds (TiO<sub>2</sub>, Tyzor, TiLAC, and Ti(Bu)<sub>4</sub>), cerium salts, and zinc compounds<sup>61</sup>. Though results indicate that indeed crack mitigation or the prevention of the onset of SCC is possible, the exact mechanism of interaction is still unknown.

The majority of the laboratory testing has been performed in caustic environments which simulate the pH of an operating steam generator (pH=10) at a temperature of approximately 315°C. Typical sample geometries include C-rings or standard ASTM tensile specimens machined from alloy 600 stock provided by the manufacturers of nuclear steam generator tubing. Recent testing, as well as earlier results<sup>62</sup>, demonstrated promise using titanium compounds over other possible additives. The

---

<sup>60</sup> V.N. Shah, D.B. Lowenstein, A.P.L. Turner, S.R. Ward, J.A. Gorman, P.E. MacDonald, G.H. Weidenhamer, "Assessment of Primary Water Stress Corrosion Cracking of PWR Steam Generator Tubes," *Nuclear Engineering and Design*, Vol. 134, No.2-3, pp. 199-216.

<sup>61</sup> J. B. Lumsden, S.L. Jeanjaquet, J.P.N. Paine and A. McIlree, "Mechanism and Effectiveness of Inhibitors for SCC in a Caustic Environment", *Seventh International Symposium on Environmental Degradation of Materials in Nuclear Power Systems - Water Reactors*, Vol. 1 (Breckenridge, CO: NACE International, August 7-10, 1995), pp. 317-323.

<sup>62</sup> J.B. Lumsden and P.J. Stocker, "Inhibition of IGA in Nickel Based Alloys in Caustic Solutions", *Corrosion/88*, Paper No. (Houston, TX: National Association of Corrosion Engineers, 1988).

solubility of the particular additive appears important<sup>63</sup> however. Measurement of the potential and/or applied potential is also performed to characterize the electrochemical environment.

Results indicate that the inhibitors may react by one of two methods detected thus far. In several cases, the inhibitors act to raise the potential above which SCC will occur. The IGSCC potential region appears to be +150 to +200mV versus nickel and occurs at the greatest rate at the passive potential<sup>64</sup>. Addition of titanium compounds increases the threshold potential by a minimum of 50 milli-volts and in a few cases prevented SCC occurrence within the test period<sup>65</sup>. In other cases, the inhibitor is thought to stabilize the passive film<sup>66</sup> preventing the onset of SCC by temporarily or permanently delaying the onset of film breakdown. Both hypotheses correlate well with the film rupture/anodic dissolution theory for SCC.

---

<sup>63</sup> M.T. Miglin, J.V. Monter, C.S. Wade, M.J. Psaila-Dombrowski, and A.R. McIlree, "SCC of Alloy 600 in Complex Caustic Environments", *Seventh International Symposium on Environmental Degradation of Materials in Nuclear Power Systems - Water Reactors*, Vol. 1 (Breckenridge, CO: NACE International, August 7-10, 1995), pp. 277-290.

<sup>64</sup> R. Bandy, R. Roberge, and D. van Rooyen, "Intergranular Failures of Alloy 600 in High Temperature Caustic Environments," *Corrosion - NACE*, XVI No. III, (March 1985), p. 149.

<sup>65</sup> J. B. Lumsden, S.L. Jeanjaquet, J.P.N. Paine and A. McIlree, "Mechanism and Effectiveness of Inhibitors for SCC in a Caustic Environment", *Seventh International Symposium on Environmental Degradation of Materials in Nuclear Power Systems - Water Reactors*, Vol. 1 (Breckenridge, CO: NACE International, August 7-10, 1995), pp. 321-322.

<sup>66</sup> M.T. Miglin, J.V. Monter, C.S. Wade, M.J. Psaila-Dombrowski, and A.R. McIlree, "SCC of Alloy 600 in Complex Caustic Environments", *Seventh International Symposium on Environmental Degradation of Materials in Nuclear Power Systems - Water Reactors*, Vol. 1 (Breckenridge, CO: NACE International, August 7-10, 1995), p. 281.

## 2.4 Crack Measurement by Potential Drop Methods

In recent years two primary methods of detecting "small" cracks have emerged. The first involves the use of a constant frequency, or DC current, the second an alternating frequency, or AC current. In each case, the initiation of cracks in the material results in a measurable potential drop when probes are placed across the crack initiation site.

### 2.4.1 Theory of DC Potential Drop

Direct current potential drop was initially used for crack detection due to the relatively straightforward application of direct current theory to metallic conductors. In direct current flow, the current travels along the conductor from injection point to pickup. The resistance of the conductor is dependent on the material's resistivity,  $\rho$ , which is a function of temperature, the conductor length,  $\ell$ , and area,  $A$ . Applying Ohm's Law and the relationship for resistance:

$$E = \frac{I\rho\ell}{A} \quad (2-3)$$

Assuming for a moment that the resistivity is constant with temperature, the reduction of cross-sectional area due to crack penetration results in an increase in the potential (assuming the conductor is not expanding in the direction of  $\ell$ ). As can be seen, this simple relationship allows the detection of crack initiation and growth based on a simple reduction of area.

On closer examination, several difficulties arise which make the application of DC potential drop systems inferior to the use of AC potential drop detection schemes. The resistance losses in the conductor during current transmission cause heating according to:

$$Losses = I^2 R = V I . \quad (2-4)$$

As temperature increases for nickel alloys, the resistivity increases resulting in an increase in potential. Additionally, the junction of the input probes with the conductor surface can result in electromagnetic fields. These fields, caused by thermal differences between the two materials (i.e. "thermocouple effect"), can be significant<sup>67,68</sup>.

The two effects, the resistivity change due to temperature and the thermocouple effect, can be compensated for by employing two techniques. The first is to measure the potential across a similar conductor (i.e. same geometry, input probe and pickup probe spacing, etc.) which is placed at the same temperature as the conductor under test. The thermal effects of the potential change due to resistivity changes can be mathematically eliminated by normalizing the sample with respect to the reference. The second method, developed by General Electric<sup>69</sup> and employed in many DC potential crack measurement systems, reverses the applied current at a specified interval (e.g. every 0.5 seconds). This changes the polarity of the induced junction electromagnetic field. The measured potential drop initially is additive with the electromagnetic field during the initial half cycle and subsequently subtractive on the next half cycle. The thermocouple effect is essentially eliminated by averaging the measured potential during each cycle.

---

<sup>67</sup> T. Baumeister, E. Avallone, T. Baumeister III, *Mark's Standard Handbook for Mechanical Engineers*, 8th Ed. (New York: McGraw-Hill Book Co., 1978), pp. 16-11-16-13.

<sup>68</sup> W. R. Catlin, D.C. Lord, T.A. Prater and L.F. Coffin, *The Reversing DC Electrical Potential Method* (Schenectady, NY: General Electric).

<sup>69</sup> W. R. Catlin, D.C. Lord, T.A. Prater and L.F. Coffin, *The Reversing DC Electrical Potential Method* (Schenectady, NY: General Electric).

In addition to the thermal effects on potential measurement, the relatively low resistivity of alloy 600 in the temperature range of interest requires a relatively large current be applied to allow for a sufficient potential drop to occur between the pickup probes. From equation (2-3), the gain for a DC potential drop system is inversely proportional to the change in area resulting from crack growth:

$$\frac{V_2}{V_1} = \frac{A_1}{A_2} \quad (2-5)$$

Given the low resistivity of alloy 600 (inverse of conductivity from Table 1), equation 2-5 requires the application of currents normally in excess of 1 ampere for a sufficient gain in voltage from small changes due to crack propagation into the wall.

Switching requirements, reference samples, and large applied currents are drawbacks to the application of using DC potential for an on-line monitor system. As will be seen, these drawbacks can be mitigated or eliminated and an increase in sensitivity to crack initiation realized with an AC potential drop system.

#### 2.4.2 Theory of AC Potential Drop

Use of alternating current in a potential drop system allows a higher sensitivity to crack detection by taking advantage of the skin effect present in conductors. The skin effect distributes the current density to the outside of the conductor with little or no current flow on the interior. The depth of actual current flow is frequency and material dependent and must be calculated to optimize the sensitivity response of the system. A brief review of the applicable electromagnetic propagation theory is presented for background.

R.W.P. King developed the following derivation for current density distribution as a function of the radius in a tubular conductor<sup>70</sup>. Assuming a conductor of good conductivity surrounded on the inside and outside by "space" (i.e. vacuum), the potential functions from the Maxwell- Lorentz Equations for an electromagnetic field,

$$\nabla^2 \vec{A} + \beta^2 \vec{A} = 0 \quad (2-6)$$

are applied.  $\vec{A}$  is referred to as the vector potential and  $\vec{\beta}$  is the phase constant. Expressing equation (2-5) in cylindrical coordinates, the solution is made separable. The radial solution is the only solution of interest since the length of the overall conductor (i.e., wires plus tube) can be considered infinite with respect to the radius of the conductor. This permits the current density at any radial point,  $r$ , to be the same at any point,  $z$ , along the length. Differentiating the radial solution yields the Fourier Equation:

$$\frac{\partial^2 \vec{F}_z}{\partial \vec{x}^2} + \frac{1}{x} \frac{\partial \vec{F}_z}{\partial \vec{x}} + \vec{F}_z = 0. \quad (2-7)$$

where  $\vec{F}_z$  is a variable of integration and  $\vec{x} = \vec{k} \cdot r$ . For a good conductor,  $\vec{k}$  is equal to the phase constant,  $\vec{\beta}$ , where  $\vec{\beta}$  is defined as:

$$\vec{\beta} = (1-j)\sqrt{\pi f \mu \sigma} . \quad (2-8)$$

Solutions to the Fourier equation are well known Bessel Functions of zero order, first and second kind ( $J_0$  and  $N_0$ , respectively):

$$A_z(r) = D_1 J_0(\vec{\beta}_1 r) + D_2 N_0(\vec{\beta}_1 r) \quad (2-9)$$

---

<sup>70</sup> Ronold W. P. King, *Fundamental Electromagnetic Theory*, 2nd Ed. (New York: Dover Publications, 1963), pp. 350-356.

$A_z(r)$  is evaluated for each region depicted in Figure 2-4. If  $(\vec{k}_3 b)^2 \ll 1$  (a good assumption for the diameter of tube and conditions in a vacuum), then  $A_z(r)$  is equal to a constant. The fundamental electric vector,  $E_z$ , is related to the potential vector by:

$$\vec{E}_z(r) = \frac{-j\omega \vec{k}^2}{\partial r} A_z(r) \quad (2-10)$$

and the current density is simply:

$$\vec{i}_z = \sigma \vec{E}_z. \quad (2-11)$$

Since  $A_z(r)$  is constant,  $\frac{d\vec{E}_z(r)}{dr}$  is equal to zero. Substituting (2-10) into (2-9), differentiating and evaluating the constants of integration at the boundaries,  $r=b$  and  $r=c$  yields:

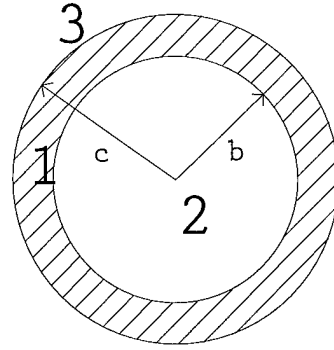


Figure 2-4: Tubular Conductor

$$\vec{E}_z(c) = \vec{D} \left[ J_0(\vec{\beta}_1 c) N_1(\vec{\beta}_1 b) - N_0(\vec{\beta}_1 c) J_1(\vec{\beta}_1 b) \right] \quad (2-12)$$

The final constant of integration,  $\vec{D}$ , is eliminated by taking the ratio of  $\vec{E}_z(r)$  to  $\vec{E}_z(c)$ . Substituting the expression for the current density given by equation (2-11) into this ratio, integrating over the area of the conductor from b to c and rearranging yields the current density as a function of total applied current,  $\vec{I}_z$ :

$$\vec{i}_z(r) = \frac{\vec{I}_z}{\pi c} \left( \frac{\vec{\beta}_1}{2} \right) \left\{ \frac{J_0(\vec{\beta}_1 r) N_1(\vec{\beta}_1 b) - N_0(\vec{\beta}_1 r) J_1(\vec{\beta}_1 b)}{J_1(\vec{\beta}_1 c) N_1(\vec{\beta}_1 b) - N_1(\vec{\beta}_1 c) J_1(\vec{\beta}_1 b)} \right\}. \quad (2-13)$$

$J_1$  and  $N_1$  are Bessel Functions of the first order, first and second kind. The skin depth is simply the inverse of the magnitude of  $\vec{\beta}_1$ :

$$\delta_s = |\vec{\beta}_1| = \frac{1}{\sqrt{\pi f \mu \sigma}} \quad (2-14)$$

Figure 2-5 plots the current density for various values of  $\beta b$  through the tubular wall for the alloy 600 Heat 96834 sample tube dimensions. Since the material factors which influence  $\vec{\beta}_1$  cannot be altered except by substituting sample material,

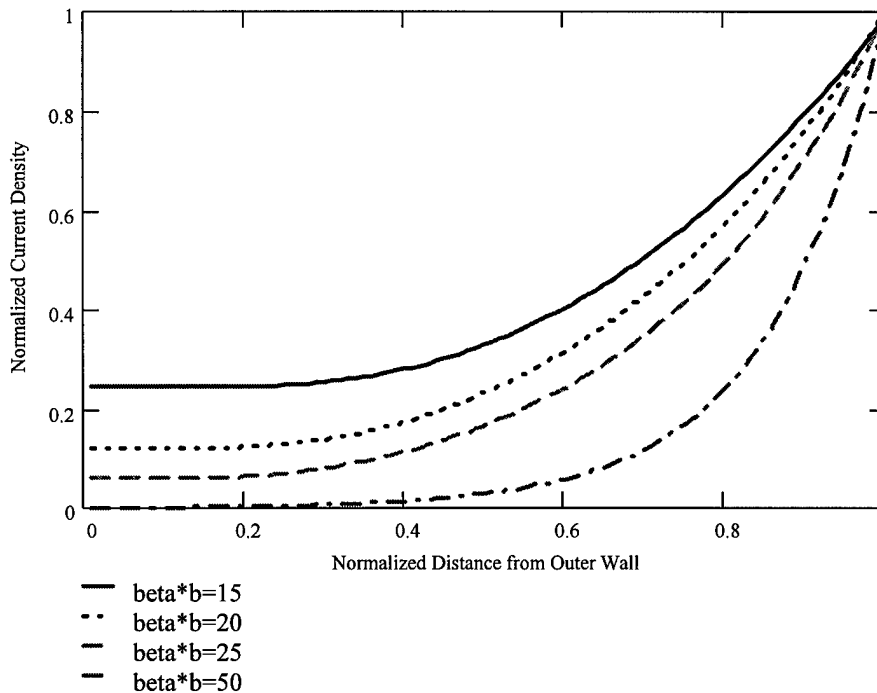


Figure 2-5: Current Density as a Function of Distance from the Exterior Wall of a Tubular Conductor for Various Values of  $\beta b$

Figure 2-5 clearly shows the dependence of the skin depth upon frequency. For highly ferro-magnetic materials, even low frequencies will generate an appreciable skin effect, while non-ferro magnetic materials (such as alloy 600) must use much higher frequencies to generate any skin effect. At values of  $\vec{\beta}_1 b$  below 10, the current density approaches an even distribution, typical of direct current, as one would expect.



Given the current density as calculated from equation (2-12), the potential drop between any two points on the conductor equals<sup>71</sup>:

$$E = I (R + j\omega L) = \frac{l}{\sigma} \vec{i}_z \quad (2-15)$$

If  $\beta_1 b$  is large resulting in significant skin effects (generally greater than or equal to 10 as discussed above) and the wall is sufficiently thick compared to the skin depth<sup>72</sup> ( $c - b \geq 4d_s$ ), then it can be shown that the surface impedance,  $Z_s$ , equals:

$$Z_s = \frac{2\pi c E_z(c)}{I_z(c)} = 2\pi z_i \quad (2-16)$$

where  $z_i$  is the internal impedance given by:

$$z_i = \frac{\beta_1}{2\pi c \sigma} \frac{1+j}{\sqrt{2}} \quad (2-17)$$

Substituting (2-16) into (2-15) and relating to (2-14) yields:

$$R = \omega L = \frac{1}{d_s \sigma} \quad (\text{per unit length}) \quad (2-18)$$

or, more simply, the impedance is proportional to  $\sqrt{f}$ . This allows the potential drop to be increased at the surface of an AC system by increasing the frequency of the signal for a constant current through the conductor, thus increasing the sensitivity to small impedance changes.

Application of the above theory to a potential drop system illustrates the advantages of such a system. As a crack develops of depth  $a$ , the length of current travel along the

---

<sup>71</sup> I. Verpoest, E. Aernoudt, A. Deruyttere, and M. Neyrinck, "An Improved A.C. Potential Drop Method For Detecting Surface Microcracks During Fatigue Tests of Unnotched Specimens," *Fatigue of Engineering Materials and Structures*, Vol. 3 (1981), pp. 206-209.

<sup>72</sup> Ronold W. P. King, *Fundamental Electromagnetic Theory*, 2nd Ed. (New York: Dover Publications, 1963), p. 357.

surface is increased by  $2a$ . The potential drop increases by a ratio of  $\left(1 + \frac{2a}{l}\right)$  according to equation (2-14). The measured potential drop can be a significant change if the applied frequency is high resulting in high surface impedance (equation 2-17). If the skin depth is large compared to the wall thickness however, the measured potential may be small owing to a relatively low surface impedance, though any skin effect will enhance the detection over resistance changes due to area changes required for DC system operation. The potential drop sensitivity to small changes in surface impedance of AC systems when applied to crack detection has achieved a sensitivity as small as  $50\mu\text{m}$  in crack depth<sup>73</sup>.

There is a consequence of the application of high frequency AC signals which must be considered. It has been found<sup>74</sup> during operation of AC potential systems that an error proportional to  $f$  vice the  $\sqrt{f}$  is induced on the measured potential. This voltage error is attributed to "inductive pickup". The higher the frequency employed, the larger the inductive effect. The leads which attach to the tubular conductor form a coil (Figure 2-6). This coil generates an oscillating magnetic field and associated voltage on the

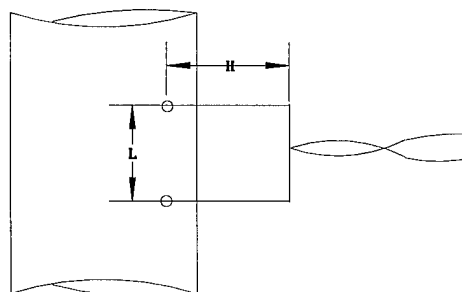


**Figure 2-6: "Inductive Coil" Setup by Pick-Up Wires on the Tube**

<sup>73</sup> I.S. Hwang, "Embrittlement Mechanisms of Nickel-Base Alloys in Water" (Ph.D. dissertation, Department of Nuclear Engineering, Massachusetts Institute of Technology, 1987), p. 101.

<sup>74</sup> F.D.W. Charlesworth and W.D. Dover, "Some Aspects of Crack Detection and Sizing using A.C. Field Measurements," *The Measurement of Crack Length and Shape During Fracture and Fatigue*, ed. C. J. Beevers (West Midlands, UK:EMAS, 1982), p. 258.

conductors (wire and tube). This inductive "load" can reduce the sensitivity of the system by raising the "noise" level of the received potential measurement. The higher potential level requires a greater change in  $I$ , thus a larger crack penetration, for crack detection. For non-ferro-magnetic materials, this error can be near 100% of the applied voltage<sup>75</sup>.

In summary, the AC potential drop method has proved superior to the DC potential drop method for use in high temperature and pressure, corrosive environments. In DC potential drop, large currents are required to obtain a potential drop which is measurable. For sensitivity to crack size, the current must be stable to within 0.01%, which is difficult at the required high currents<sup>76</sup>. Additionally, thermoelectric effects from these currents result in a bias of the measured potential.

Shortcomings of the DC potential drop technique are overcome by using an alternating current source. The AC current yields an increased potential drop for the same applied current, provides noise rejection and is more sensitive to a given crack size than DC potential drop. The ability to vary the frequency, limited only by available equipment, allows the sensitivity to be further improved by taking advantage of skin effect.

Several shortcomings of the AC potential drop technique must also be considered. Use of the AC potential drop technique requires well-insulated probe leads, and sensitivity

---

<sup>75</sup> Ibid., p. 258.

<sup>76</sup> I.S. Hwang and R.G. Ballinger, "A multi-frequency AC potential drop technique for the detection of small cracks," *Measurement Science Technology*, Vol. 3, (1992), p. 63.

is a function of probe spacing. Inductive effects, especially at higher frequencies, can result in induced voltages in the probe leads. These induced voltages can mask potential changes due to crack initiation and growth, thereby decreasing sensitivity. Thus a tradeoff must be made between induced voltages and increasing current densities for optimal crack sensitivity. Further, the non-magnetic properties of alloy 600 (as well as many other alloys) require the use of high frequencies to take advantage of the higher current densities present from skin effect. The larger skin effect depths require a reduction in the probe spacing to maintain the same sensitivity as in a magnetic material. This obviously requires the area of crack initiation to be localized during any experimental observations.

## **2.5 Present Research**

The literature clearly identifies many possible factors influencing IGSCC in alloy 600. Experiments conducted by the numerous researchers cited have presented IGSCC data for alloy 600 based on standard ASTM test samples, C-rings or wires tested in a laboratory environment. Actual detection of IGSCC in-situ and the stress conditions present during initiation have not been measured. Additionally, no test data is available for steam generator tube samples subjected to laboratory experiments for comparison to these parameters.

The focus of the present research was separated into two phases. During phase one, an experimental test apparatus capable of duplicating an in-situ steam generator environment and subjecting alloy 600 tube samples to various wall stresses was constructed. The goal of the testing was to prove crack detection in alloy 600 tubes under in-situ conditions was possible using an ACPD system.

In phase two, actual alloy 600 tubing crack growth rate data for various applied stress intensities was collected for comparison to the literature results. Use of the ACPD system allowed monitoring of the crack growth rate while subjecting the tube to various stress intensities.

### 3. Experimental Apparatus

An autoclave system provides the environment necessary to accelerate the formation of stress corrosion cracks on a sample tube from the normal in-situ steam generator environment. The system allows for monitoring of the sample tube with an Alternating Current Potential Drop (ACPD) system and control functions to maintain environmental conditions and safety. The system was designed to allow a sample tube to be internally pressurized to approximately 150% of yield strength and maintained at a temperature of  $315 \pm 1^\circ\text{C}$ . The operating fluid is 0.1%  $\text{Na}_2\text{CO}_3$  and 10%  $\text{NaOH}$  by weight which equates to a pH of 10 at  $315^\circ\text{C}$ . A similar system was developed to detect crack initiation successfully in a neutral environment at room temperature<sup>1</sup>. Further, the system includes the capability to inject inhibitors and evaluate their ability to arrest crack growth. The autoclave system is illustrated schematically in Figure 3-1.

#### 3.1 Mechanical System Description

The mechanical portion of the system consists of four components: (1) the autoclave and heating system (2) an autoclave recirculation loop (3) a static pressurization system and (4) a sample pressurization system. The autoclave system is designed to maintain the autoclave fluid subcooled in either a recirculation or static operating mode. The system may be operated in either mode with no mechanical alterations required,

---

<sup>1</sup> Il Soon Hwang, "Embrittlement Mechanisms of Nickel-Based Alloys in Water," PhD Dissertation (Massachusetts Institute of Technology, 1987), pp. 96-121.

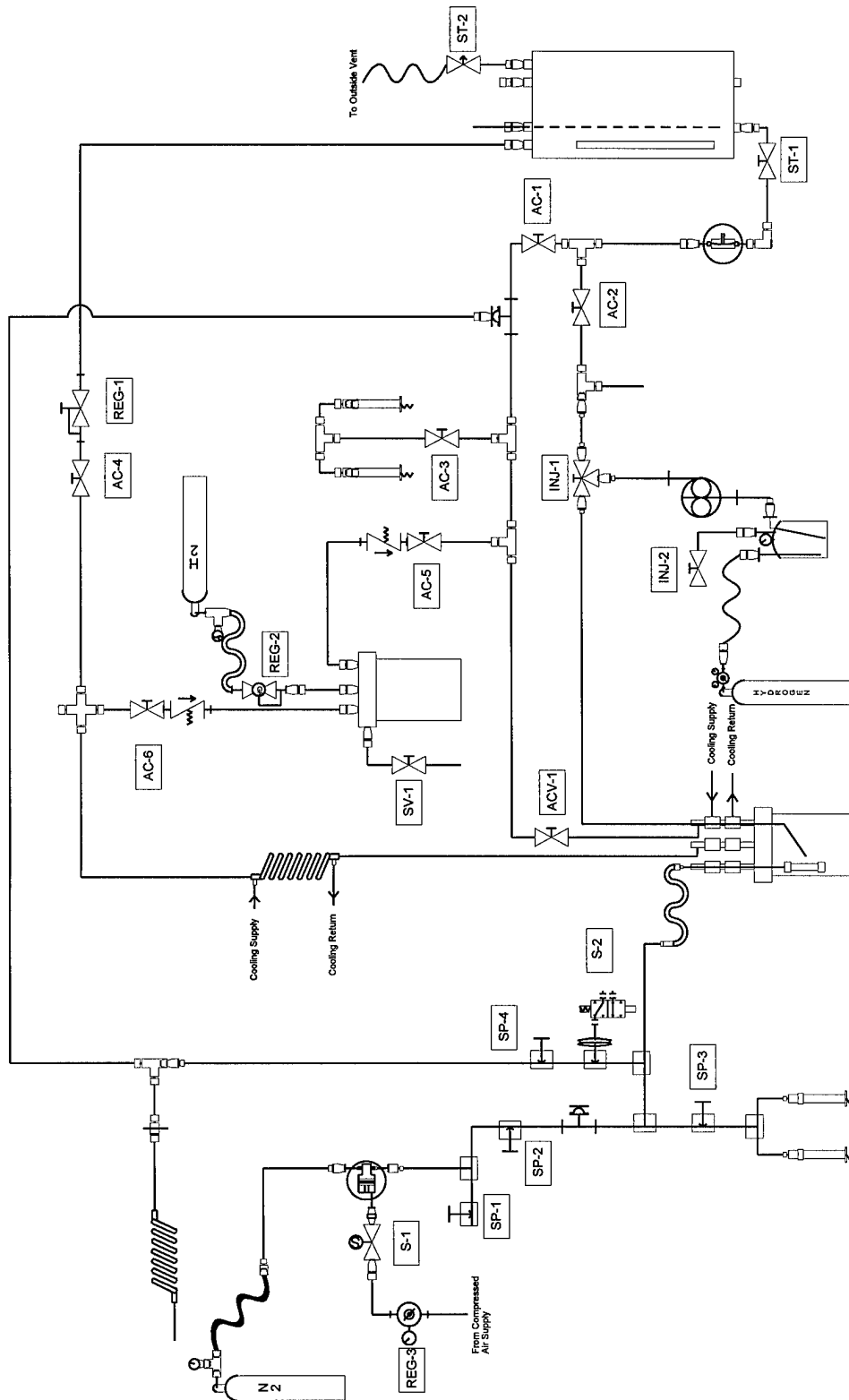


Figure 3-1: Autoclave System Showing Recirculation, Static and Pressurization Systems

Additionally, the mechanical system incorporates several safety and control features. Detailed construction drawings are contained in Appendix 3.

### 3.1.1 Autoclave and Heating System

A one gallon, nickel-200 autoclave is used to contain the sample tube, heat the caustic solution to 315°C and provide the required strength to maintain the caustic solution at a subcooled pressure. The vessel has a maximum allowed working pressure of 12.4 MPa (1800 psig) at 315°C. The autoclave has a bolt-on head that has been modified with the addition of six one foot long nipples. The nipples are machined from nickel-200 bar stock that has been bored with a 6.4 mm (0.25 in) hole. The nipples are inserted into the autoclave head and welded and have a 1/4

National Pipe Thread (NPT) male thread machined into the opposite end. The nipples provide fittings for connecting the recirculation and static systems, penetrations for the ACPD electrical connections, sample pressurization tube and dual junction thermocouple. Each nipple has an external copper and bronze cooling jacket to maintain the stainless steel fittings

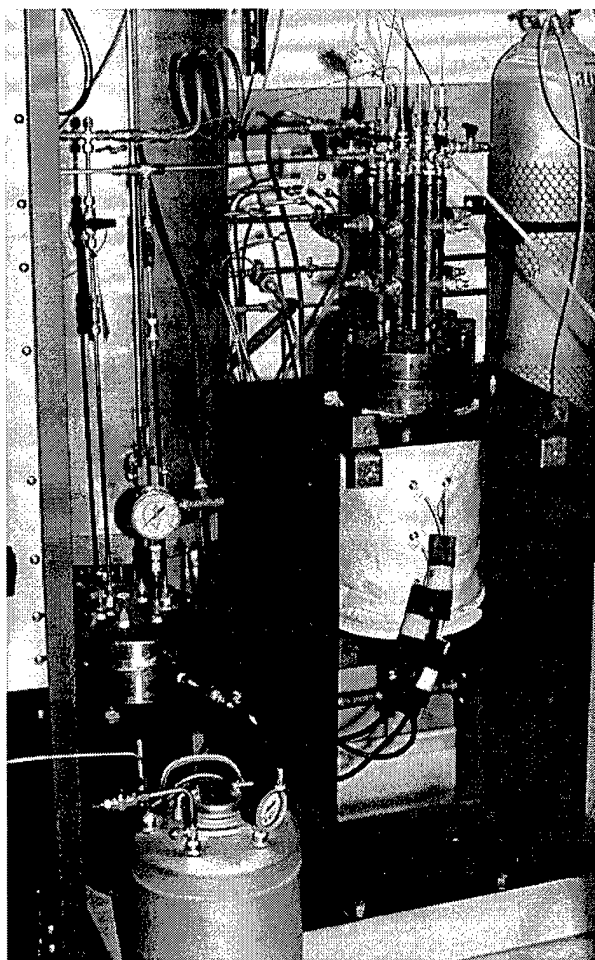


Figure 3-2: Autoclave with Heating Mantle Showing Recirculation and Static System Connections



below 100°C, averting possible failure from caustic stress corrosion. The cooling jackets are provided with chilled water from the building chilled water system.

The autoclave is heated by an external heating mantle. The mantle has a maximum heat output of 2700 watts from three elements in the mantle which are supplied with 250 volts each. Control of the mantle heat output is by turning any one or all of the elements on and off.

### 3.1.2 Recirculation Loop

When operating in recirculation mode, the necessary liquid pressure and flow rate are developed by a Model 610 Pulsa-feeder pump. This pump is a positive displacement, wormgear reduction diaphragm pump capable of a maximum flow rate of 20 ml/min. (0.31 gph) at a head up to 20 MPa (3000 psig). To simplify operation, the pump is made self-priming by locating the suction below a 200 liter storage tank.

All tubing used to deliver the working fluid to and from the autoclave is commercially procured 6.4 mm (0.25 in) x 1.6 mm (0.065 in) wall 316 stainless steel tubing rated at 70 MPa (10,000 psig) working pressure and conforming to ASTM standard A269/A213.

All fittings used to assemble the tubing are Parker stainless steel CPI/A-Lok (working pressure rating of 70 MPa) or National Pipe Thread (NPT) (minimum working pressure of 42 MPa (6100 psig)).

All isolation valves are Parker ball valves with 316 stainless steel bodies and Teflon or Kel-F seats. The maximum working pressure of any isolation valve is 20 MPa (3000 psig), minimum.

A backpressure regulator, Tescom model 26-1724-24, on the fluid return line from the autoclave, maintains the desired fluid pressure in the autoclave. The regulator is stainless steel with teflon seats and is rated from 0 to 17.2 MPa (2500 psig).

A 200 liter (50 gallon) stainless steel tank with a quartz sight glass provides a supply and return reservoir. Purging and agitation of the fluid stored in the tank are accomplished via a 6.4 mm (0.25 in) nickel tube incorporated into the tank. An inert gas supply is attached to the end fitting and is bubbled through the fluid. The tank can be pressurized to a maximum pressure of 68 kPa (10 psig) and vented through a Parker CPI fitting at the tank top. The tank sits on a stand to allow easy access to the recirculation pump isolation valve and to a Conax® fitting, which allows internal potentials to be monitored.

### 3.1.3 Static System

In static mode operation, the system is pressurized with Grade 5 hydrogen. A gap of at least 25 mm (1 in) is maintained below the autoclave head as a gas space. The pressure source is a 40 MPa (6000 psig), 14000 liter (500 ft<sup>3</sup>) Grade 5 hydrogen bottle procured from a commercial vendor. A transfer hose, normally used in hydraulic applications, which is non-conducting and rated to 70 MPa (10,000 psig) directs the gas to a regulator. Pressure in the tank is monitored by a mechanical gauge attached at the outlet.

The pressure in the autoclave is maintained by a gas regulator obtained from Grove, Inc., model 15LHX. It has a stainless steel casing with stainless steel internal components and has a working pressure range from 0 to 41.3 MPa (6000 psig).

The regulator has a relief feature which allows pressure to be maintained within the desired range once set. Outlet gas from the regulator travels via a scrubber before reaching the autoclave.

A scrubber is used to prevent hot caustic from reaching the regulator when gas is relieved from the autoclave to maintain the upper pressure setpoint. Hot caustic present in gas would quickly corrode the internal stainless steel regulator parts, resulting in regulator failure. The scrubber consists of a titanium 4 liter (1 gallon) autoclave (High Pressure Equipment Model BC-4) with a working pressure of 15.2 MPa (2200 psig). The autoclave is maintained cold and is filled 50% with deionized water. Returning gas passes through the water and is chilled by natural convection and conduction prior to entering the regulator for discharge to the atmosphere. During the cooling process, the caustic entrained in the hot hydrogen gas is condensed into the water.

Two Parker stainless steel check valves with a 70 kPa lift pressure prevent short circuiting of the scrubber by the return gas. The check valves have a working pressure of 20 MPa.

Tubing, fittings and valves used exclusively by the static system are identical to those described for use in the recirculation system.

#### **3.1.4 Sample Pressurization System**

Internal sample pressurization is accomplished with nitrogen. To obtain the required sample internal pressure, commercial Grade 4.8 nitrogen from a 8500 liter (300 ft<sup>3</sup>) gas bottle supplies a Haskel gas booster pump. The pump, Model AG 152, is capable of reaching pressures of 140 MPa (20,000 psig).

The outlet pressure is controlled using compressed air and a regulator.

All tubing in the sample pressurization system is 3.2 mm (0.125 in) by 0.9 mm (0.035 in) wall 316 stainless steel and is rated to a maximum allowed working pressure of 100 MPa (15,000 psig). A non-conductive hose, normally used in hydraulic applications, connects the sample with the pressurization system. The maximum allowed working pressure of the hose is 10000 psig.

All valves, except the diaphragm isolation valve, are Autoclave Engineer series 10V2, 316 stainless steel with allowed working pressures to 80 MPa (11500 psig). The diaphragm isolation valve is an air-to-close Autoclave Engineer Series 10V2 with a maximum working pressure of 75 MPa (11000 psig). This isolation valve is normally open and is shut by 275 to 480 kPa (40 to 70 psig) air pressure.

Fittings are Autoclave Engineer low pressure fittings with a maximum allowed working pressure of 80 MPa, Parker NPT fittings with maximum allowed working pressures of 50 MPa (7100 psig), and Boston Hydraulic fittings with maximum allowed working pressures of 70 MPa.

### **3.2 Control Systems**

Autoclave and sample pressures are monitored by pressure transducers, Model P-605, manufactured by Omega Engineering. The internal autoclave temperature is monitored from a dual junction Type K nickel sheathed thermocouple installed through the autoclave head. The transducers and one junction of the thermocouple provide input to six model DP-41E meters, also manufactured by Omega Engineering, which provide visual readout

and control functions. Additionally, the pressure readings are recorded and displayed versus time on a Gateway 486 microprocessor via a Hewlett Packard 3852A Data Acquisition and Control Unit.

Heater control is provided by an Omega Engineering CN9000 microprocessor controller. The controller is a proportional - integral-differential controller and is tuned to allow temperature to be maintained within a 1 degree Celsius band. Input for the controller is from the dual junction Type K nickel-sheathed thermocouple installed in the autoclave.

### 3.3 Safety Systems

The heater control and pressurization systems are interlocked to prevent startup if autoclave pressure conditions are not met and to shut down the system safely if autoclave pressure control is lost or a sample through-wall rupture occurs. The system logic electrically disconnects the autoclave heating system should subcooled conditions be lost, autoclave temperature rise above 325°C, nitrogen pressure fall to a low specification (variable dependent on desired wall stress) or autoclave pressure rise above 13.8 MPa (2000 psig). Additionally, if the logic circuit initiates a trip, air is isolated to the Haskel booster pump and the sample nitrogen pressure dumped via the diaphragm valve, preventing over pressurization of the sample. A common collection system equipped with an air cooling coil and collection bottle prevents hot caustic from becoming airborne. A schematic diagram of the interlock system is shown in Figure 3-3. A detailed wiring diagram is in Appendix 3.

The sample and autoclave pressurization systems are protected from over pressure by rupture disk assemblies. The

autoclave rupture disk is installed in the 6.4 mm tubing line between the recirculation pump and the autoclave and is not isolable from the static system when operated in that mode. It provides over pressure protection at 20 MPa. The Sample Pressurization system has a similar rupture disk which provides protection at 70 MPa.

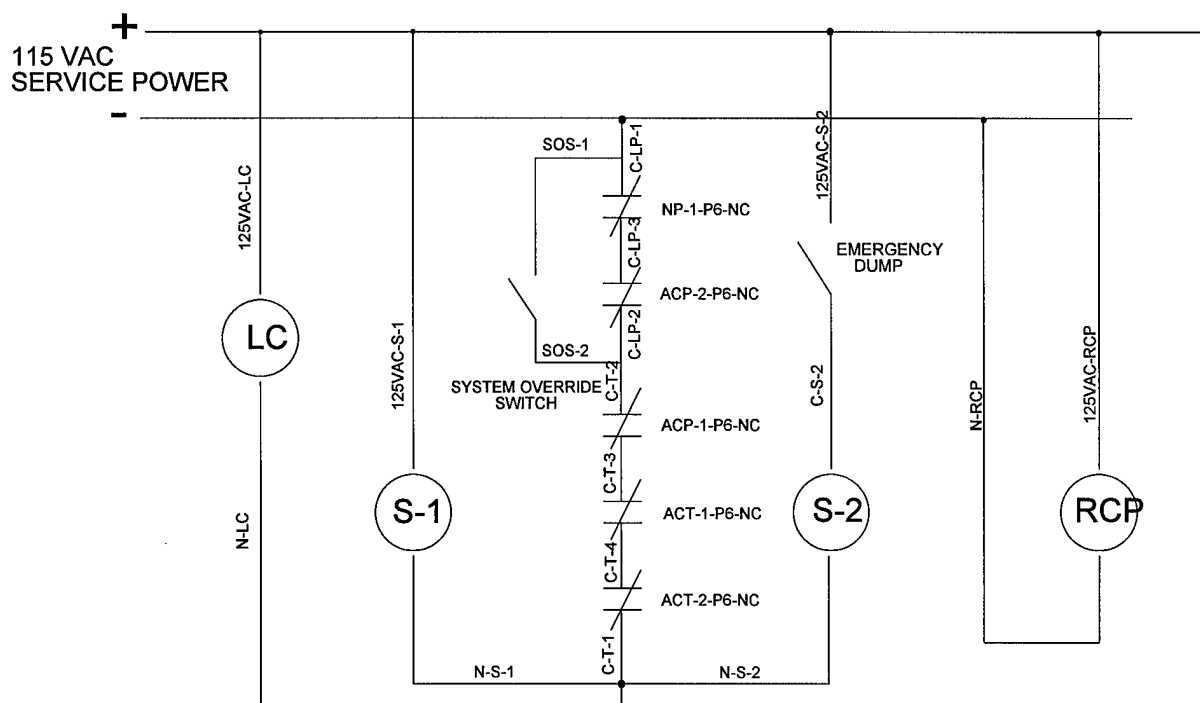


Figure 3-3: Interlock Control System Schematic

For personnel safety, the recirculation and pressurization systems are housed in a single cabinet open in the back and right sides for installation of services and maintenance. The cabinet also houses the Omega DP41 meters which are separated from the mechanical equipment and tubing by a Plexiglas spray shield. All wiring below the spray shield is contained in anti-corrosive, wet environment 13 mm flexible cable rated for this use. Polyethylene collecting pans are installed below the tank,

cabinet and pressure vessel to prevent caustic from reaching the tiled floor.

### 3.4 Test Sample

#### 3.4.1 Material

The material selected for use in this work is a 2.2 cm diameter alloy 600 tubing, heat number 96834, fabricated by Babcock and Wilcox Company, with a 1.4 mm wall thickness. The tubing has been low temperature annealed at  $927 \pm 14^\circ\text{C}^2$ . Important mechanical properties of this heat are contained in Table 3-1. This particular heat has demonstrated susceptibility to environmentally assisted cracking during in-service conditions.

Table 3-2 illustrates the composition of the as-tested material compared to the chemical composition provided by the manufacturer and the limiting chemical composition provided by Inco Alloys International for Inconel Alloy 600 compositions. The chemical composition of the as-tested material was determined by electron dispersive x-ray spectroscopy (EDX) (Figure 3-4).

Figure 3-5 illustrates the typical microstructure in three directions of alloy 600 Heat 96834, low temperature annealed material. The sample was prepared by polishing to a 1  $\mu\text{m}$  finish and electro-etching in a 5% nitric acid- 95% methanol solution at 3 volts for approximately 20 seconds. From Figure 3-5, this particular heat of alloy 600 shows an equiaxed grain structure

---

<sup>2</sup> R.G. Ballinger and I.S. Hwang, "Characterization of Microstructure and IGSCC of Alloy 600 Steam Generator Tubing," Final Report, EPRI TR-101983, (Palo Alto: Electric Power Research Institute, February 1993), p. 2-1.

with an average grain size of  $35\mu\text{m}^3$ . Figure 3-6 is an SEM micrograph of the tubing oriented in the longitudinal (L) direction showing a large number of intragranular precipitates. These precipitates have been investigated<sup>4</sup> and found to be primarily carbides. Additionally, discontinuous carbides also reside at the grain boundaries.

$Y_s$ (MPa)	$U_s$ (MPa)	$\nu$	$\sigma$ (mho/m)	$\mu$ (H/m)
335	744	0.3	$0.97 \times 10^6$	$1.26 \times 10^{-6}$

Table 3-1: Mechanical Properties of Heat 96834

	Ni	Cr	Fe	C	Mn	S	Si	Cu
Limiting Chemical Composition <sup>5</sup>	72% min	14- 17%	6- 10%	0.15 max	1.0 max	0.015 max	0.5 max	0.5 max
B&W 96834 Manufacturer Composition <sup>6</sup>	74.97	15.8 4	8.03	0.04	0.26	0.001	0.3	0.0 2
EDX Analysis Composition	72.9	18.4	8.1	*	0.1	*	0.5	*

\* Composition not detected

Table 3-2 : Chemical Composition of Alloy 600

<sup>3</sup> R.G. Ballinger and I.S. Hwang, "Characterization of Microstructure and IGSCC of Alloy 600 Steam Generator Tubing", Final Report, EPRI TR-101983 (Palo Alto: Electric Power Research Institute, February 1993), p. 3-56.

<sup>4</sup> I.S. Hwang, "Embrittlement Mechanisms of Nickel-Base Alloys in Water" (Ph.D. dissertation, Department of Nuclear Engineering, Massachusetts Institute of Technology, 1987), p. 187.

<sup>5</sup> Inconel, Inco Alloys International (Huntington, WV:Inco Alloys International, Inc.).

<sup>6</sup> R.G. Ballinger and I.S. Hwang, "Characterization of Microstructure and IGSCC of Alloy 600 Steam Generator Tubing", Final Report, EPRI TR-101983 (Palo Alto: Electric Power Research Institute, February 1993), p.2-2.



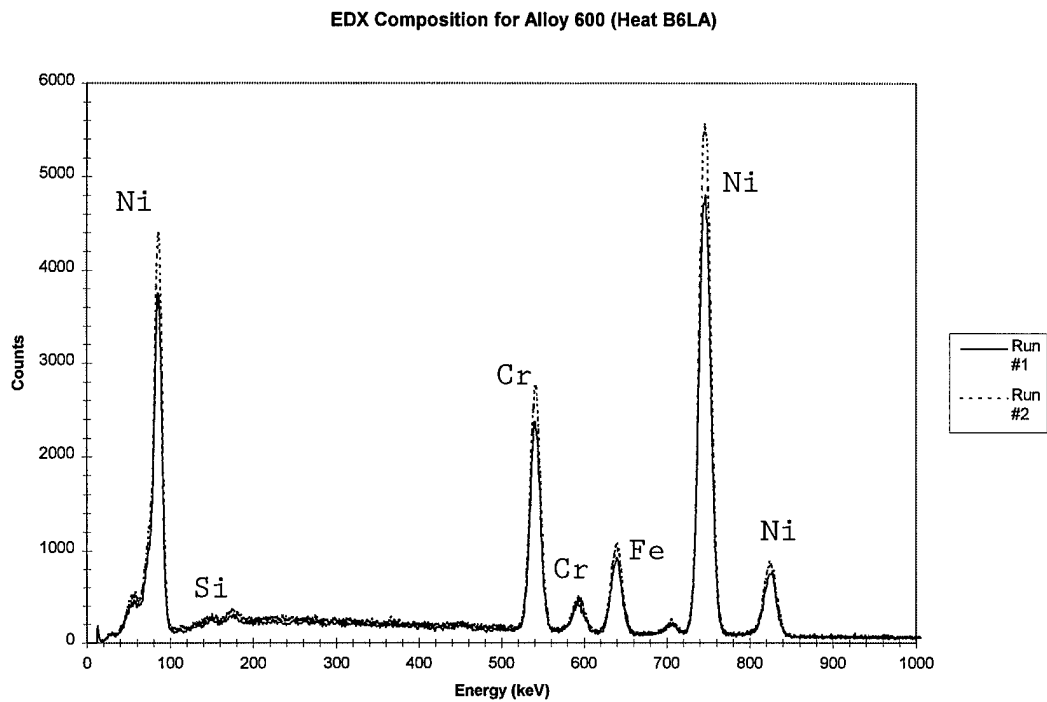


Figure 3-4: EDX of alloy 600 Heat 96834 (Low Temperature Anneal)

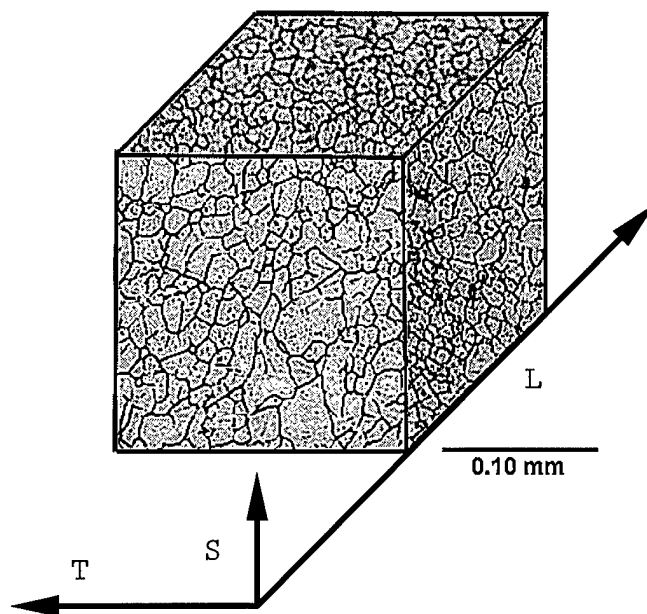


Figure 3-5: Three Dimensional SEM Micrograph of Heat 96834 (longitudinal, L; transverse, T; short transverse, S).

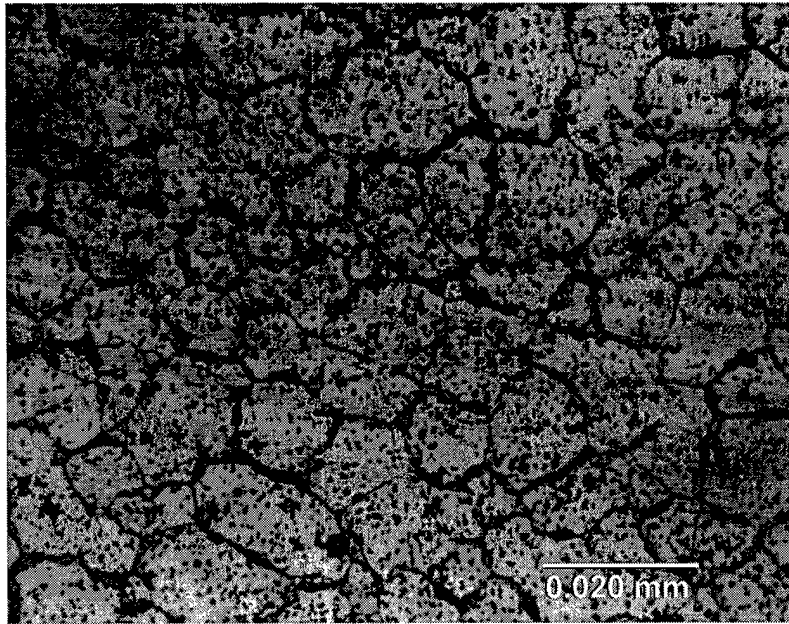


Figure 3-6: Heat 96834 SEM Micrograph Showing Intragranular Precipitates

#### 3.4.2 Sample Construction

The test sample is a 10 cm long section of steam generator tube with a cap welded to each end. A ceramic spacer is placed in the interior of the sample to minimize the pressurization volume. On one endcap, a 3.2 mm hole is drilled and a 3.2 mm by 0.9 mm tube, approximately 50 cm long, is welded into the joint. This tube connects the nitrogen pressurization system to the test sample.

Two sets of samples were manufactured. The first had a 2 cm wide band around the center of the interior wall thinned to 0.8 mm. This enabled higher wall stresses to be obtained at lower internal nitrogen pressures. The second set of samples had a fatigue crack induced at the test area of the sample. This pre-crack allowed accurate predictions of initial stress

concentrations to be made. A detailed discussion of this method can be found in the experimental procedures section.

Figure 3-7 shows a simplified schematic of the two test samples. Appendix 3 contains the detailed schematics.

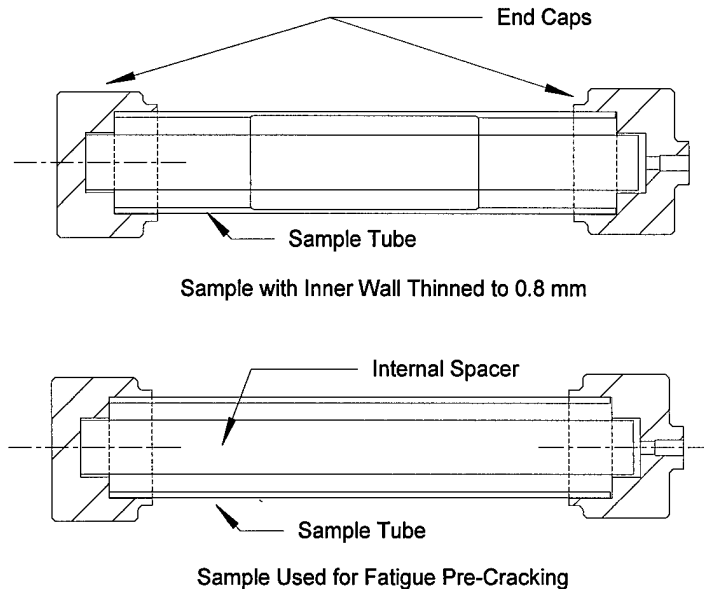


**Figure 3-7: Simplified Schematic of Test Samples Illustrating Machining Differences in the Tube Sections**

### 3.5 Alternating Current Potential Drop (ACPD) System

The ACPD system is based on one developed by Hwang<sup>7,8</sup>. The actual system cabinet is shown in Figure 3-8. A schematic diagram is shown in Figure 3-9. Data collection is automated and no operator intervention is necessary once the system is started. One significant improvement is the use of a Gateway

---

<sup>7</sup> Il Soon Hwang, "Embrittlement Mechanisms of Nickel-Based Alloys in Water," PhD Dissertation (Massachusetts Institute of Technology, 1987), pp.96-121.

<sup>8</sup> R.G. Ballinger, and I.S. Hwang, "Characterization of Microstructure and IGSCC of Alloy 600 Steam Generator Tubing," Final Report, EPRI TR-101983, (Palo Alto: Electric Power Research Institute, February 1993), p. 2-54.

486 Personal Computer using LABVIEW®. This software provided a better graphics display and simplified final data analysis.

The ACPD system provides a multifrequency capability through the use of a Hewlett Packard Multi-Frequency Function Generator (Model 3325A). The input signal to the test sample is provided by a high stability AC current driver, Model 465-35, manufactured by Perry Amplifier, which combines an operator selectable DC input signal with the AC output of the Multi-Frequency Function Generator. The output signal from the test sample is amplified by a Perry Amplifier Model 675D Low Impedance Pre-Amplifier. The signal is discriminated against background noise by a microprocessor controlled, high sensitivity Princeton Applied Research Model 5301 Lock-in Amplifier and passed to the Gateway 486 PC through a Hewlett Packard Model 3488A Switch Control Unit.

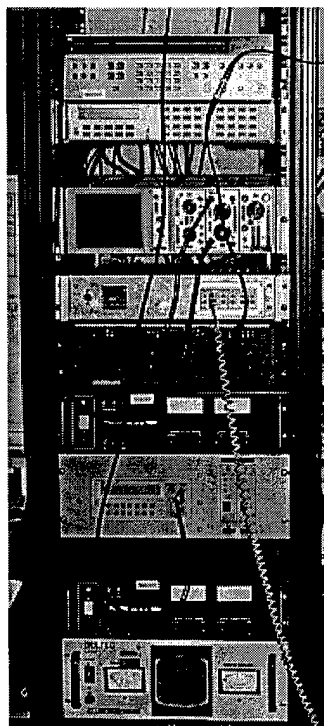


Figure 3-8: ACPD Test Stand

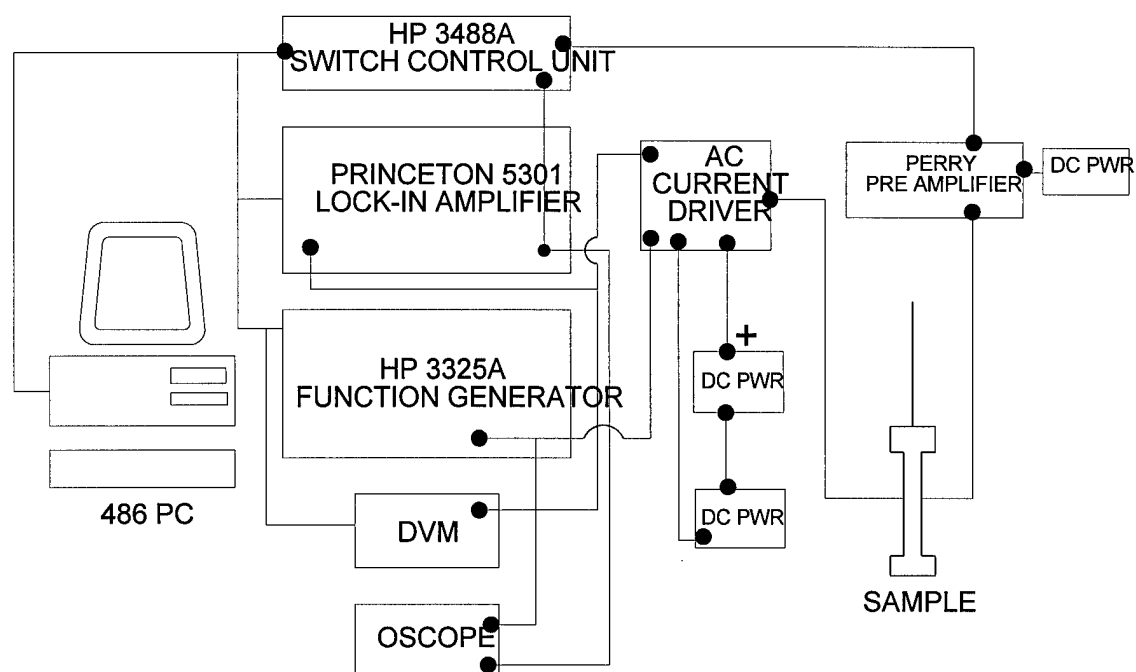


Figure 3-9: ACPD System Schematic

#### 4. Experimental Procedure

The experimental program was divided into two distinct phases. During phase one, the ACPD system proof of principle was to be accomplished. In phase two, the focus was on crack initiation and growth on tubing. To expedite the SCC initiation and growth process, a fatigue pre-crack was induced in the samples for phase two. The system operation remains identical in both cases. Detailed step by step operating procedures are in Appendix 2.

##### 4.1 ACPD Proof of Principle Testing

During phase one, the goal was to demonstrate the ability of the ACPD system to detect cracks in conditions similar to in-situ steam generator conditions. The system was operated in static mode for this phase of testing. Figure 4-1 shows a welded test sample. Approximately 2 cm of the interior wall was thinned to 0.8 mm to allow a greater stress range to be applied without exceeding the pressurization system specifications. Detailed construction drawings are in Appendix 3.

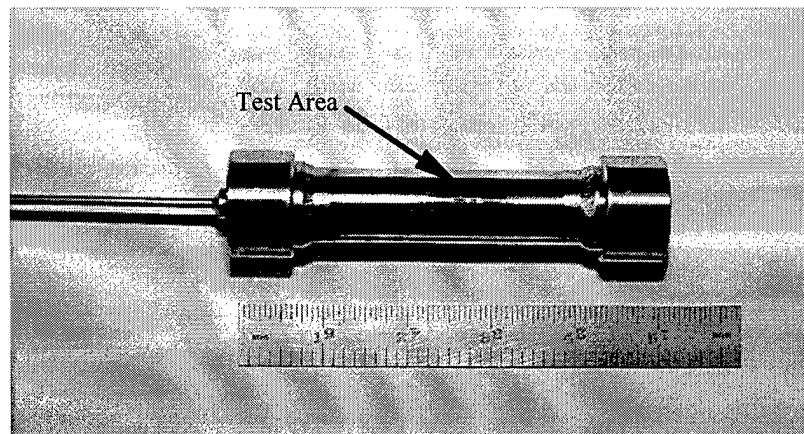
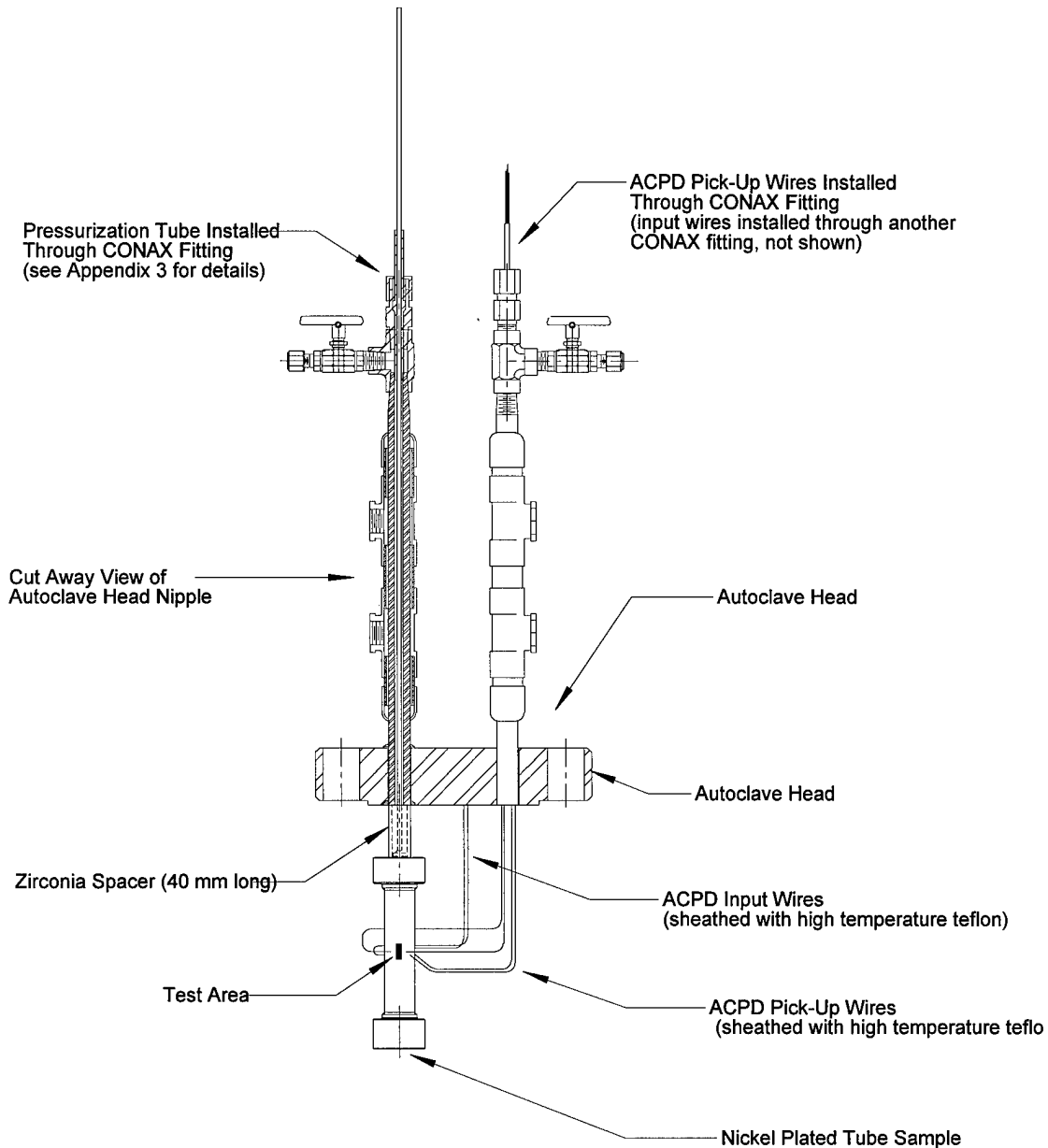


Figure 4-1: Welded Test Sample.

After welding, the sample was electroless nickel plated in all areas except a small area in which crack initiation was expected. The plating prevented SCC initiation at sites beyond that monitored by the ACPD test probes. Crack initiation and growth were expected in the axial direction since the hoop stress is greater by a factor of two than the axial stress in the cylinder. The test site consisted of an area no greater than 1 mm across in the circumferential direction to improve crack detection sensitivity, by 3 mm wide in the axial direction, roughly the weld contact area of the output probes to the ACPD system. This area was masked off with Miccro Super XP 2000 micro-stop and allowed to dry 24 hours to ensure mask cohesion.

Electrical isolation of the sample and ACPD probes was necessary to maximize output gain from the ACPD. Figure 4-2 shows schematically the sample tube installation into the autoclave head. If grounds exist, current across the test site is reduced and overall potential drop is lowered. The sample was electrically isolated along the pressurization tube by encasing the tube in High Operating Temperature Teflon (TFE) (Alpha Wire Corporation, No. FIT-500). This teflon insulation was also used on all input and output ACPD leads to the sample. The sample was passed through one of the autoclave head nipples via an electrically isolable Conax® fitting (Conax Corporation catalog number EGT-125-A). ACPD system input (one set) and output (test and reference area) probe wires were similarly passed through separate nipples to prevent inductive interference and through Conax® fittings TG-24-A4.



**Figure 4-2: Schematic of Sample Tube Installed Into Autoclave Head**

The input and output probe wires were then welded to the sample. The input probes were welded along the same axial plane as the test area at approximately  $\pm 90$  degrees azimuth. The reference area was chosen along the same axial plane between one input probe and the test area. Input wire spacing for the reference area should be the same as the test area to



provide initially identical potential drop signals. Figure 4-3 shows the completed head and sample assembly. The entire sample, less the masked off test area, was then nickel plated using a plating procedure developed by Morra for surface specimen preservation<sup>1</sup> (detailed procedure is in Appendix 2).

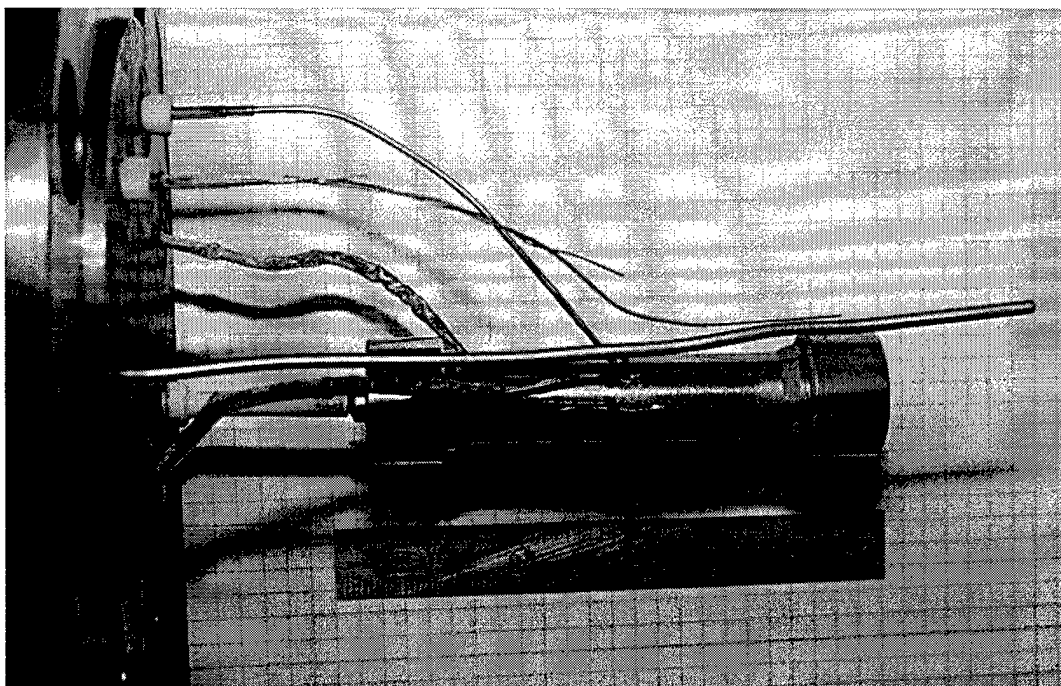


**Figure 4-3: Sample Assembled into Autoclave Head Showing ACPD Input and Output Wires, Thermocouple, Level Sensing and Nickel Reference Electrode**

Following completion of the plating process, the masking was removed from the test area. A small sharp surface scratch was placed in the test area to aid in stress concentration. The thermocouple (not electrically isolated), nickel reference electrode and several wires for fluid level measurement by

---

<sup>1</sup> M. M. Morra, J. M. Morra and R. R. Biederman, "A Technique for the Preparation of Powders for Examination by Transmission Electron Microscopy", *Materials Science and Engineering*, A124 (1990) pp. 55-64.

potential were installed in the head following the procedures used for the ACPD wire installation.

The caustic solution was prepared using 10% NaOH and 0.1%  $\text{Na}_2\text{CO}_3$  by weight in deionized water. The  $\text{Na}_2\text{CO}_3$  was added to accelerate the corrosion process<sup>2</sup>. 2600 ml of solution was prepared and added to the autoclave to allow for a minimum of 3 cm (1.5 inches) of gas volume at the top.

The head assembly was installed and torqued to 170 to 190 N-m (125 to 140 ft-lbs). Cooling tubes were attached to the head nipples. All external tubing connections for the static/recirculation system were attached to provide the hydrogen pressurization path. Electrical connections to the thermocouple and polarization system were completed. ACPD constant current transformer outputs were connected to the probe input leads. The reference and test area leads were each connected to a separate Perry preamplifier. The ACPD system was started and output signals observed for stability (noise, transients and signal level) using an oscilloscope and monitoring the computer output.

The system and autoclave volume were purged of oxygen with grade 5 hydrogen. Purging consisted of flowing hydrogen at 15 kPa (about 2 psig) through the Parker tee on the outlet tube and exhausting through each nipple vent (ACV-1 through 6) for approximately 15 minutes each. An alternate purge consisted of using the hydrogen supplied to the scrubber and again exhausting through each nipple vent for 15 minutes. The system

---

<sup>2</sup> R. Bandy, R. Roberge, and D. van Rooyen, "Intergranular Failures in Alloy 600 in High Temperature Caustic Environments," *Corrosion-NACE*, Vol. 41 No.3 (March 1985), pp. 142-151.

was then pressurized to 3.5 MPa (500 psig) through the scrubber by opening REG-2 and leak checked at all fittings.

Detailed system startup procedures are in Appendix 2. The system hydrogen overpressure was raised to  $12.4 \pm 0.5$  MPa ( $1800 \pm 50$  psig). The heating circuit was energized and autoclave temperature raised to  $315 \pm 1^\circ\text{C}$ . Once at temperature, the ACPD signals were again monitored for stability. The desired stress across the wall was obtained by operating the sample nitrogen pressurization system to obtain the desired differential pressure. During this phase of testing, internal nitrogen pressure was raised to approximately 45.5 MPa (6600 psig) to provide a nominal wall stress of 140%.

To aid in SCC initiation, the sample potential was polarized anodically with respect to the nickel autoclave. As seen in Figure 4-4, the corrosion current is significant at potentials greater than +150 mV versus nickel. In fact, previous testing has shown that SCC does not occur at potentials below +100 mV versus nickel<sup>3</sup>. Due to the relatively large surface area of the test sample, a DC constant voltage power supply (Hewlett Packard Model 6023A) was used. The positive terminal was attached to the sample pressurization tube and the negative terminal to the autoclave (counter-electrode). The potential versus nickel was monitored using the electrically isolated nickel electrode installed through the autoclave head and a high impedance voltmeter (Keithly

---

<sup>3</sup> J. B. Lumsden, S. L. Jeanjaquet, J. P. N. Paine and A. McIlree, "Mechanism and Effectiveness of Inhibitors for SCC in a Caustic Environment," *Seventh International Symposium on Environmental Degradation of Materials in Nuclear Power Systems - Water Reactors*, Vol. 1, (Breckenridge, CO: NACE International, August 7-10, 1995), pp. 317-325.

Programmable Electrometer, Model 617). Potentials were maintained between +150 mV and 220 mV versus nickel during this phase of testing. If drift in the applied potential is noted during the course of the test due to the lack of a feedback loop to the power supply, adjustment to the applied potential must be made to prevent drifting outside the desired band.

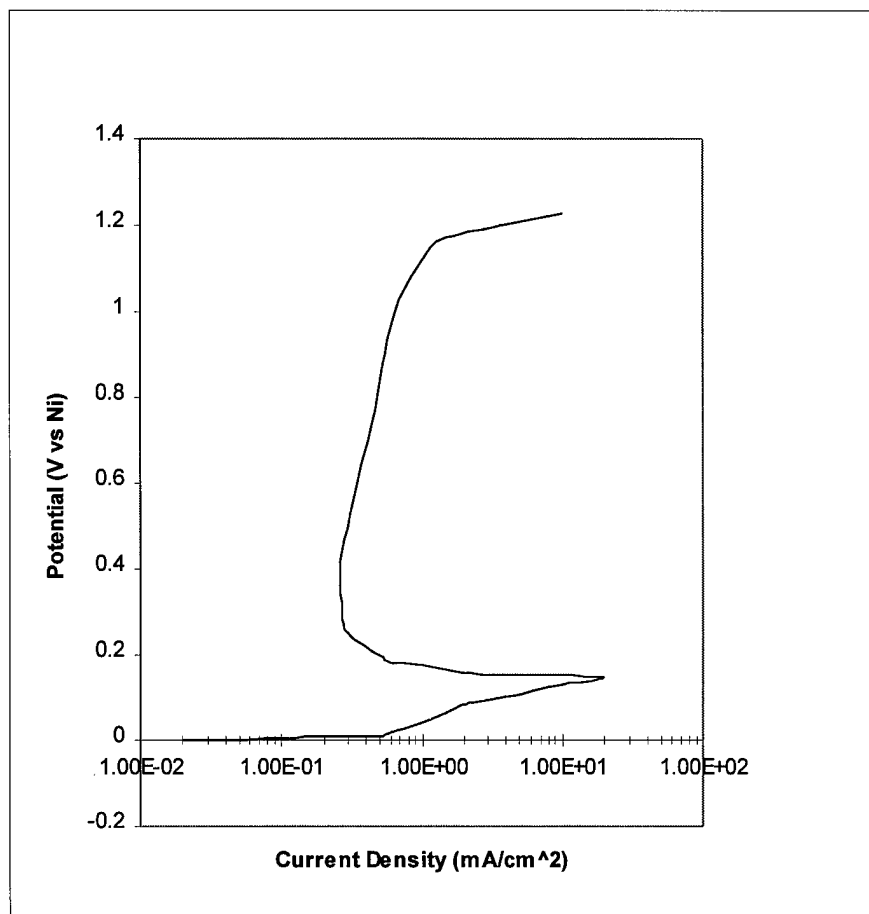


Figure 4-4: Polarization Curve for Alloy 600 at 300C in 10% NaOH<sup>4</sup>

During phase one, the potential drop for the test area was monitored versus the reference area. The test was terminated

---

<sup>4</sup> R. Scarberry, "Corrosion of Nickel Based Alloys", Conference Proceedings, American Society of Metals, Metals Park, 1985.

when a 50% rise in test area potential drop was indicated with no associated increase in the reference area potential drop.

#### 4.2 Crack Initiation and Growth Measurements

Following successful completion of the ACPD proof of principle testing, phase two tests were conducted to obtain crack growth data from the steam generator tube samples. The ACPD system was used to detect crack initiation and monitor growth rate. Stress intensity calculations were made based on a finite element analysis of the crack geometry. The data obtained was then compared to data obtained from other researchers using non-tube samples.

Crack initiation times were reduced by inducing axial fatigue cracks in the tube test area prior to inserting into the autoclave. Axial fatigue cracks were initiated at the test site by applying a circumferential load along one axial point using an MTS fatigue frame. The initiation site occurs at 90 degrees to the load axis by machining a pre-crack with a small grinding tool. This increases the stress at this point beyond that experienced along the load axis. The site was monitored with a strobe and fatigue crack length measured. The fatigue growth was stopped when cracks were visible on each side of the pre-flaw. Measurements on several tubes showed that this produced an approximate elliptical crack front. The stress intensity factor can be calculated using a finite element analysis of Newman and Raju<sup>5</sup> knowing the surface length of the

---

<sup>5</sup> J. C. Newman Jr., and I. S. Raju, "An Empirical Stress Intensity Factor Equation for the Surface Crack," *Engineering Fracture Mechanics*, Vol. 15, No. 1-2 (Great Britain: 1981), pp. 185-192.

fatigue crack. Final stress intensity was less than  $25 \text{ MPa}\sqrt{\text{m}}$ . The fatigue pre-cracks were initiated on the sample tubes prior to welding the caps.

Preparation of the sample, installation and operation of the system were identical to phase one. Pickup probes were carefully welded to each side of the pre-crack. The sample was plated ensuring adequate masking of the pre-crack area to avoid plating into the pre-crack. The caustic solution was identical to phase one and the sample was again polarized to +150 to 220 mV versus nickel.

At the conclusion of the test, the tube sample was removed and the axial ring encompassing the test area cut from the tube. The ring was fractured ductilely in tension using the MTS Test System to expose the IGSCC growth area. Measurement of the fatigue, IGSCC and ductile areas allowed calculation of the stress intensities for the applied stress. Growth rates were measured from the ACPD data.

## 5. Results

### 5.1 ACPD Proof of Principle Testing

The goal of this phase of testing was to prove the operability of the ACPD detection system to detect IGSCC initiation and growth under in-situ steam generator secondary conditions.

The initial data showed the potential drop beginning to rise within the first 10 hours of the start of the test (Figure 5-1). A steady increase in the potential drop continued for 68 hours at which time a sharp increase in the signal occurred. The sample wall stress was reduced by decreasing the internal sample pressure to check the validity of the potential drop signal (Figure 5-2). A drop in the potential indicated the possibility that crack initiation had occurred. The sample remained in the depressurized condition for approximately 12 hours. Repressurization of the sample demonstrated a return to the potential drop level previously recorded. The test was terminated at 140 hours when no further crack growth was noted.

A close visual examination under the stereoscopic microscope revealed no cracking of the wall in the test area of the sample. However, circumferential cracking of one of the test area pickup probes was noted. The crack appeared to be 50% through the 0.5 mm diameter wire. Normalizing the potential drop data clearly showed a rise in the test area signal with respect to the reference area (Figure 5-3).

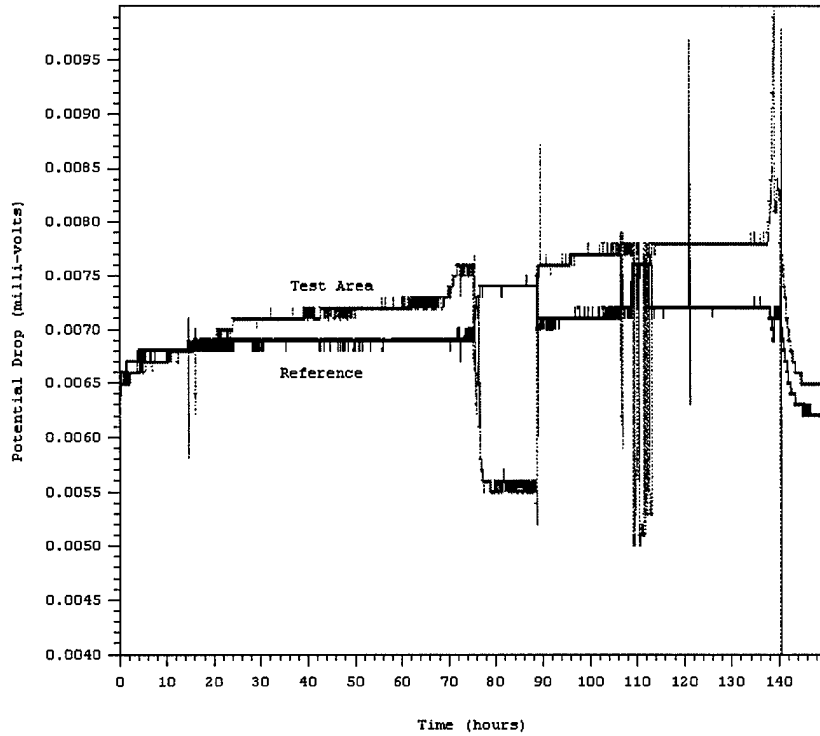


Figure 5-1: Potential Drop for the Test and Reference Areas.

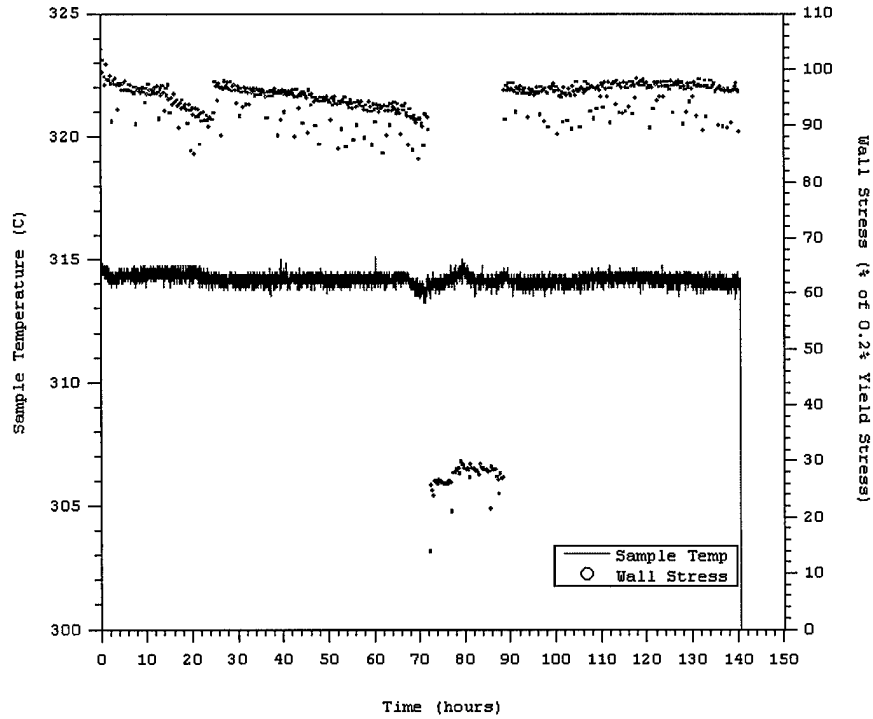
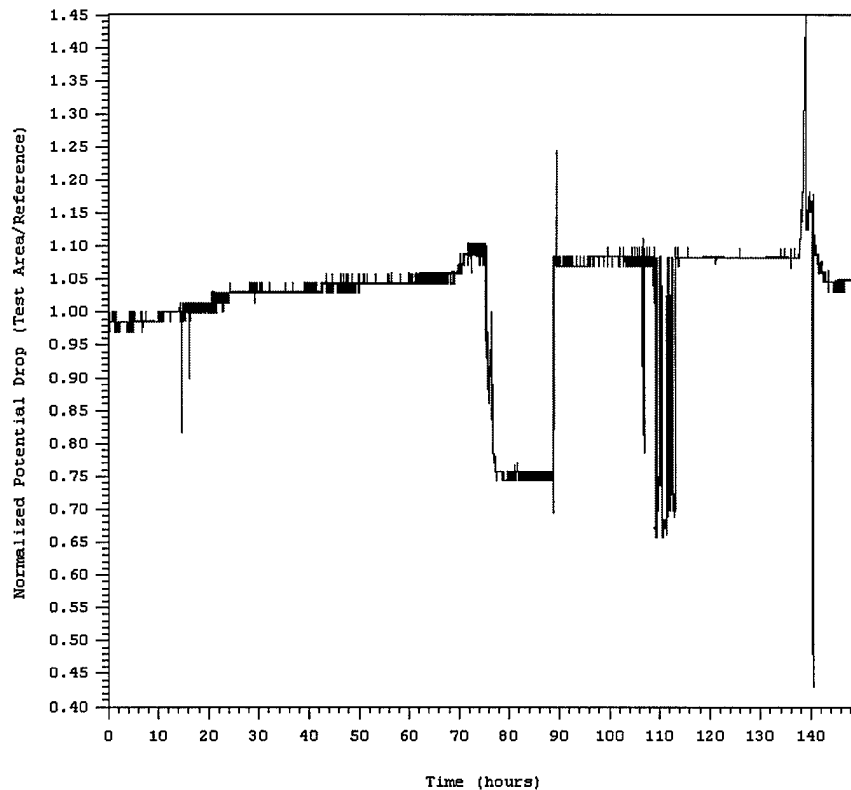


Figure 5-2: Sample Temperature and Wall Stress (Percent of 0.2% Yield Stress).





**Figure 5-3: Test Area Potential Drop Normalized With Respect To the Reference Area for Figure 5-2.**

Although the cracking did not occur in the sample, the test did show the ability of the ACPD system to detect crack initiation and growth in the caustic environment at temperature.

Additional data to confirm ACPD operation under in-situ steam generator conditions is presented in Figures 5-4 through 5-6. For this sample, the initial wall stress was set to 90% of yield stress. The sample was polarized to  $+225 \pm 5$  mV versus nickel based on previous studies by Bandy, et.al.<sup>1</sup>. Subsequent increases in wall stress in an attempt to expedite crack initiation occurred at the 400, 510, 600 and 740 hour points

---

<sup>1</sup> R. Bandy, R. Roberge and D. van Rooyen, "Intergranular Failures in Alloy 600 in High Temperature Caustic Environments," *Corrosion-NACE*, Vol. 41, No. 3, (March 1985), pp. 144-145.

(Figure 5-4). Incremental increases were used to ensure pressurization system integrity and to attempt to find the lowest optimum stress for crack initiation.

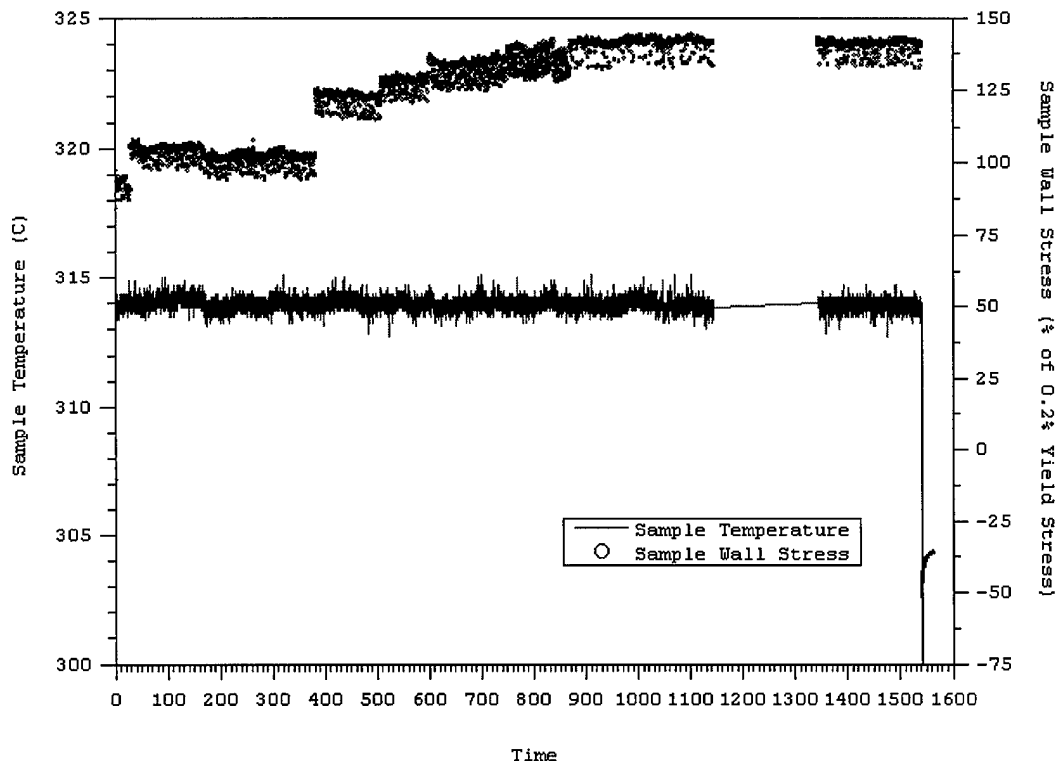


Figure 5-4: Sample Temperature and Wall Stress (Percent of 0.2% Yield Stress).

Two frequencies, 1 kHz and 10 kHz, were used at 800 mA and monitored by the ACPD system. The use of dual frequencies in these ranges allowed a relatively low frequency signal (which can be considered direct current (DC) from a skin effect viewpoint) and an alternating current (AC) signal, with some minor skin effect and minimal induction effects, to be used for detection and comparison.

Figure 5-5 plots the results of the potential drop measurements. Although no significant increase in the test area potential drop occurred, the reference area displays a

significant increase in both the 1 and 10 kHz signals. A sharp rise in the 1 kHz signal is easily seen at the 1400 hour point in the test. The potential drop measurements were normalized for the reference signal with respect to the test area signal (Figure 5-6). The steady rise in the 10 kHz signal from hour 520 until test termination is clearly seen.

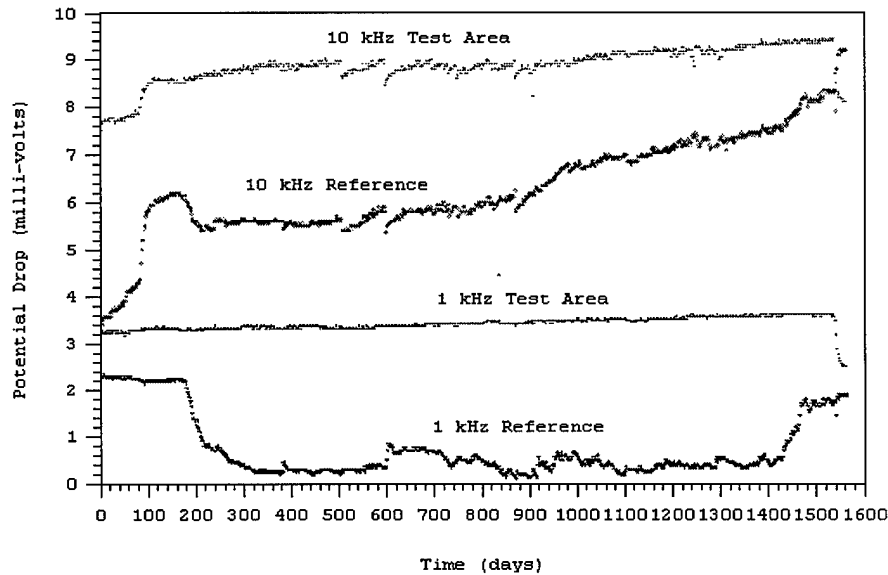


Figure 5-5: Potential Drop for Test and Reference Areas.

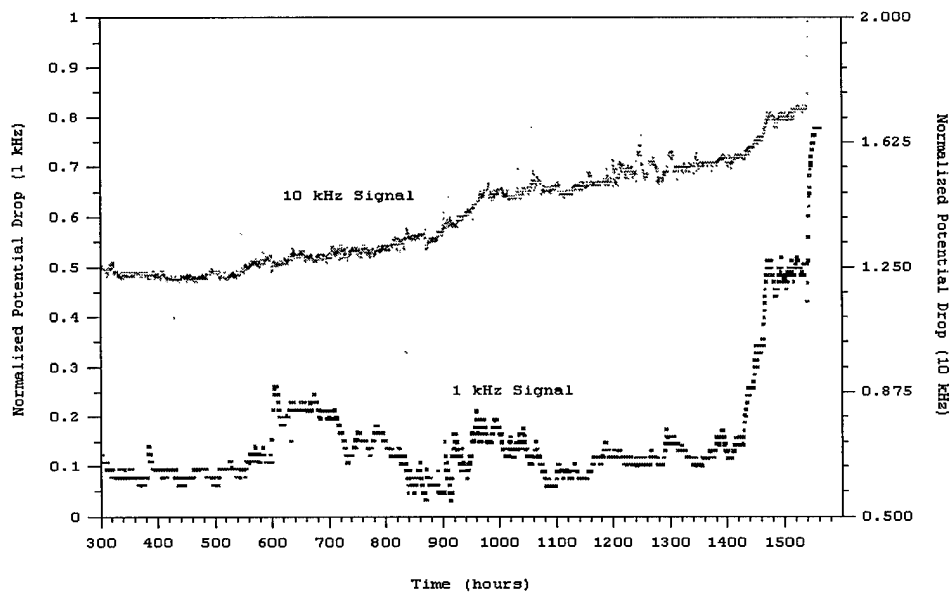


Figure 5-6: Normalized Potential Drop for Figure 5-5.

After operation for 1540 hours, the sample was depressurized and the autoclave cooled for sample inspection. Close visual examination under the stereoscopic microscope showed an approximately 2 mm long crack emanating from beneath the right reference area pick-up probe (Figure 5-7). Several smaller surface cracks were also noted. The tube was sectioned and the crack surface opened under tension. The area of intergranular stress corrosion cracking is well defined under SEM examination (Figures 5-8 and 5-9).



Figure 5-7: Stereoscopic Composite of Sample Surface Showing Crack Emanating From Beneath the Reference Area Probe.

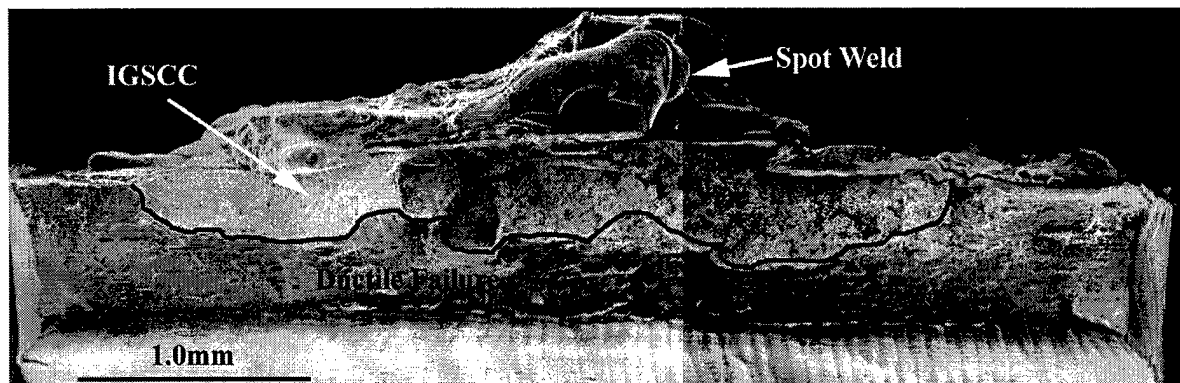


Figure 5-8: SEM Composite Micrograph of the Reference Area Fracture Surface.

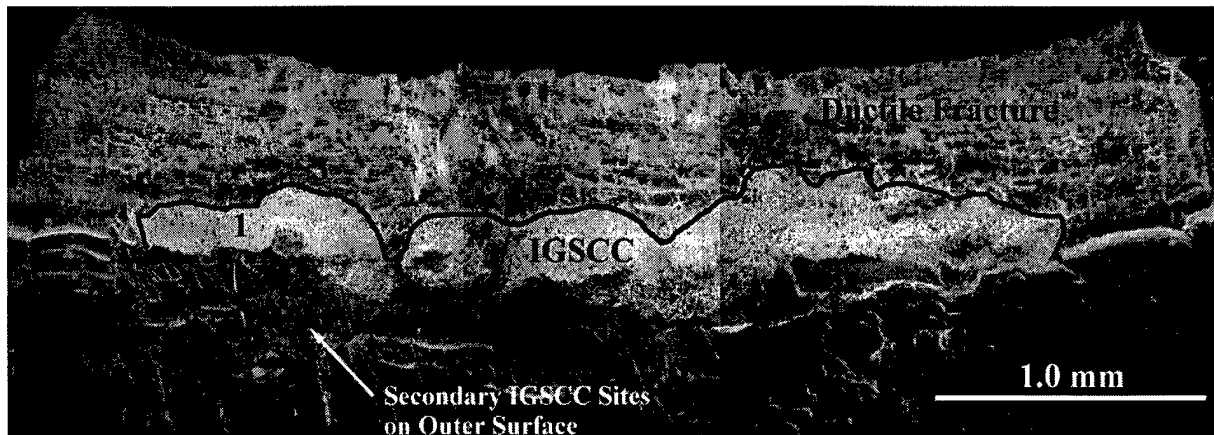


Figure 5-9: SEM Composite Micrograph of the Opposite Side of the Reference Area Fracture Surface. Note the Secondary IGSCC Cracks Apparent on the Surface Near the Primary Site.

Figures 5-10 and 5-11 are magnified micrographs of the areas indicated in Figure 5-8. The dimple effect of the ductile failure region in contrast to the easily distinguished grains and lack of deformation in the indicated IGSCC region are clearly seen. The area of interest is clearly the result of IGSCC, not ductile fracture. The boundary area micrograph in Figure 5-12 illustrates the transition region.

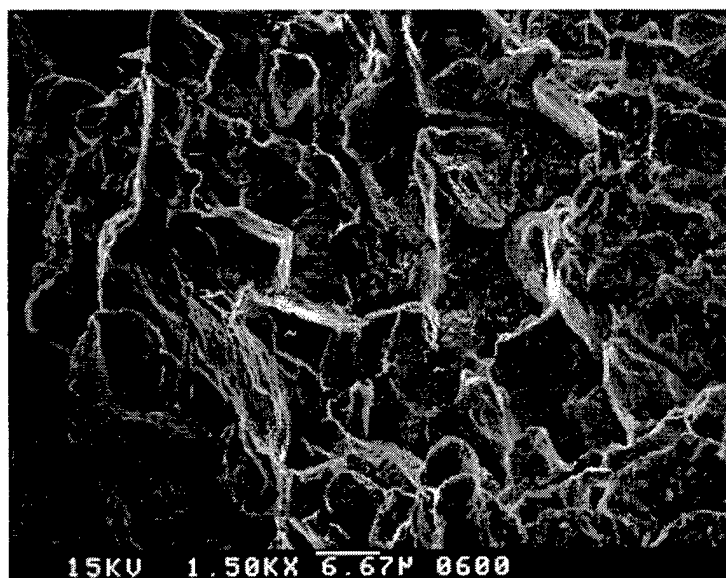


Figure 5-10: SEM Micrograph of Region 1 Clearly Showing IGSCC In This Region.

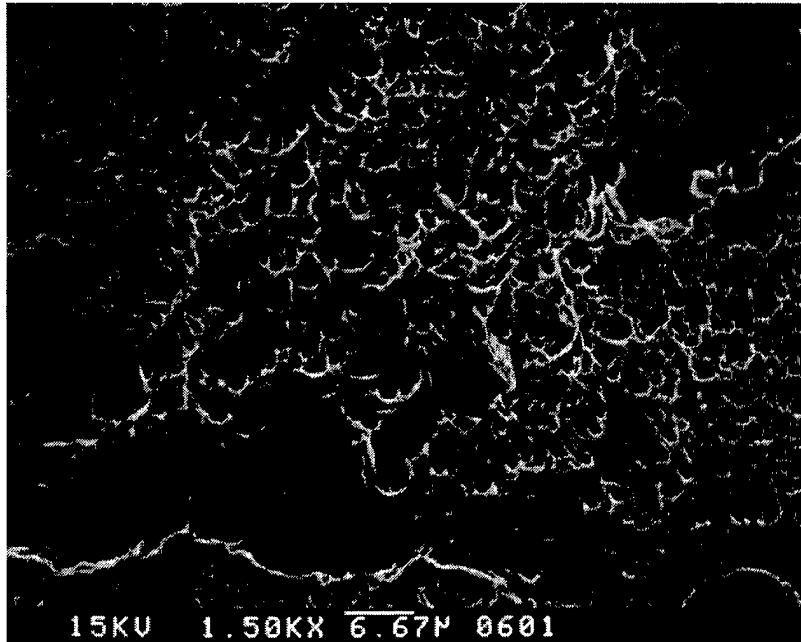


Figure 5-11: SEM Micrograph of Area 2 Showing Ductile Failure Region.

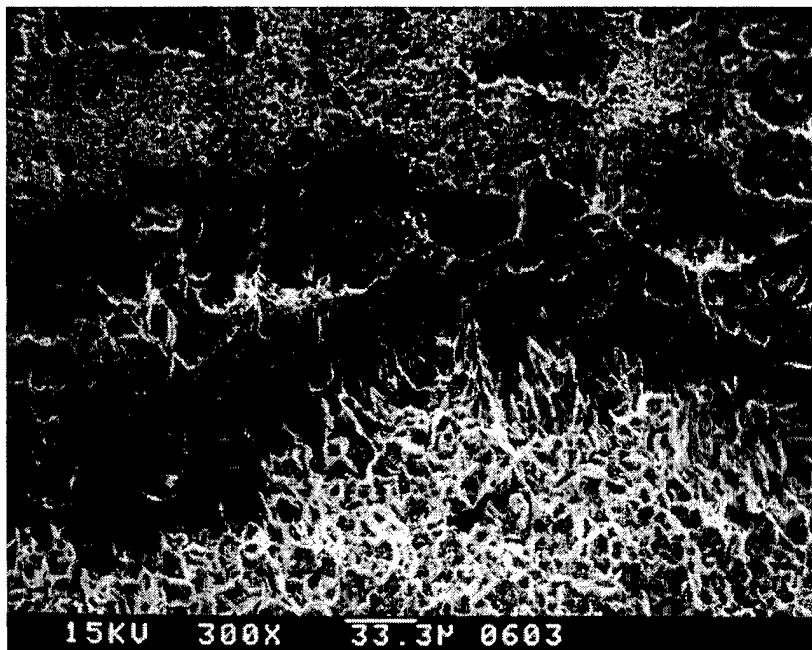


Figure 5-12: Ductile-IGSCC Transition Region.

The results of the potential drop measurements and subsequent confirmation of IGSCC demonstrate the successful application of the test system and the ability of the ACPD to detect cracks under in-situ steam generator conditions.

## 5.2 Crack Initiation and Growth Measurements

With the successful completion of the phase one testing, the test system was used to obtain crack growth data. Initial data was provided from a sample used in phase one. With the correlation of the potential drop with the IGSCC growth established, the micrographs and data taken from the ACPD were used to obtain stress intensity and crack growth measurements.

Figure 5-13 is the composite micrograph of the fracture surface of the sample. The white arcs outline the five individual crack fronts. In each case, the fronts are approximately elliptical in shape. Measurements of the crack front depth and length were performed. Based on the empirical relationships developed by J.C. Newman Jr. and I.S. Raju<sup>2</sup> for this geometry, the stress intensity factors were calculated. Crack growth rates were calculated based on the initial rise in the 10 kHz ACPD signal for the reference area.

Figure 5-14 illustrates graphically the approximate location of the crack initiation at 540 hours. Results of the crack stress intensity and growth rate calculations are tabulated in Table 5-1 for the five crack growth fronts.

---

<sup>2</sup> J.C. Newman Jr. and I.S. Raju, "An Empirical Stress Intensity Factor Equation for the Surface Crack," *Engineering Fracture Mechanics*, Vol.15, No.1-2 (Great Britain:1981), pp. 185-192.

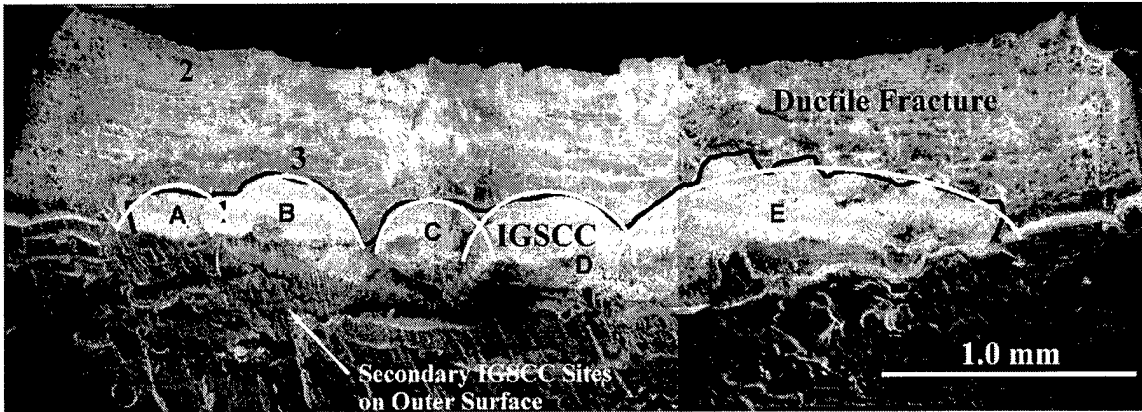


Figure 5-13: SEM Composite Micrograph of IGSCC Fracture Surface Showing Elliptical Crack Fronts.

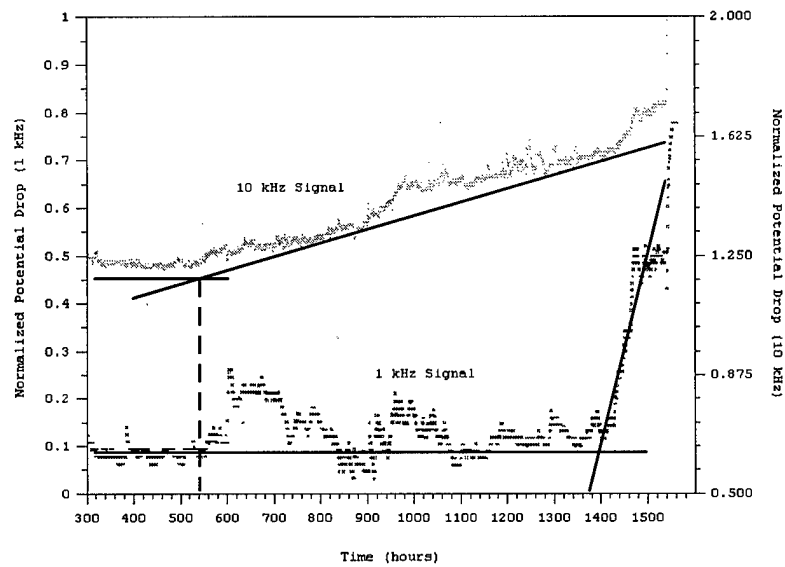


Figure 5-14: Normalized ACPD for Sample Showing Crack Initiation Time Based on Increasing 10kHz Potential Drop.

Area	Depth (b) ( $\mu$ )	Length (2a) (mm)	$K_I$ ( $\text{MPa}\sqrt{\text{m}}$ )	$dA/dt$ (mm/yr)
A	192	0.35	7.3	1.6
B	233	0.52	9.2	2.0
C	242	0.45	8.3	2.1
D	267	0.52	9.1	2.3
E	317	1.44	15.3	2.7

Table 5-1: Tabulated Results for Stress Intensity and Growth Rates.



Additional crack growth data was obtained for phase two. To expedite the crack initiation process, a sample with a well defined axial crack initiated by fatigue (as described in Section 4) was used for sample 960212. The machined notch was elliptical with an estimated depth of 0.5 mm from dial indicator readings and measurements conducted from the crack geometry (Figure 5-15). The fatigue crack growth front was expected to be elliptical, demonstrated in prior testing. Based on this geometry, the fatigue crack depth was calculated to be 1 mm or 72% of the wall.

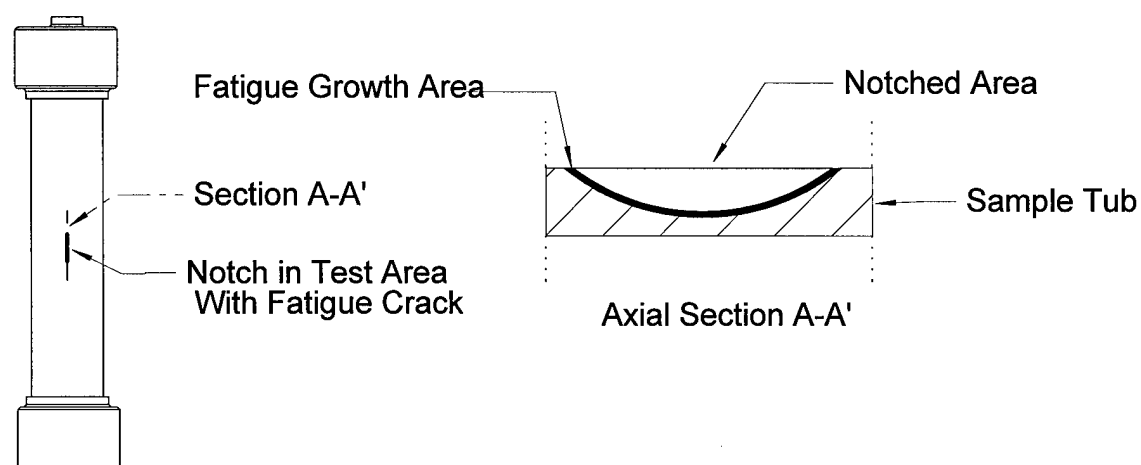


Figure 5-15: Schematic of Tube Samples With Fatigue Pre-Cracks in Test Area.

Procedures for system operation outlined in Section 4 were followed. The tube sample was polarized to +150 mV versus nickel based on the maximum corrosion rates observed by J. Lumsden, S.L. Jeanjaquet, J.P.N. Paine and A.R. McIlree<sup>3</sup>. Initial wall stress (38%) was chosen to yield an initial stress

---

<sup>3</sup> J. Lumsden, S.L. Jeanjaquet, J.P.N. Paine and A.R. McIlree, "Mechanism and Effectiveness of Inhibitors for SCC in a Caustic Environment," *Seventh International Symposium on Environmental Degradation of Materials in Nuclear Power Systems-Water Reactors*, Vol.1 (Breckenridge, CO: NACE International, August 7-10, 1995), pp. 317-323.

intensity factor at the crack front of  $11 \text{ MPa}\sqrt{\text{m}}$  ( $10 \text{ ksi}\sqrt{\text{in}}$ ). This value was chosen based on IGSCC crack growth rates observed in ASTM samples by M. Miglin<sup>4</sup>. The intent was to prevent fast crack growth and penetration of the tube wall. This in turn would allow observation of the crack growth by the ACPD system as demonstrated during the first phase of testing. Applied wall stress and sample temperature as a function of time are shown in Figure 5-16.

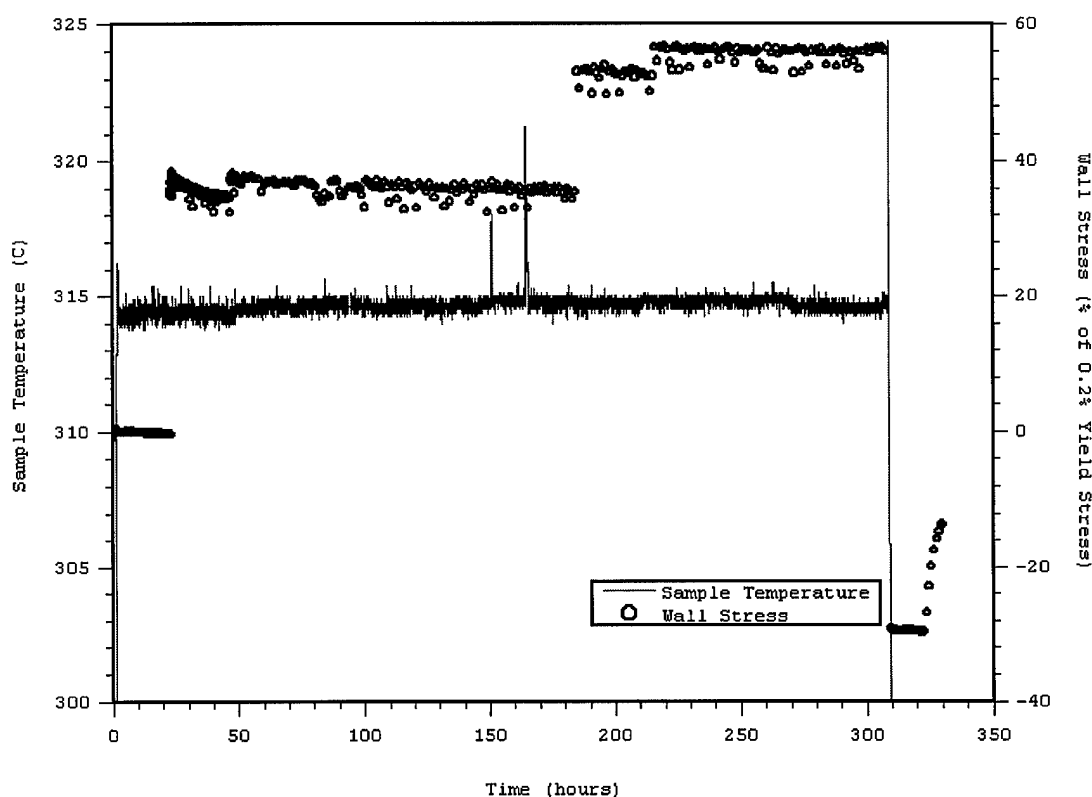


Figure 5-16: Sample Temperature and Applied Wall Stress (Percent of 0.2% Yield Stress).

<sup>4</sup> M. Miglin, J.V. Monter, C.S. Wade, M.J. Psaila-Dombrowski, A.R. McIlree, "SCC of Alloy 600 in Complex Caustic Environments," *Seventh International Symposium on Environmental Degradation of Materials in Nuclear Power Systems-Water Reactors*, Vol.1 (Breckenridge, CO: NACE International, August 7-10, 1995), pp. 277-290.

The potential drop measurements versus time are shown in Figure 5-17. An upward movement of the test sample caused the repositioning of the pickup wires and the large increase in potential at 140 hours into the test. At 185 hours into the test, with no large increases in the potential drop indicating crack growth, the wall stress was increased to 58%, or a K value of  $16.4 \text{ MPa}\sqrt{\text{m}}$  ( $15 \text{ ksi}\sqrt{\text{in}}$ ) based on initial crack geometry. The test terminated at 310 hours when a system shutdown occurred due to a loss of internal sample pressure. Subsequent examination of the test sample indicated that a through wall crack had occurred at the pre-notched test site (Figures 5-18 and 5-19).

Analysis of the normalized plot of the potential drop test area versus reference shows an overall increase in both the 10 kHz and 1 kHz potential drop signals from the initiation of testing (Figure 5-20). Based on this, the duration of crack growth was 310 hours with IGSCC initiation occurring from the onset of the test.

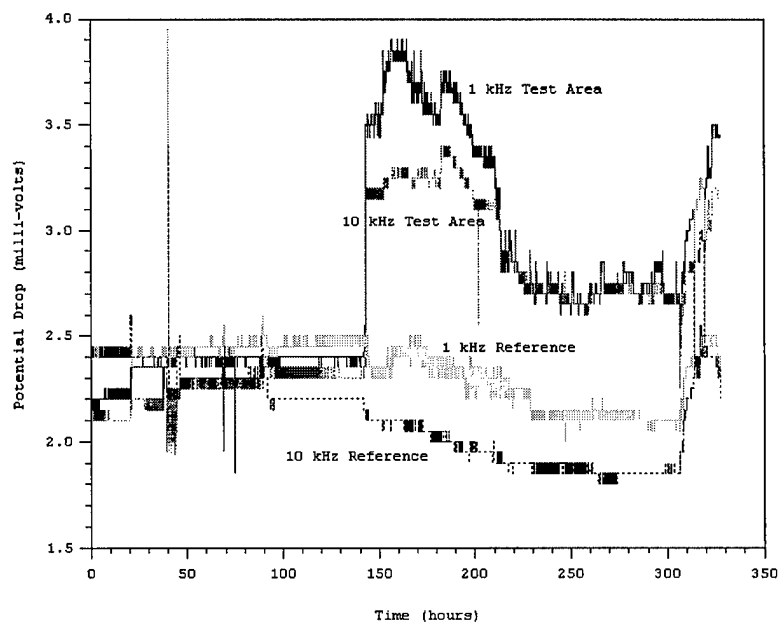


Figure 5-17: Potential Drop Versus Time for Test and Reference Areas.

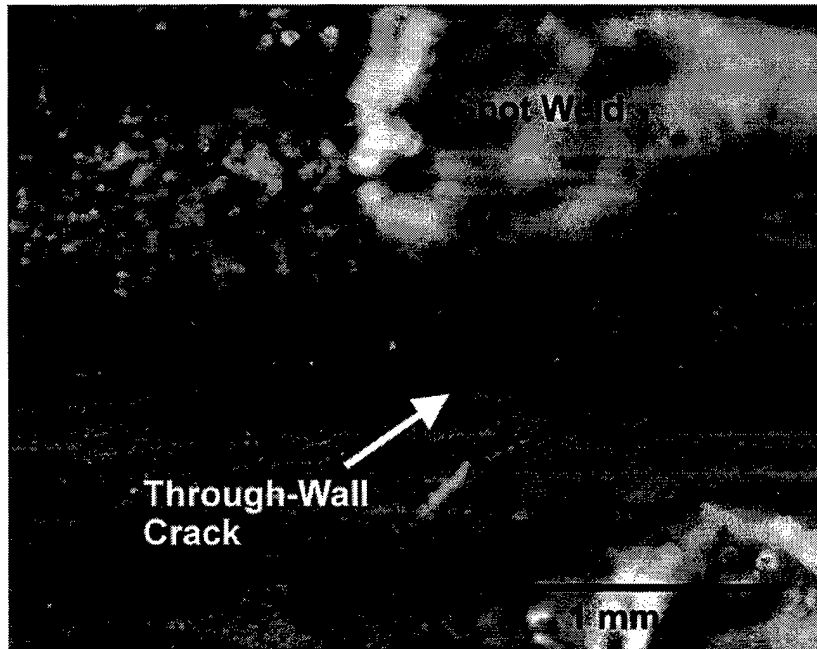


Figure 5-18: Stereo Microscope Image of the Through-Wall Crack Seen at the Base of the Machined Notch.

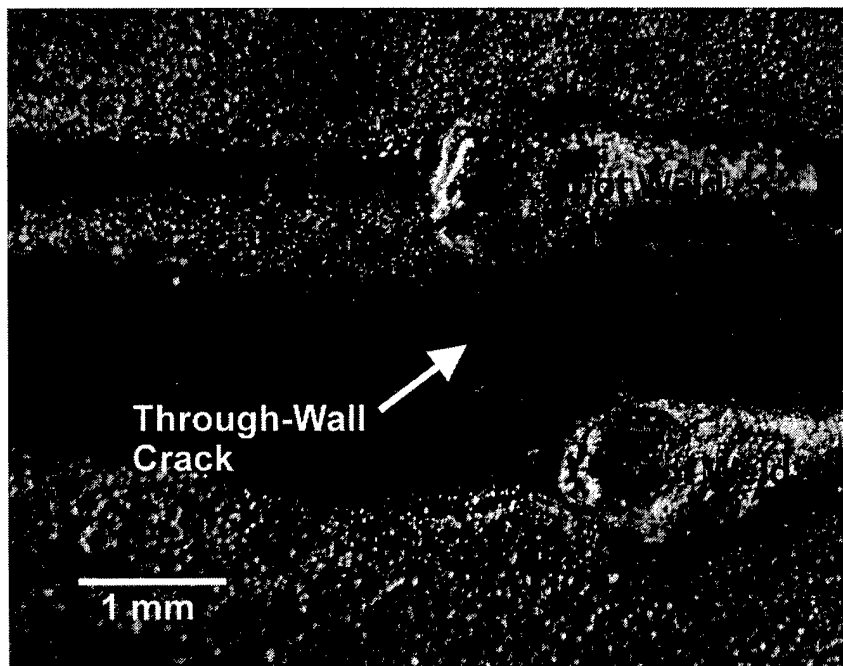


Figure 5-19: Low Power Stereo Microscope Image Showing the Relative Position of the Through Wall Crack to the Probes.

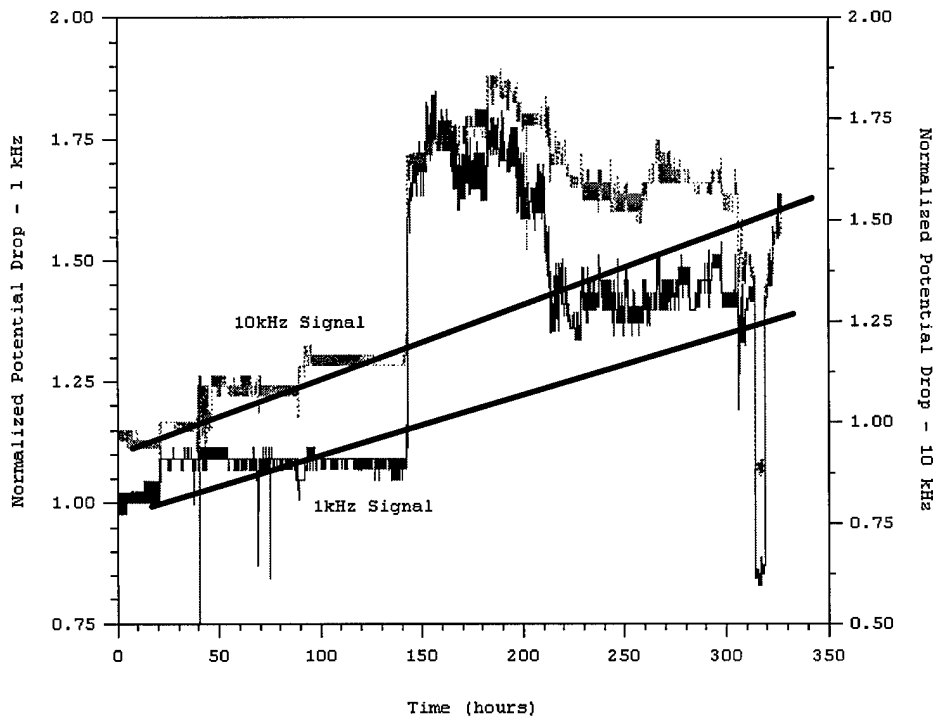
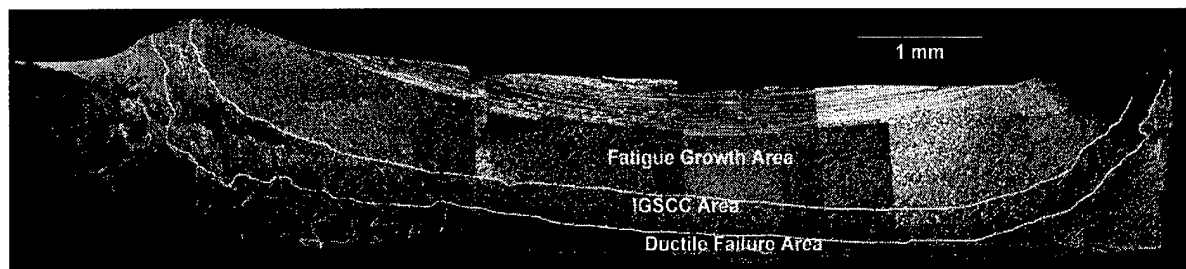


Figure 5-20: Normalized Potential Drop (Test Area with respect to the Reference Area) Showing an Increasing Signal from the Onset of Testing.

The sample tube was sectioned and the crack ductilely fractured. A visual examination was conducted by SEM. Figure 5-21 clearly shows a region of IGSCC. Several regions of through-wall crack propagation can also be seen. Figure 5-22 is a magnified micrograph of the IGSCC area showing two distinct growth areas for the two different applied stress intensities. A beach mark separates the two varying areas of IGSCC growth and is outlined in white. Micrographs of the ductile region, caused by the process used to open the crack area, and the pre-fatigue regions are presented in Figures 5-23 and 5-24 for comparison. The transition region between the fatigue area and the IGSCC area is shown in Figure 5-25.



Area Shown in  
Figure 5-22

Figure 5-21: SEM Composite Micrograph of Fracture Surface Clearly Showing Area of IGSCC.

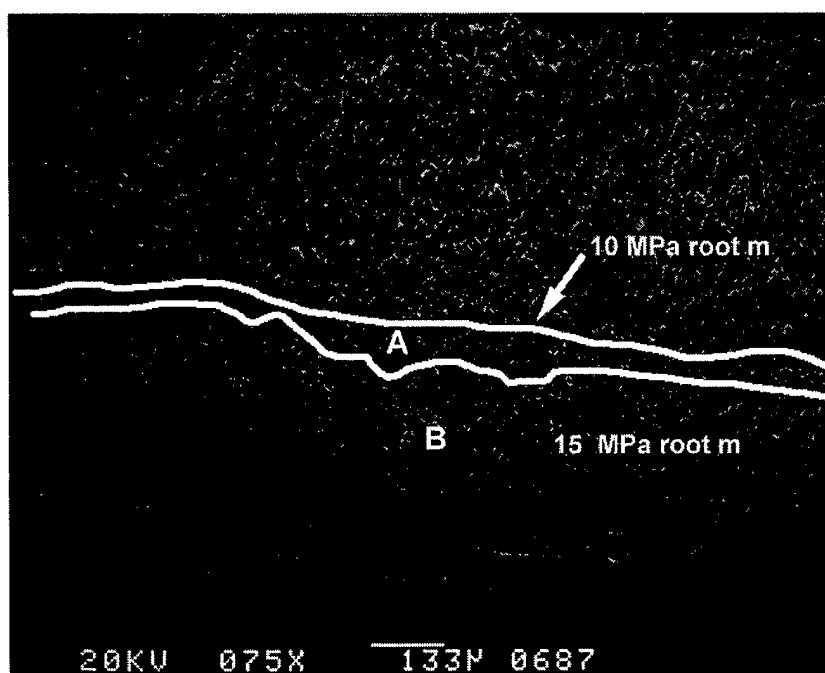


Figure 5-22: Magnified SEM Micrograph of IGSCC Area Outlining Two Possible Crack Growth Areas.

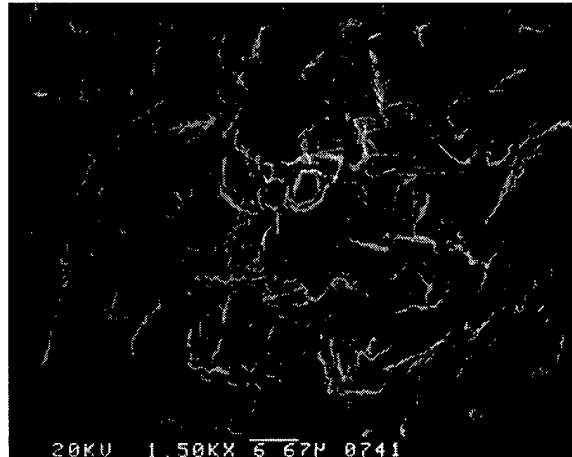


Figure 5-23: Micrograph of the Pre-Fatigue Area.

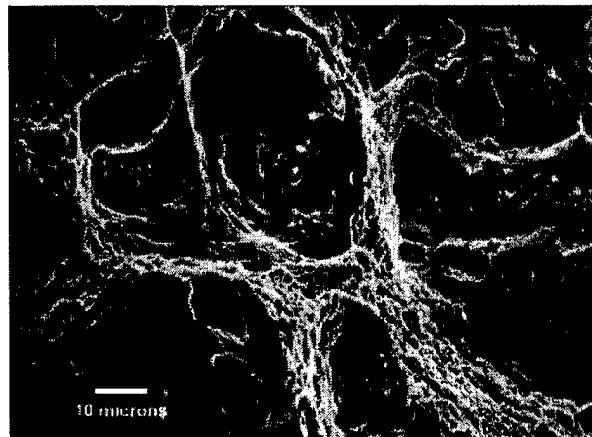


Figure 5-24: Micrograph of the Ductile Failure Region.

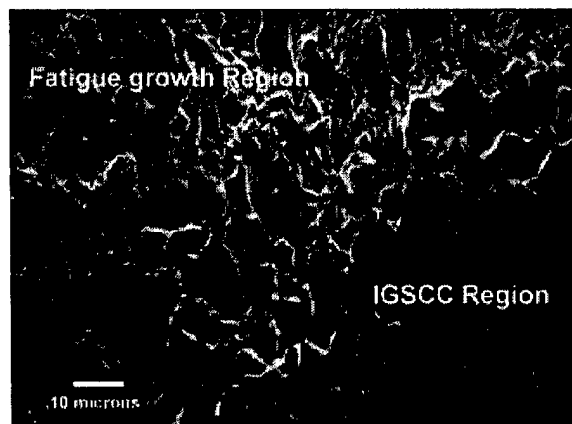


Figure 5-25: Micrograph Showing the Pre-Fatigue to IGSCC Transition Region.

Table 5-2 summarizes the results of crack depth measurements for the two crack growth regions indicated by Figure 5-21. Crack growth time is based on initiation of IGSCC at the onset of testing from the ACPD data. Based on the visual measurements of the fracture surface, the initial stress intensity ( $K_I$ ) of 11.9 MPa $\sqrt{m}$  (10.9 ksi $\sqrt{in}$ ) compares favorably with the estimated value during the test. The area of IGSCC measures 67 $\mu m$  and 203 $\mu m$ , respectively, in depth from the surface for the two growth areas. Finite element analysis yields an average  $K_I$  of 12.3 MPa $\sqrt{m}$  and 17.7 MPa $\sqrt{m}$ , respectively, for the two growth areas.

Area	Depth (b) ( $\mu m$ )	Length (2a) (mm)	$K_I$ MPa $\sqrt{m}$	dA/dt (mm/yr)
<b>Fatigue</b>	1114	9.0	11.9	na
<b>A</b>	1181	9.5	12.6	3.6
<b>B</b>	1384	11.2	22.8	14.2

Table 5-2: Tabulated Results for Stress Intensity and Growth Rates.



## 6. Discussion

### 6.1 ACPD Proof of Principle

The goal of phase one, to prove that the ACPD system could be used to detect cracks on tubing under in-situ steam generator conditions, was validated. The data clearly indicate a correlation between potential drop and crack initiation and growth. This was illustrated in the normalized plots of Figures 5-3 and 5-6. To substantiate this claim, predicted values for the potential drop can be calculated and compared to the actual values obtained. The assumption that the 10 kHz and 1 kHz signals are close to DC signals will be made for simplicity. This assumption is valid since the non-ferromagnetic properties of alloy 600 provide little increase in current density near the surface.

For one sample, the predominant effect was an area change since the current path length to the crack was several orders of magnitude greater than the change of length due to the crack. The normalized calculated potential drop versus actual results is plotted in Figure 6-1.

In a second sample, the IGSCC crack occurred under the reference probe vice test area. This was probably due to higher residual stresses in this area due to the weld (a small heat affected zone) or incomplete plating that allowed a crevice. The difference between the calculated potential drop from the area change in the sample and the increase in the path due to crack penetration is an order of magnitude. Therefore, the potential drop was most affected by the change in the path length. This is a valid assumption for an AC signal, deviating from the initial assumption of pure DC. Using the depth of penetration shown in

Table 5-1 and assuming a constant linear crack growth, the normalized calculated potential drop versus actual test results are plotted in Figure 6-2.

The correlation between the actual and calculated potential drops is excellent. Differences between the actual and calculated potential drops can be attributed to:

(1) current loss through the conductive solution,

(2) relative resistance differences between the wires and sample from those assumed, and

(3) inductive losses not included in the calculation since DC current was assumed for the estimate.

The 1 kHz signal in one set of data shows a much greater rise than the 10 kHz predictions but only near the end of the test cycle. However, if one assumes the crack started at the same point the 10 kHz signal began to rise, the overall increase in the 1 kHz signal is also very close to that calculated. The possibility of noise in the 1 kHz signal during the 520 to 1400 hour region could account for the failure of the potential drop to rise in this period. This postulate became more likely when it was discovered that a ground in the shield for the 1 kHz signal existed.

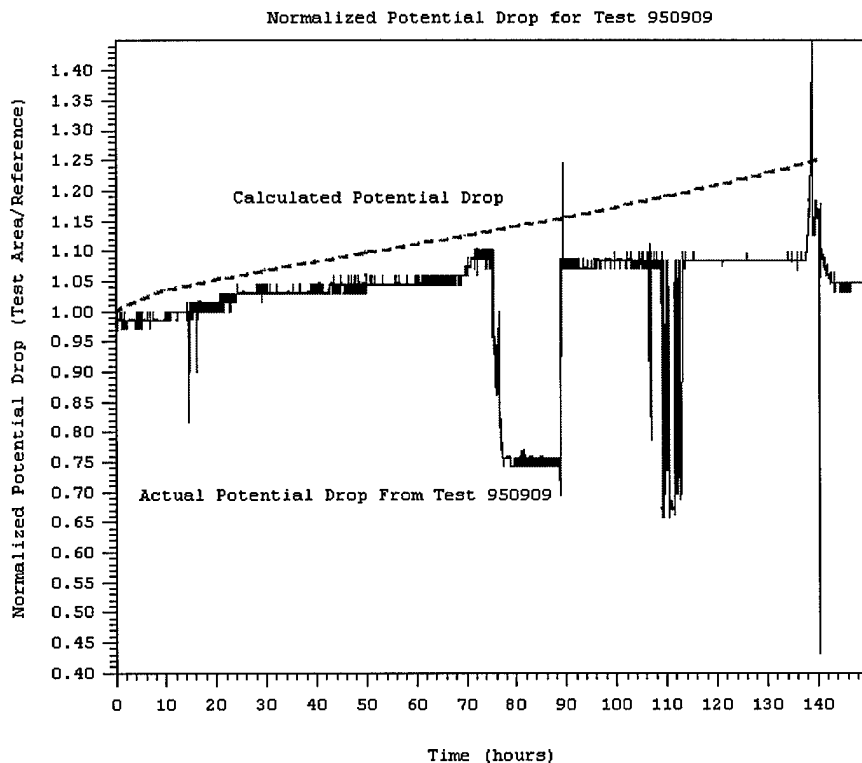


Figure 6-1: Calculated Potential Drop Versus Actual.

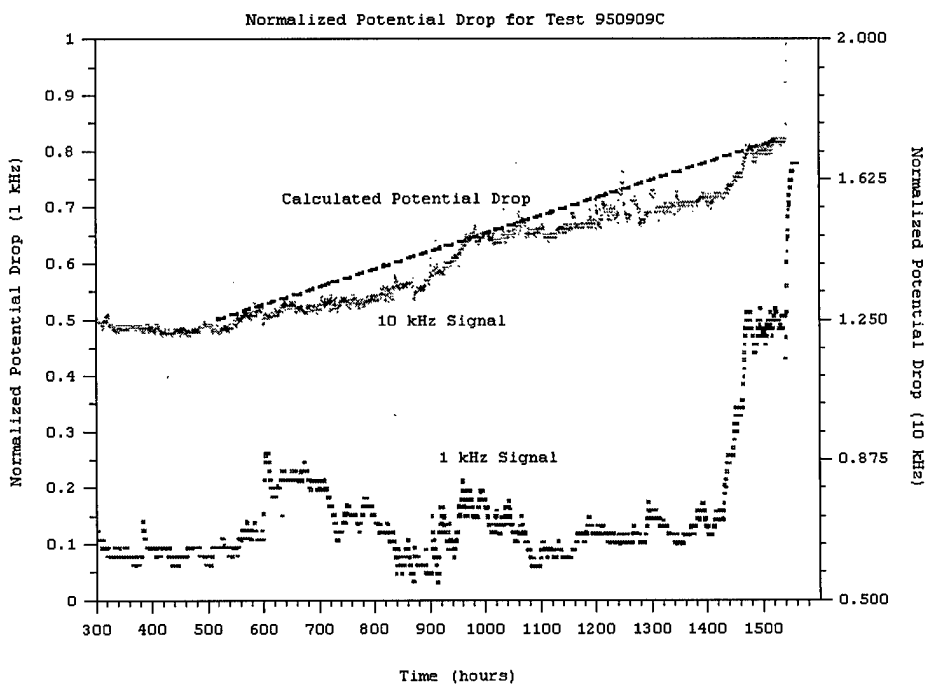


Figure 6-2: Calculated Potential Drop Versus Actual.

## 6.2 Crack Growth Rates

The measurements of crack length and depth given in Tables 5-1 and 5-2 were used to calculate stress intensity and growth rate based on test duration. The average values of stress intensity and calculated growth rates for the two sets of data for phase two are plotted in Figure 6-3.

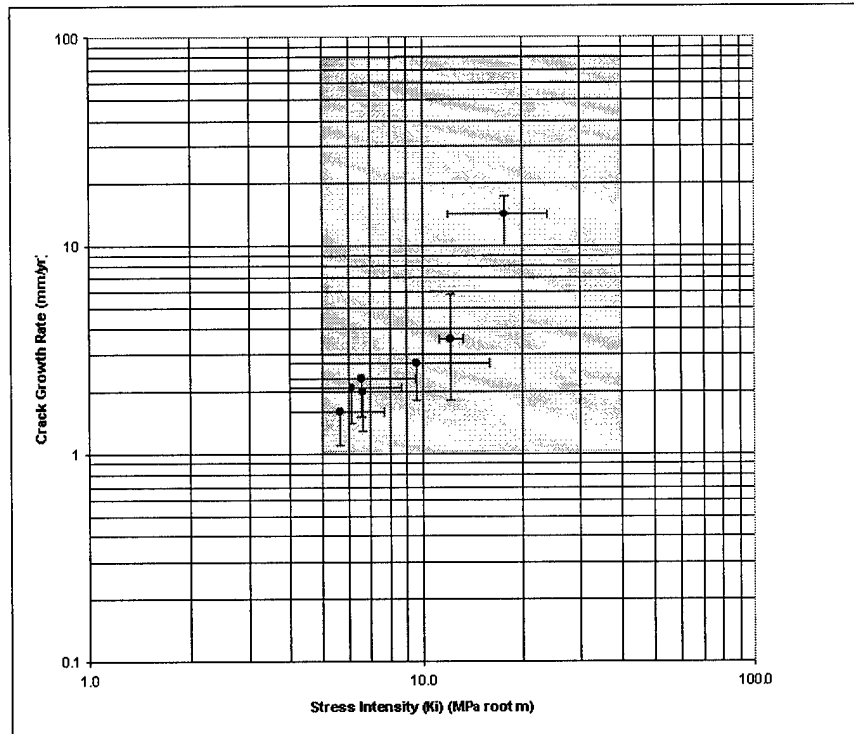


Figure 6-3: Alloy 600 Tube Crack Growth versus Stress Intensity from Phase Two Testing. The Shaded Area Represents Data Ranges for K and Growth Rates from M. Miglin<sup>1</sup>.

It is significant to note an apparent relationship in the stress intensity versus crack growth rates. Based on the tube data collected, growth rate appears to be exponential to the

<sup>1</sup> M. Miglin, J. V. Monter, C. S. Wade, M. J. Psaila-Dombrowski, A. R. McIlree, "SCC of Alloy 600 in Complex Caustic Environments," *Seventh International Symposium on Environmental Degradation of Materials in Nuclear Power Systems-Water Reactors*, Vol. 1 (Breckenridge, CO:NACE International, August 7-10, 1995), pp. 277-290.

applied stress intensity when  $K_I$  is less than about 15 MPa $\sqrt{m}$ . For values between 15 and 20 MPa $\sqrt{m}$ , crack growth rates accelerate, indicating a threshold value, approximately 15 MPa $\sqrt{m}$ , above which growth rates increase at an increasing rate.

Previously reported crack growth data in 10% NaOH was compared with the results from this study. M. Miglin, et.al., have reported stress intensity values from 5 to 40 MPa $\sqrt{m}$  with growth rates from 0.2 to 76 mm/yr<sup>2</sup>. The shaded area in Figure 6-3 represents this broad range of reported data from M. Miglin<sup>3</sup>. In addition, Rebak, et.al. have obtained crack growth data for Alloy 600 flat tubes at various pH and temperatures ranging from 300 to 330°C<sup>4</sup>. A good correlation is shown when comparing Rebak's data to the present tube data (Figure 6-4). The dark upper bands represent data primarily in pH range 9 to 10, while the lower, lighter band represents data primarily in the 5 to 9 pH range. The data indicate a crack growth rate dependence on pH as well as on  $K_I$ .

Figure 6-5 shows a plot of various growth rates versus pH from Miglin<sup>5</sup> and Rebak, et.al.<sup>6</sup>. The data from Rebak is broken down into stress intensity ranges and is consistent with the

---

<sup>2</sup> M. Miglin, J. V. Monter, C.S. Wade, M. J. Psaila-Dombrowski, A. R. McIlree, "SCC of Alloy 600 in Complex Caustic Environments," *Seventh International Symposium on Environmental Degradation of Materials in Nuclear Power Systems-Water Reactors*, Vol. 1 (Breckenridge, CO: NACE International, August 7-10, 1995), pp. 277-290.

<sup>3</sup> T. Beineke, et. al., "PWR Molar Ratio Control Applications Guidelines", EPRI TR.-104811-V1, 1995, p. 2-13.

<sup>4</sup> R.B. Rebak, and Z. Szlarska-Smialwska, "Influence of Stress Intensity and Loading Mode on Intergranular Stress Corrosion Cracking of Alloy 600 in Primary Water of Pressurized Water Reactors," *Corrosion*, Vol. 50, No. 5, (May 1994), pp. 378-393.

<sup>5</sup> M. Miglin, et.al., op. cit., p. 285.

<sup>6</sup> R.B. Rebak, and Z. Szlarska-Smialwska, "Influence of Stress Intensity and Loading Mode on Intergranular Stress Corrosion Cracking of Alloy 600 in Primary Water of Pressurized Water Reactors," *Corrosion*, Vol. 50, No. 5, (May 1994), pp. 386-387.

results illustrated in Figure 6-4 (Note the decrease in growth rate with pH for a specific stress intensity band). The crack growth data for prior testing is based on ASTM specimens, not tubes. Of significance is the wide variation in growth rates in pH range 10 (.025 to 250 mm/yr.). The alloy 600 tube data obtained in phase two fall in the middle of this range.

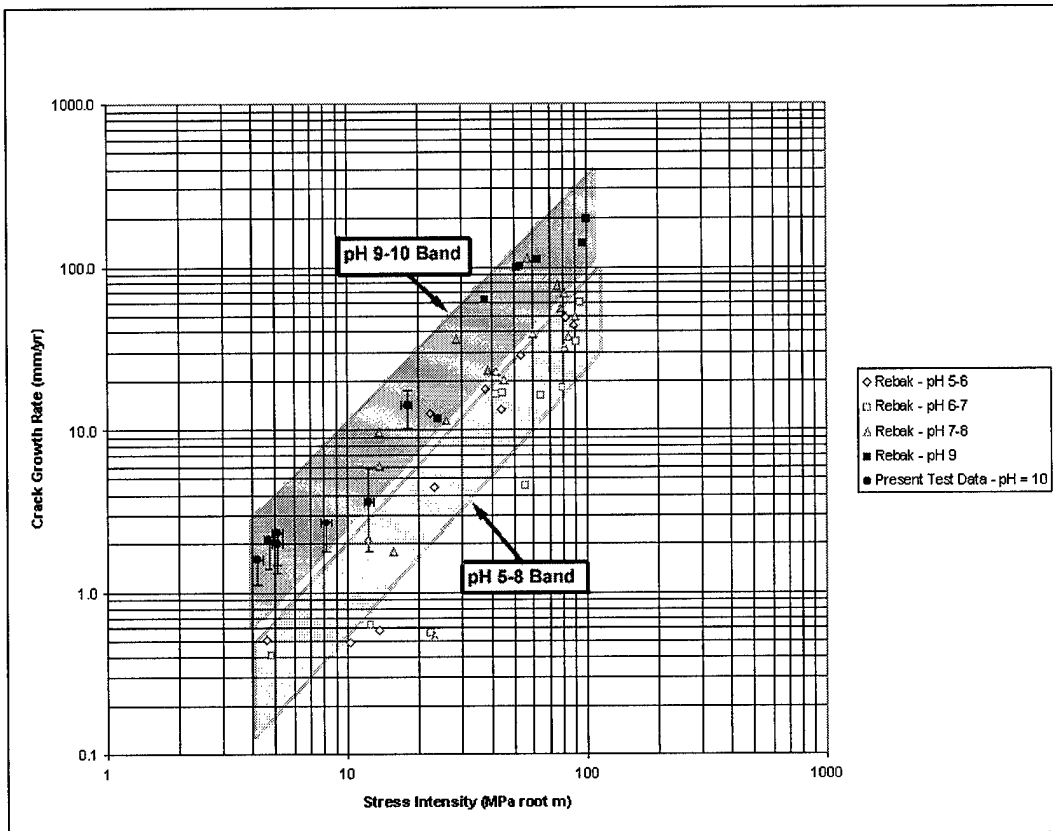


Figure 6-4: Comparison of Crack Growth Data versus Stress Intensity (K).

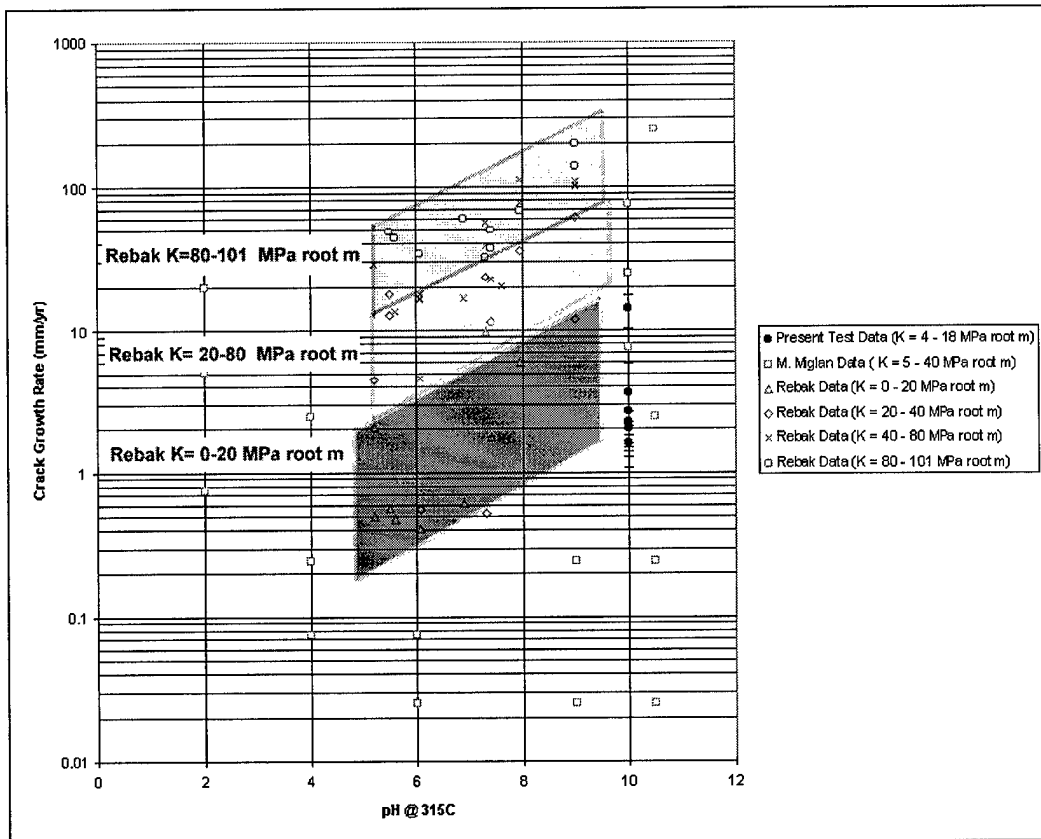


Figure 6-5: Comparison of Alloy 600 Crack Growth Rates versus pH.

No prior data exists for crack growth in actual steam generator tube samples. The tube data presented here represents the first in-situ monitoring and crack growth measurement of steam generator tubing. The tubing data obtained during phase two testing correlates with data reported for non-tube (i.e. plate samples) alloy 600 specimens, which implies credibility for the results from plate samples. Based on this data and the relationships obtained, steam generator tube crack growth rates from in-situ inspections can be predicted and further development of an on-line monitoring system using ACPD methods developed.

## 7. Conclusions

A laboratory system capable of monitoring alloy 600 steam generator tubing for IGSCC using an ACPD multi-frequency detection system was constructed. The system provided the capability to maintain an environment similar to an operating steam generator secondary side. Additionally, the autoclave system provided the capability to impress varying wall stresses on the tube samples up to 140 % of yield strength to expedite crack initiation.

The capability of the ACPD system to detect initiation and growth of IGSCC on alloy 600 tubes in the in-situ environment was demonstrated. IGSCC initiation and growth was monitored up to 1240 hours at two frequencies. The higher frequency proved to have a greater sensitivity to crack initiation. The measured potential drop from the tube data correlated well with calculated values.

IGSCC crack growth data for alloy 600 tubes was obtained. Average values of stress intensity ( $K_I$ ) ranged from 4.2 to 17.4 MPa $\sqrt{m}$  with growth rates from 1.6 to 12.3 mm/yr. Data obtained from these tests show an exponential relation between crack growth rate and stress intensity for alloy 600 tubes.

The crack growth data obtained from these tests were compared to data from previous researchers using standard test samples of alloy 600. The measured tube crack growth data and stress intensities compared favorably to prior data. The data obtained is the first IGSCC crack growth data in tubes. This data and future test data obtained using the procedures and techniques developed, may be used in predicting tube failure times based on site inspections.



## 8. Recommendations for Future Work

An early goal of the program was to make use of the ACPD monitoring system to measure the effectiveness of various inhibitor compounds to mitigate or halt SCC growth. Due to time constraints, this could not be accomplished in this program. However, inhibitors can play a critical role in the mitigation of IGSCC in existing steam generators. The system developed in this research can provide the data essential for an evaluation of inhibitors and this evaluation should be performed.

Additional stress intensity (K) versus growth rate data is needed to better establish the relationship between growth rate and K. This data will also establish a better band of expected growth rates for alloy 600 tubing.

Data from ACPD measurements of SCC growth in tubes is required to provide a predictive tool. Future data collection will enable the determination of crack size versus potential drop and allow operator prediction of crack size on-line.

Finally, higher frequency application of the ACPD input signal needs to be investigated to allow the probe spacing to increase with no loss in sensitivity. The use of the ACPD system under actual steam generator conditions will require less restrictive placement of the output probes. The data collected during testing conducted thus far indicates that higher frequency application may allow an increase in probe spacing with the same sensitivity to crack growth.

## References

- Adams, James P. and Eric S. Peterson. "Steam Generator Secondary pH During A Steam Generator Tube Rupture." *Nuclear Technology*, CII, (June 1993), pp. 304-306.
- Andersen, P.L.. "Effects of Temperature on Crack Growth Rate in Sensitized Type 304 Stainless Steel and Alloy 600." *Corrosion Science*. Vol.49, No.9 (September 1993).
- Babcock and Wilcox. *Steam/its generation and use*. 39th Ed. New York: Babcock and Wilcox, 1978.
- Ballinger, R.G. and I.S. Hwang. "Characterization of Microstructure and IGSCC of Alloy 600 Steam Generator Tubing." Final Report, EPRI TR-101983, Palo Alto: Electric Power Research Institute (February 1993), p. 3-56.
- Bandy, R., R. Roberge, and D. van Rooyen. "Intergranular Failures of Alloy 600 in High Temperature Caustic Environments." *Corrosion - NACE*", XVI no. III, (March 1985), pp. 142-151.
- Baumeister, T., E. Avallone, T. Baumeister III. *Mark's Standard Handbook for Mechanical Engineers*. 8th Ed. New York: McGraw-Hill Book Co. (1978).
- Beineke, T.. et.al.. "PWR Molar Ratio Control Applications Guidelines". EPRI TR-104811-V1, 1995.
- Berry, Warren E. *Corrosion in Nuclear Applications*. New York: John Wiley & Sons, 1971.
- Catlin, W. R., D.C. Lord, T.A. Prater and L.F. Coffin. *The Reversing DC Electrical Potential Method*. Schenectady, NY: General Electric.
- Cels, J.R.. Caustic Stress Corrosion Cracking Studies at 288C(550F) Using the Straining Electrode Technique. *Corrosion-NACE*, V34, No.6 (June 1978).
- Charlesworth, F.D.W. and W.D. Dover. "Some Aspects of Crack Detection and Sizing using A.C. Field Measurements." *The Measurement of Crack Length and Shape During Fracture and Fatigue*. Edited by C.J. Beevers. West Midlands, UK: EMAS (1982), p. 258.

- Electric Power Research Institute. "Boric Acid Application Guidelines for Intergranular Corrosion Inhibition," EPRI NP 5558. (1984).
- Electric Power Research Institute. *Steam generator Reference Handbook*. EPRI TR-103824, Project 2895;4044 Nuclear Power Group. Palo Alto: EPRI, Dec 1994.
- Friend, Wayne Z. *Corrosion of Nickel and Nickel Based Alloys*. New York: John Wiley & Sons, 1980.
- Hwang, I.S. and R.G. Ballinger. "A Multi-Frequency AC Potential Drop Technique for the Detection of Small Cracks." *Measurement Science Technology*, Vol 3, (1992), p 63.
- Hwang, I.S., "Embrittlement Mechanisms of Nickel-Base Alloys in Water." Ph.D. dissertation, Department of Nuclear Engineering, Massachusetts Institute of Technology, 1987.
- Inco Alloys International. *Inconel*. Huntington, WV: Inco Alloys International, Inc.
- International Nickel Co., Inc.. "Corrosion Resistance of Nickel and Nickel-Containing Alloys in Caustic Soda and other Alkalies." *Corrosion Engineering Bulletin*. CEB-2, 1971.
- Jang, I., "Effect of Sulphate and Chloride ions on the Crevice Chemistry and Stress Corrosion Cracking of Alloy 600 in High Temperature Aqueous Solutions." *Corrosion Science*, Vol. 33, No. 1 (1992), pp. 25-38.
- Johnk, Carl T.A. *Engineering Electromagnetic Fields and Waves*, New York: John Wiley and Sons, 1975.
- Johns, D.R. and F.R. Beckitt. "Factors Influencing the Thermal Stabilisation of Alloy 600 Tubing Against Intergranular Corrosion." *Corrosion Science*, XXX No. II/III (1990), pp. 223-237.
- Jordan, Edward C. *Electromagnetic Waves and Radiating Systems*. 2nd Ed. Englewood Cliffs, N.J.: Prentice-Hall, 1968.
- King, Ronold W. P. *Fundamental Electromagnetic Theory*. 2nd Ed. New York: Dover Publications, Inc, 1963.

- Lumsden, J. B., S.L. Jeanjaquet, J.P.N. Paine and A. McIlree. "Mechanism and Effectiveness of Inhibitors for SCC in a Caustic Environment." *Seventh International Symposium on Environmental Degradation of Materials in Nuclear Power Systems - Water Reactors*, Vol 1, Breckenridge, CO: NACE International (August 7-10,1995), pp. 317-325.
- Lumsden, J.B. and P.J. Stocker. "Inhibition of IGA in Nickel Based Alloys in Caustic Solutions." *Corrosion/88*, Houston, TX: National Association of Corrosion Engineers (1988).
- Miglin, M.T., J.V. Monter, C.S. Wade, M.J. Psaila-Dombrowski, and A.R. McIlree. "SCC of Alloy 600 in Complex Caustic Environments." *Seventh International Symposium on Environmental Degradation of Materials in Nuclear Power Systems - Water Reactors*, Vol 1, Breckenridge, CO: NACE International (August 7-10,1995), pp. 277-290.
- Morra, M.M., J.M. Morra and R.R. Biederman. "A Technique for the Preparation of Powders for Examination by Transmission Electron Microscopy." *Materials Science and Engineering*, A124 (1990) pp. 55-64.
- Newman Jr., J.C. and I.S. Raju, "An Empirical Stress Intensity Factor Equation for the Surface Crack." *Engineering Fracture Mechanics*, Vol 15, No. 1-2 (Great Britain:1981), pp. 185-192.
- Payne, M. and P. McIntyre. "Influence of Grain Boundary Microstructure on the Susceptibility of Alloy 600 to Intergranular Attack and Stress Corrosion Cracking." *Corrosion-NACE*, XLIV no. V, (May 1988), pp. 314-319.
- Rebak, R.B. and Z. Szlarska-Smialwska, "Influence of Stress Intensity and Loading Mode on Intergranular Stress Corrosion Cracking of Alloy 600 in Primary Water of Pressurized Water Reactors." *Corrosion*, Vol. 50, No. 5, (May 1994), pp. 378-393.
- Rios, R., T. Magnin, D. Noel, O. DeBouvier. "Critical Analysis of Alloy 600 Stress Corrosion Cracking Mechanisms in Primary Water." *Metallurgical and Materials Transactions A*, Vol. 26, No. 4, (1995), pp. 925-939.
- Roberts, J.T. Adrian. *Structural Materials in Nuclear Power Systems*. New York: Plenum Press (1981).
- Scaffer, Saxena, Antolovich, Sanders and Warner. *The Science and Design of Engineering Materials*. Chicago: Irwin (1995).

- Scarberry, R.. "Corrosion of Nickel Based Alloys." Conference Proceedings. American Society of Metals. Metals Park, 1985.
- Shah, V.N., D.B. Lowenstein, A.P.L. Turner, S.R. Ward, J.A. Gorman, P.E. MacDonald, G.H. Weidenhamer. "Assessment of Primary Water Stress Corrosion Cracking of PWR Steam Generator Tubes." *Nuclear Engineering and Design*, Vol. 134, No. 2-3, pp. 199-216.
- Shen, Y. and P. G. Shewmon. "Intergranular Stress Corrosion Cracking of Alloy 600 and X-750 in High Temperature Deaerated Water/Steam." *Metallurgical Transactions A*, Vol. 22A, No. 8, (August 1991), pp. 1857-1864.
- Sung, J. K., J. Koch, T. Angeliu, and G.S. Was. "The Effect of Grain Boundary Chemistry on Intergranular Stress Corrosion Cracking of Ni-Cr-Fe Alloys in 50 Pct NaOH at 140°C." *Metallurgical Transactions A*, Vol. 23A, No. 10, (October 1992), pp. 2887-2904.
- Todreas, Neil E. and Mujid S. Kazimi. *Nuclear Systems I*. Bristol, PA: Taylor & Francis, 1990.
- Uhlig, Herbert H. and R. Winston Revie. *Corrosion and Corrosion Control*. New York: John Wiley & Sons, 1985.
- Van Vlack, L. H.. *Elements of Material Science and Engineering*. 3rd Ed.. Reading, MA: Addison-Wesley Publishing Co. (1975).
- Verpoest, I., E. Aernoudt, A. Deruyttere, and M. Neyrinck. "An Improved A.C. Potential Drop Method For Detecting Surface Microcracks During Fatigue Tests of Unnotched Specimens." *Fatigue of Engineering Materials and Structures*, Vol 3 (1981),pp. 206-209.
- Wagner, C.. Discussions at the First International Symposium on Passivity, Heiligenberg, West Germany, 1957. *Corrosion Science*. Vol 5, (1965).
- Woodward, J. "Rapid Identification of Conditions Causing Intergranular Corrosion or Intergranular Stress Corrosion Cracking in Sensitized Alloy 600." *Corrosion - NACE*, XL, No. XII, (December 1984), pp. 640-643.

## A-1. Autoclave System Operating Characteristics

This appendix contains information describing heater controller settings, autoclave heatup characteristics, and a description of the autoclave head ring failures which occurred during early testing due to a failure to completely purge the autoclave volume of oxygen. This information is provided to provide a benchmark for system operating performance during future testing.

### A-1.1 Omega CN9000A Heater Controller Parameter Settings

The CN9000 Heater Controller manufactured by Omega Engineering, Inc. is a Proportional-Integral-Differential controller. The controller has a self-tune mode which allows the parameters to be automatically calculated during the heatup. However, the auto-tune feature has a time-out routine in the software which will terminate the auto-tune calculation after a predetermined time, which is preset by the manufacturer. This occurred during the heatup tests in the static mode. As an alternative, the PID parameters may be manually calculated from observation of the autoclave temperature oscillations during heatup. Detailed procedures are in the CN9000 Operators Manual(M575/O289).

A heatup of the autoclave was conducted with a set temperature of 280°C in order to obtain the necessary parameters without exceeding the 315°C rated autoclave temperature. When the set temperature was reached by allowing the controller to operate in a manual mode with the PID controller inactive, oscillations occurred as expected. Measurements of the amplitude and period of the oscillations were obtained from a graph of the temperature versus time from

the LABVIEW® (figure A-1). The required parameters are calculated and presented in Table A-1.

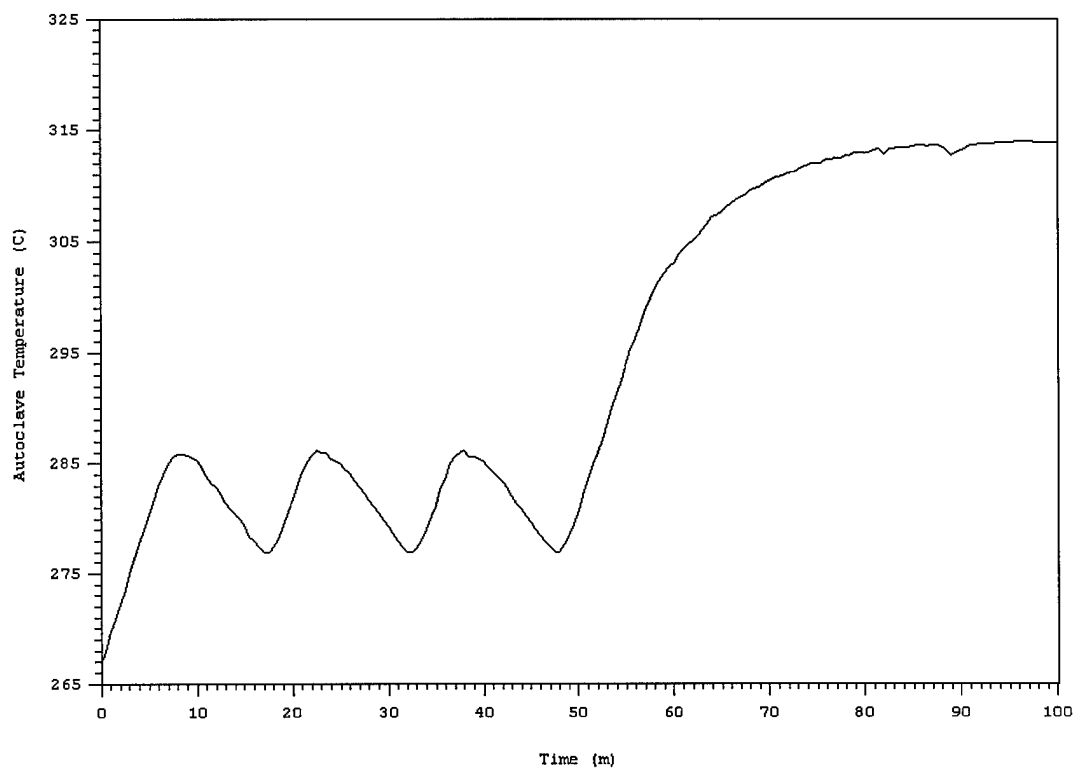


Figure A-1-1: Heatup 950726 Showing Oscillations of the Heater Controller. The Amplitude Was Measured at 9°C with a Period of 15 Minutes.

CN9000A Heater Controller PID Parameters		
Measured Amplitude: 9°C		Measured Period: 15 minutes
PID Parameter	Governing Equation	Result (Setting)
Proportional Time	T/20	45 seconds
Proportional Band (%)	Ax150/Full Scale	3.375% (5%)
Derivative Time	T/10	90 (50) seconds
Integral Time	T	900 (1080) seconds

Table A-1-1 : CN9000A PID Controller Parameters for Static Autoclave Operation

### A-1.2 Heatup Plots

Time to heatup is a function of the fluid quantity in the autoclave and the heat loss of the system. The heating mantle generates 2700 watts total heat output. Based on the two operating modes, this output is sufficient to heat the autoclave to the desired  $315^{\circ}\text{C}$ . However, since heat is lost at a greater rate in recirculate mode due to the incoming cold fluid and larger fluid volume in the autoclave, additional insulation on the head and preheating of the incoming fluid is necessary to provide reasonable heatup times. Testing showed that heatup to temperature requires approximately two hours in static mode and six hours in recirculate mode. Figure A-2 shows the heatup plots during normal static and recirculate heatups. The fluid is preheated to  $80^{\circ}\text{C}$  using a heat tape on the incoming tubing for the recirculate mode of operation.

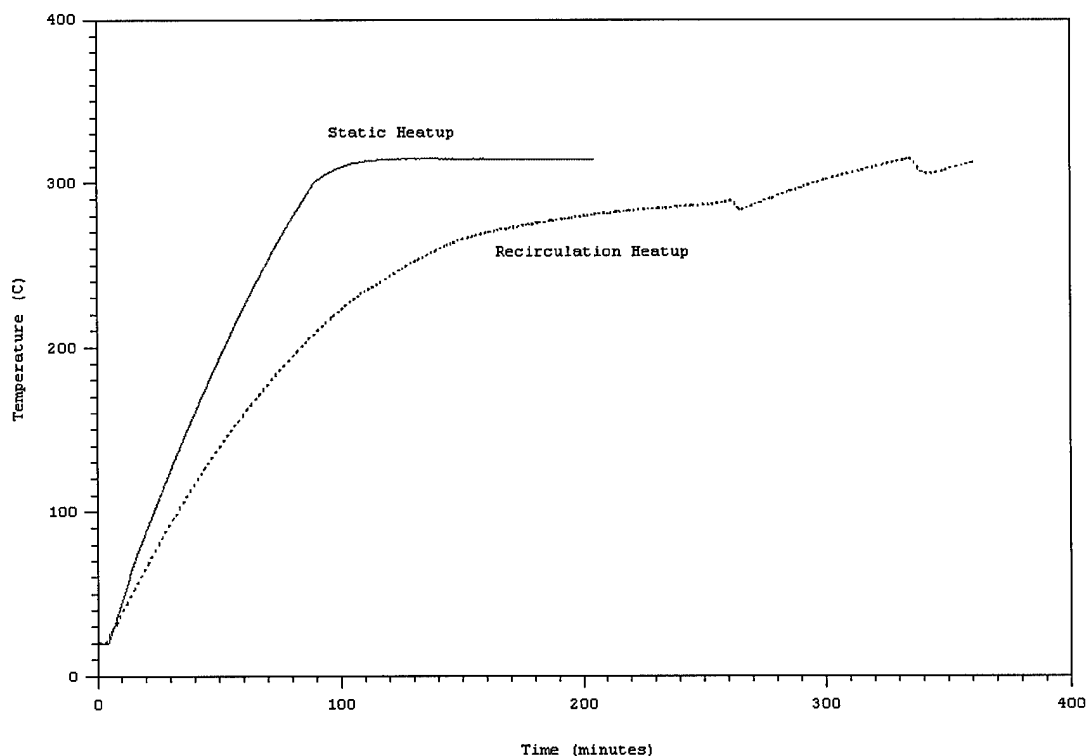


Figure A-1-2: Heatup Plot Showing Contrast in Time Between Recirculation and Static Modes



### A-1.3 Autoclave Head Seal Ring Failures

Cracking of the nickel O-ring which seals the head and autoclave body occurred during two early caustic tests while operating in recirculation mode. The failures occurred within 100 hours of reaching final autoclave temperature. Post shutdown inspections revealed a green residue on the interiors of the autoclave head and body. Although no formal chemical analysis was performed, the residue was thought to be nickel oxide or nickel hydroxide. Inspection of the O-ring indicated radial cracking with signs of erosion in one location (figures A-3 and A-4).

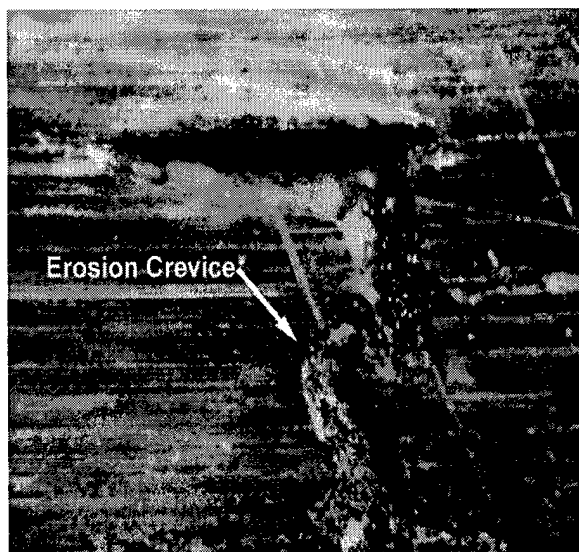


Figure A-1-3: Channel in O-ring  
from Test 950703

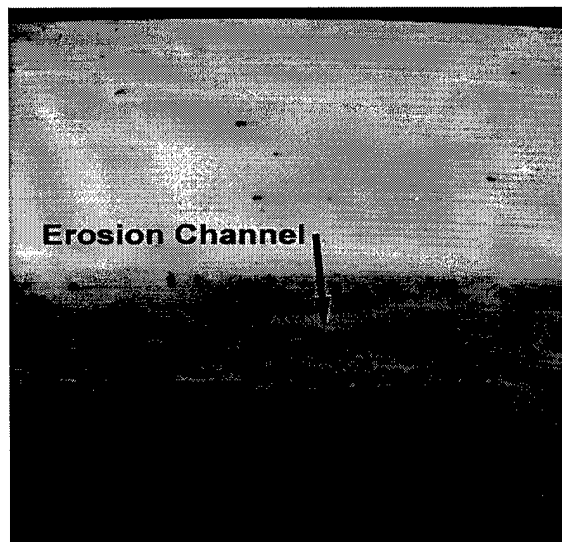


Figure A-1-4: Erosion Damage to O-  
Ring from Test 950403

Based on the best available data from the post-shutdown analysis, the cracking is thought to be from oxygen which was not purged from the nipples prior to heatup. The oxygen was forced into solution during the subsequent fill. Once at temperature, the oxygen in caustic attacked the O-ring which is

subject to a large compressive stress. The greater thermal expansion of the nickel versus the carbon steel head bolts further increases the compressive stress on the O-ring during heatup. Areas of increased stress due to a prior flaw are probably where the cracking initiated. The failure of the O-rings resulted in system shutdown due to a loss of autoclave pressure.

Future O-ring cracking while operating in recirculation mode should not occur. The autoclave head was modified to allow thorough purging of the oxygen in the nipples by installation of valves at the high points (ACV-1 through 6).

## A-2. Operating Procedures

This appendix contains detailed procedures for operating the autoclave system in all modes. Emergency procedures are included to rapidly shut down the system in an emergency. Operation of the system using these procedures should prevent equipment damage and minimize any personnel hazards.

## A-2.1 System Startup Procedure - Static Operation.

### A-2.1.1 Prerequisites

a. The sample is installed in the head and the head is bolted onto the autoclave. Ensure the head is torqued to 125 to 140 foot-pounds. Verify all Conax fittings are torqued to the required values to prevent hydrogen leakage.

b. All external tubing connections are installed to the head. The heating mantle is installed with required thermal insulation bolted in place (i.e. lower autoclave thermal insulation disk).

c. Cooling jacket water is connected to the head. Ensure cooling water is turned on and flow verified prior to startup.

d. The main electrical panel breakers are shut for 250 volt service to the heater controller. 120 volt service is available to the heater controller and control systems. Verify all heating mantle electrical connections are complete.

e. 50 to 75 psig compressed air service is connected to regulator REG-3 and solenoid S-2.

f. Nitrogen bottle pressure should be a minimum of 1500 psig to prevent frequent booster pump cycling.

g. Hydrogen bottle pressure is a minimum of 2000 psig. Pressure below this will result in operation closer to solution saturation temperature.

h. Solenoid S-2 Emergency Dump Switch is in "SHUT".

i. System Override Switch is in "STARTUP".

j. The system has been purged of oxygen by an inert gas for at least 15 minutes through each valve ACV-1 through ACV-6 (NOTE: if the gas inlet is through the outlet union cross, then purging through ACV-2 is not required).

k. The injection system is connected or capped at the autoclave standoff.

l. Connect or verify connected all thermocouple leads. This includes the dual junction thermocouple for internal autoclave temperature and the return tubing external temperature.

m. The following valve lineup is completed:

Static System Operation : Startup Valve Lineup			
Valve	Position	Valve	Position
AC-1	SHUT	ACV-4	SHUT
AC-2	SHUT	ACV-5	SHUT
AC-3	OPEN	ACV-6	SHUT
AC-4	SHUT	SP-1	SHUT
AC-5	OPEN	SP-2	OPEN
AC-6	OPEN	SP-3	OPEN
ACV-1	OPEN	SP-4	THROTTLED OPEN
ACV-2	SHUT	REG-1	FULL OPEN
ACV-3	SHUT	REG-2	SHUT
INJ-1	TO VENT	REG-3	SHUT
SV-1	SHUT	ST-1	SHUT

Table A-2-1: Static System Start-Up Valve Lineup

#### A-2.1.2 Procedure

a. SLOWLY open the Hydrogen Tank Isolation Valve to pressurize the system up to the inlet of REG-2.

b. Operate REG-2 slowly to pressurize the system to 1800 psig. Adjust REG-2 as necessary to maintain the system pressure 1750 to 1850 psig.

c. Once the system pressure is 1750 to 1850 psig, the sample may be internally pressurized to obtain the desired stress across the wall. See the sample pressurization procedure. When the sample internal pressure exceeds the low pressure shutdown setpoint, reset the shutdown on meter NP-1.

d. Reset meter ACP-1 once pressure exceeds 1600 psig.

e. When all shutdown signals are reset, place the System Override Switch in "NORMAL".

f. Set or verify the setpoint temperature is  $315 \pm 2^{\circ}\text{C}$  on the CN9000 Series Heater Controller (See the Operators Manual).

g. Turn the CN9000 Series Heater Controller on per the Operator's Manual instructions. Shut the heater latch contactor on the rear of the control panel by pushing the green "START" button. A distinct latch sound should be heard. If not, check for a power interruption to the heater controller or control circuit.

h. Monitor the heatup to verify normal heatup characteristics (see Appendix 1). It normally requires approximately 2 hours to reach set temperature.

## A-2.2 System Startup Procedure - Recirculation.

### A-2.2.1 Prerequisites

a. The sample is installed in the head and the head is bolted onto the autoclave. Ensure the head is torqued to 125 to 140 foot-pounds. Verify all Conax fittings are torqued to the required values to prevent caustic leakage.

b. All external tubing connections are installed to the head. The heating mantle is installed with required thermal insulation bolted in place (i.e. lower autoclave thermal insulation disk).

c. Cooling jacket water is connected to the head. Ensure cooling water is turned on and flow verified prior to startup.

d. The main electrical panel breakers are shut for 250 volt service to the heater controller. 120 volt service is available to the heater controller and control systems. Verify all heating mantle electrical connections are complete.

e. 50 to 75 psig compressed air service is connected to regulator REG-3 and solenoid S-2.

f. Nitrogen bottle pressure should be a minimum of 1500 psig to prevent frequent booster pump cycling.

g. The storage tank contains a minimum of 50 liters of cold caustic solution which has been adequately deaerated.

h. Solenoid S-2 Emergency Dump Switch is in "SHUT".

i. System Override Switch is in "STARTUP".

j. The system has been purged of oxygen by an inert gas. This should be accomplished by backfilling the system with an inert gas prior to filling the system solid with caustic. ENSURE THE STANDOFFS ARE PURGED VIA ACV-1 THROUGH ACV-6.

k. The injection system is connected or capped at the autoclave standoff.

l. Connect or verify connected all thermocouple leads. This includes the dual junction thermocouple for internal autoclave temperature and the return tubing external temperature.

m. Adjust the recirculation pump flow to maximum (see operating manual).

n. The following valve lineup is completed:

Recirculation System Operation : Startup Valve Lineup			
Valve	Position	Valve	Position
AC-1	OPEN	ACV-4	SHUT
AC-2	SHUT	ACV-5	SHUT
AC-3	OPEN	ACV-6	SHUT
AC-4	SHUT	SP-1	SHUT
AC-5	SHUT	SP-2	OPEN
AC-6	SHUT	SP-3	OPEN
ACV-1	OPEN	SP-4	THROTTLED OPEN
ACV-2	SHUT	REG-1	FULL OPEN
ACV-3	SHUT	REG-3	SHUT
INJ-1	TO VENT	ST-1	OPEN
ST-2	THROTTLED OPEN		

Table A-2-2: Recirculation System Start-Up Valve Lineup

#### A-2.2.2 Procedure

a. Place the recirculation pump in "RUN"

b. Once the system is verified solid (flow sounds to tank, small pressure increase on meter, etc.), adjust REG-1 slowly to pressurize the system to  $1800 \pm 50$  psig.

c. Once the system pressure is 1750 to 1850 psig, the sample may be internally pressurized to obtain the desired stress across the wall. See the sample pressurization procedure. When the sample internal pressure exceeds the low pressure shutdown setpoint, reset the shutdown on meter NP-1.



d. Reset meter ACP-1 once pressure exceeds 1600 psig.

e. When all shutdown signals are reset, place the System Override Switch in "NORMAL".

f. Set or verify the setpoint temperature is  $315 \pm 2^{\circ}\text{C}$  on the CN9000 Series Heater Controller (See the Operators Manual).

g. Turn the CN9000 Series Heater Controller on per the Operator's Manual instructions. Shut the heater latch contactor on the rear of the control panel by pushing the green "START" button. A distinct latch sound should be heard. If not, check for a power interruption to the heater controller or control circuit.

h. Monitor the heatup to verify normal heatup characteristics.

## A-2.3 System Shutdown Procedure - Static Operation

### A-2.3.1 Prerequisites

a. The system is operating at set temperature and pressure. No shutdown signals are present.

### A-2.3.2 Procedure

a. Place the System Override Switch in "OVERRIDE".

b. Shut the Hydrogen Bottle Isolation Valve.

c. Reduce the internal sample pressure to atmospheric by shutting the Nitrogen bottle isolation valve and reducing air pressure to the booster pump to 0 (REG-3). Throttle open SP-1 to vent the nitrogen to the atmosphere.

d. Turn the heater controller off (see Operator's Manual).

e. Open the heater latch contactor by depressing the red "STOP" button on the contactor housing.

f. If a quick return to operating status is intended, AC-5 and AC-6 may be shut to maintain hydrogen pressure in the scrubber. The autoclave may be vented by throttling open ACV-1 through ACV-6 or by opening AC-4 to the storage tank.

## A-2.4 System Shutdown Procedure - Recirculation

### A-2.4.1 Prerequisites

a. The system is operating at set temperature and pressure. No shutdown signals are present.

### A-2.4.2 Procedure

a. Place the System Override Switch in "OVERRIDE".

b. Reduce the internal sample pressure to atmospheric by shutting the Nitrogen bottle isolation valve and reducing the air pressure to the booster pump to 0 (REG-3). Throttle open SP-1 to vent the nitrogen to the atmosphere.

c. Turn the heater controller off (see Operator's Manual).

d. Open the heater latch contactor by depressing the red "STOP" button on the latch contactor housing.

f. Continue to operate the recirculation pump throughout the cooldown. NOTE: A RAPID DECREASE IN PRESSURE MAY OCCUR DUE TO SYSTEM CONTRACTION ONCE THE HEATER IS TURNED OFF. This is not unusual and should not be mistaken for a pump or backpressure regulator failure. Continue to operate the pump and pressure will be restored when the makeup exceeds the contraction (at about 200°C).

g. When temperature is reduced below 100°C, the system pressure may be reduced by operating REG-1 and the recirculation pump secured.

## A-2.5 Emergency Shutdown Procedures

These procedures may be used to rapidly shutdown the system in an emergency (such as a leak) or to place the system in a shutdown configuration if an automatic shutdown occurs.

### A-2.5.1 Static System Emergency Shutdown

- a. Open the heater latch contactor by depressing the red "STOP" button on the contactor housing.
- b. Place Solenoid S-2 Emergency Dump Switch in "OPEN".
- c. Shut the isolation valves on the Nitrogen and Hydrogen bottles as quickly as possible.

### A-2.5.2 Recirculation System Emergency Shutdown

- a. Open the heater latch contactor by depressing the red "STOP" button on the contactor housing.
- b. Place Solenoid S-2 Emergency Dump Switch in "DUMP".
- c. Shut the isolation valves on the Nitrogen bottle as quickly as possible.
- d. If a leak has occurred, secure the recirculation pump to avoid additional caustic from entering the autoclave. Depressurize the system by rapidly opening REG-1. CAUTION: THE SYSTEM MAY BE DEPRESSURIZED BY OPENING AC-2 HOWEVER, CAUSTIC WILL VENT TO THE ATMOSPHERE!

## A-2.6 Sample Pressurization System Operation

### A-2.6.1 Startup

#### a. Prerequisites

1. All tubing is assembled to the sample in accordance with the manufacturer's instructions.

2. Nitrogen bottle pressure is a minimum of 1500 psig to prevent frequent cycling of the booster pump.

3. 50 to 75 psig compressed air service to regulator REG-3 and S-2 is available.

4. The system low pressure shutdown is reset or the System Override Switch is in "OVERRIDE".

#### b. Procedure

1. Slowly open the Nitrogen bottle Isolation Valve. Sample pressure on NP-1 and NP-2 should indicate approximately the same as the Nitrogen bottle pressure.

2. Raise the internal sample pressure by operating REG-3. The approximate internal pressure as read at NP-1 and NP-2 should be 150 times the applied air pressure as read at REG-3. The Booster pump will cycle to maintain this pressure within an approximate 200 psig band. Allow pressure to stabilize before REG-3 is locked to the final setting.

## A-2.7 Injection System Operation

### A. Prerequisites

1. An inert gas supply is available to deaerate and agitate the inhibitor while in the tank. The gas is also required to provide a positive head to the injection pump. The gas supply line is attached to the fitting on the injection tank.

2. The solution to be injected is in the injection tank. The fill plug on the tank has been replaced.

3. The following valves are in the position noted:

Injection System Valve Lineup			
Valve	Position	Valve	Position
INJ-1	TO VENT	INJ-2	SHUT
AC-2	SHUT		

Table A-2-3: Injection System Start-Up Valve Lineup

4. 120 VAC Service Power is connected to the injection pump.

5. If agitation or deaeration of the solution is required, attach a vent line to INJ-2 prior to opening.

6. A collection bottle should be placed at the common vent prior to pressurizing the tank.

7. CAUTION: NEVER START THE PUMP WITH A HEAD GREATER THAN 1000 PSIG AGAINST THE PUMP OUTLET.

### B. Procedure

1. Pressurize the injection tank to approximately 10 psig by adjusting the gas bottle regulator. If deaeration or agitation of the solution is required, INJ-2 should be throttled open to adjust the flowrate through the injection tank while maintaining tank pressure at approximately 10 psig.

2. Set the injection pump flow to the desired rate with the micrometer on the pump.

3. Start the pump. Verify flow through the vent. After a few seconds, place INJ-1 in the "INJECT" position. Monitor autoclave pressure carefully to ensure the system does not overpressure.

4. When solution injection is complete, place INJ-1 in the "TO VENT" position. Stop the pump.

5. Shut off the gas pressure to the injection tank.

6. Vent the tank by opening INJ-2 fully.

## A-2.8 Electroless Nickel Plating Technique

This electroless nickel plating technique was developed by Dr. Martin Morra<sup>1</sup> as an aid in preserving surface features during metallographic preparation. While commercial kits for electroless nickel plating are available, this technique was developed specifically for superior retention of fine surface details. The hard, resilient plating also makes this technique ideal for the Alloy 600 sample preparation.

### A-2.8.1 Preparation

a. Clean all glassware to be used to store or hold the plating solution with a 50% nitric acid-50% deionized water (by volume) solution heated to 90° to 100°C.

b. Prepare 2 liters of plating solution by mixing 54 grams of Sodium Hypophosphite ( $\text{NaH}_2\text{PO}_2 \cdot \text{H}_2\text{O}$ ), 40 grams of Nickel Sulfate Hexahydrate ( $\text{NiSO}_4 \cdot 6\text{H}_2\text{O}$ ) and 32 grams of Sodium Succinate Hexahydrate ( $\text{C}_4\text{H}_4\text{Na}_2\text{O}_4 \cdot 6\text{H}_2\text{O}$ ) in 2 liters of deionized water. Mix the plating solution by stirring until the solids have totally dissolved.

c. Filter the plating solution with a lint free filter. A membrane filter (1 $\mu\text{m}$  pore size) used under vacuum is preferable although a glass fiber filter may be used for gravity filtration.

d. Areas of the sample not to be plated should be covered with micro-stop and allowed to dry for 24 hours. Clean the sample to be plated with an appropriate solvent (isopropyl alcohol) to remove any oils from the surface. Do not handle the sample after cleaning.

---

<sup>1</sup> M.M. Morra, J.M. Morra and R.R. Biederman, "A Technique for the Preparation of Powders for Examination by Transmission Electron Microscopy", *Materials Science and Engineering*, A124 (1990) pp. 55-64.



#### A-2.8.2 Procedure

CAUTION: The plating solution must be heated to activation temperature in a water bath. DO NOT ATTEMPT TO HEAT THE SOLUTION ON A HOT PLATE!

a. Suspend a 2000 milli-liter beaker in a 4000 milli-liter beaker. Pour enough water in the 4000 milli-liter beaker to immerse most of the 2000 milli-liter beaker. Heat the bath.

b. Pour the plating solution into the 2000 milli-liter beaker allowing room for the sample without over-flowing.

c. Suspend the sample in the plating solution. For best results, do not allow the sample to touch the surface of the beaker. DO NOT COVER THE BEAKER DURING PLATING!

d. Allow the temperature of the plating solution to rise to between 85° and 91°C.

e. The initial pH of the plating solution should be approximately 5.5 to 6.0 (test using pH paper).

f. Monitor the plating solution carefully for the first half hour after plating has begun (the rapid evolution of bubbles from the sample surface). If a white precipitate forms in the solution (it will cloud the solution), add lactic acid drop-wise and stir until the precipitate disappears (solution clears). WHEN ADDING LACTIC ACID, BE SURE THE pH DOES NOT FALL BELOW 5.5!

g. Depending on the surface of the sample, the rate of nickel deposition will be approximately 1 mil per hour. If a problem initiating plating on the sample develops, it is suggested that the sample's oxide layer be removed by placing it in a heated solution (approximately 60°C) of 2% Hydrofluoric Acid, 2% Nitric Acid in deionized water (by volume) for a few moments. The above procedure should then be repeated.

h. When excessive plating occurs on the glassware, remove the sample and cool the solution. Additional plating thickness may be obtained by repeating the above procedure as required.

### A-3. Detailed System Drawings

The following pages present the detailed system design and construction drawings used in assembly of the alloy 600 test platform. Detailed listings of components are included with a listing of the manufacturer from whom the part was procured. Alternate sources of components which possess similar specifications may be substituted for those listed. Several components were custom assembled within the lab or were previously assembled and the source may not be known. The layout of connecting tubing is provided as a guide. The exact dimensions and bends were made to custom fit the valve locations on the test stand boards and on the autoclave.

Post-assembly testing consisted of system hydrostatic tests using the installed pumps as a source. A Heise gauge and digital pressure meter served as the pressure monitoring equipment. A hydrostatic test using distilled water was considered successful if no leaks occurred in the system under test for a period of thirty minutes. Components which would be pressurized at temperatures greater than room temperature were hydrostatically tested at room temperature and at their operating temperature.

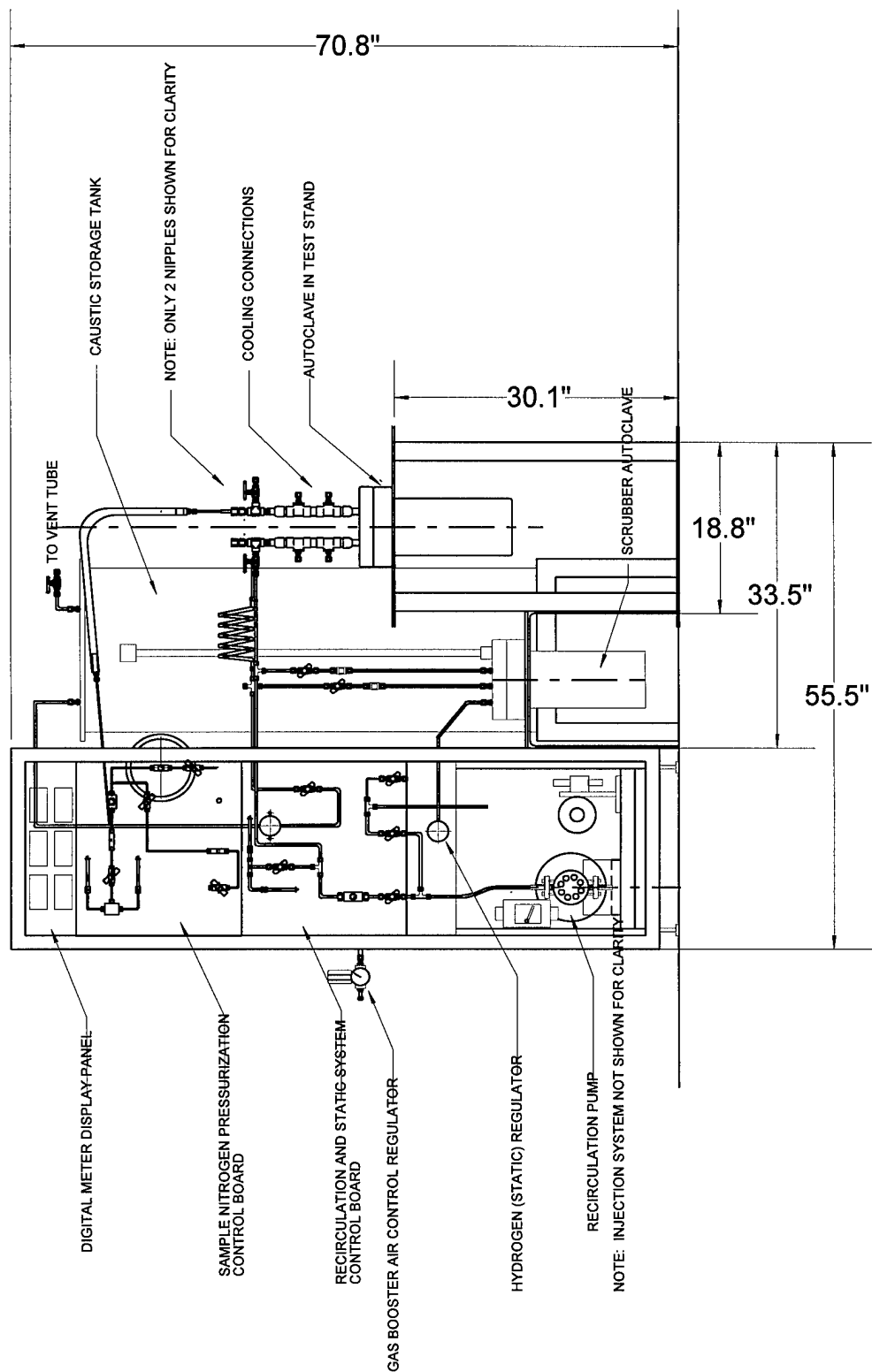
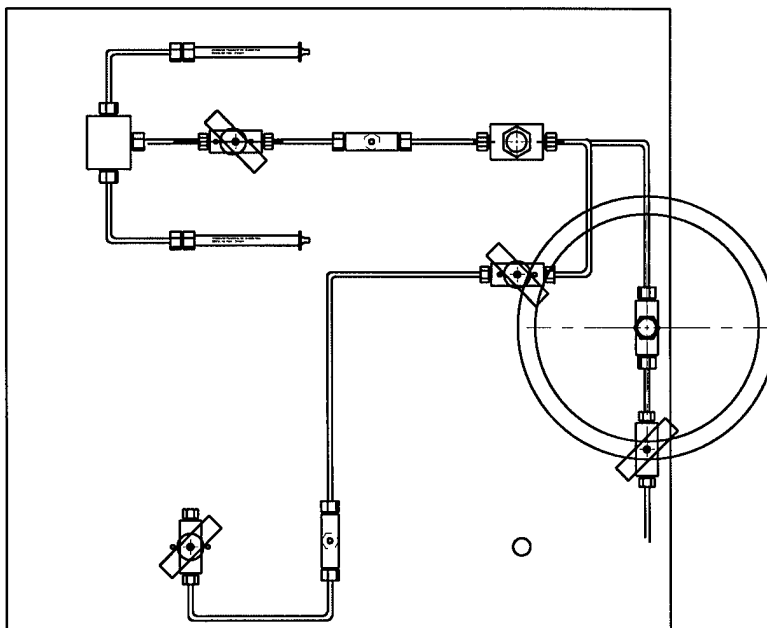
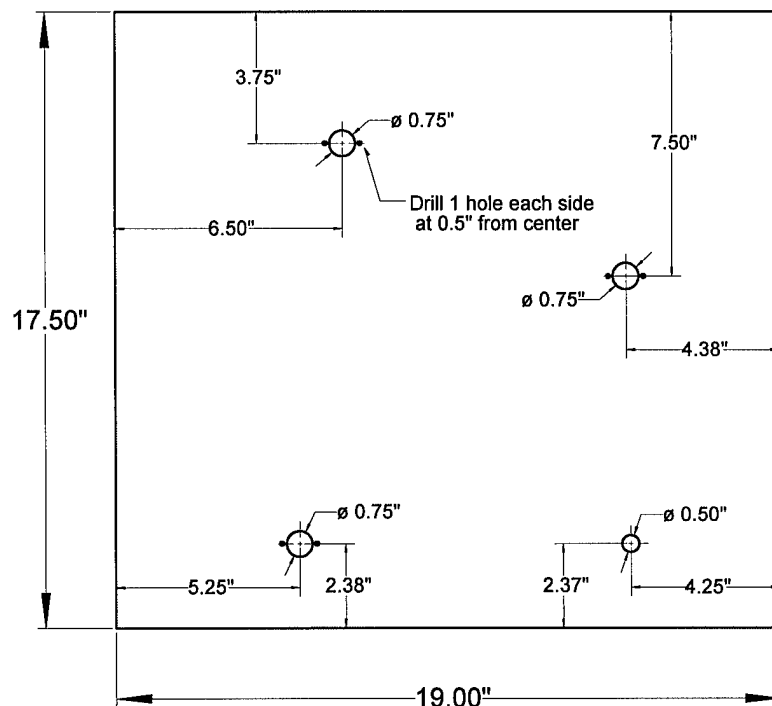


Figure A-3-1 : Alloy 600 Test System



Sample Nitrogen Board Showing Valve Layout



Sample Pressurization Board Drill Template

Figure A-3-2: Sample Pressurization Control Board Tubing and Template Details

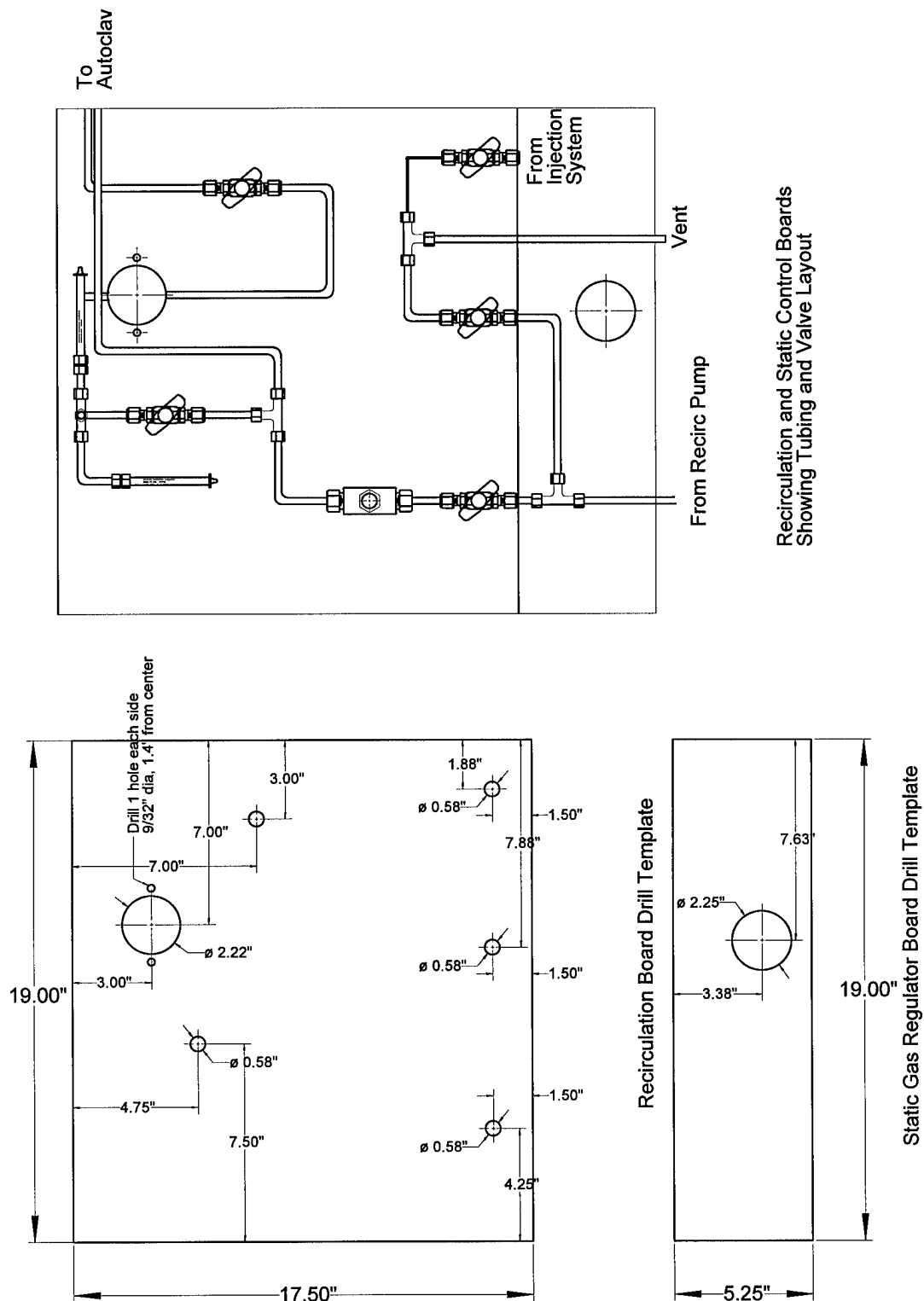


Figure A-3-3: Recirculation and Static System Control Board Tubing and Template Details

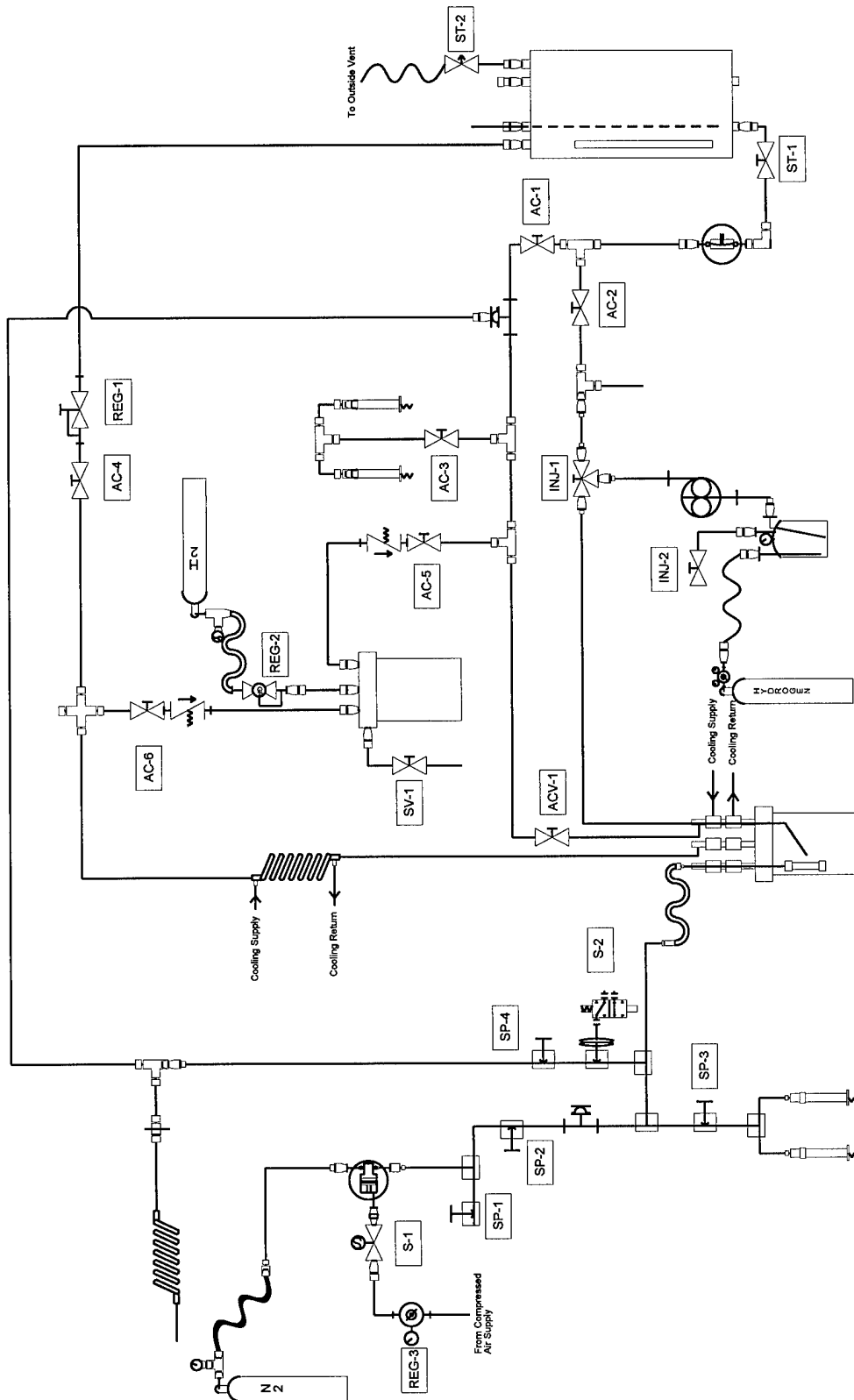


Figure A-3-4: Alloy 600 Test Platform Schematic

Alloy 600 Test Platform Components List					
Quantity	Part Number	MAWP	Material	Manufacturer	Description
1		150 psig	Brass		Solenoid Operated Two Way Valve
1			Titanium	Autoclave Engineer	Autoclave - 4 liter
1			Copper	Custom	Single Element Cooling Coil
1			Alloy 600	Custom	Alloy 600 Sample
1	KIP 141161	100 psid	Brass	Minuteman Controls	Three Way Solenoid Valve
1		10 psig	Stainless Steel	Custom	200 Liter Storage Tank w/ Sight Glass
1	62535L	10000 psig	Stainless Steel	Boston Hydraulics	0-10000 psig Liquid Gage
1	FZ-1612	10000 psig	Stainless Steel	Boston Hydraulics	3/8" Street Tee -Hydraulic Fitting
1		100psig@315C	Nickel-200	High Pressure Equipment	Autoclave w/ Cooling Jackets on Standoffs
1		130 psig	Stainless Steel	McMaster Carr	9 liter SS Injection Tank
1	AMFLO 2100	150 psig	Steel	Bridge Products Inc	Single Stage Air Regulator
1		2000 psig	Hydrogen, Grade 5	Middlesex Gas	200 cuft Hydrogen w/ 2 Stage Reg
1		3000 psig	Nitrogen, Grade 4.8	Middlesex Gas	300 cuft Nitrogen Tank, Grade 4.8, w/Connector
1		3000 psig	Brass Case		0-3000 psig Gage
1		6000 psig	Stainless Steel	Grove	Gas Regulator
1		6000 psig	Hydrogen	Middlesex Gas	500 cuft Grade 5 Hydrogen Tank with Connector
1	10-63AF4	10000 psig	Stainless Steel	High Pressure Equipment	1/4" Tee Type Safety Head
1	10V2	11000 psig	Stainless Steel	Autoclave Engineers	Air-To-Close Diaphragm Valve
1	15-63AF2	15000 psig	Stainless Steel	High Pressure Equipment	1/8" Tee Type Safety Head
1	2-4 FBZ-SS	9100 psig	Stainless Steel	Parker	1/4"MPT to 1/8" CPI/A-Lok
1	2-4 GBZ-SS	10000 psig	Stainless Steel	Parker	1/4" FPT to 1/8" CPI Female Connector
1	396-89	5000psig	Stainless Steel	LDC Analytical	MiniPump Metering Pump
1	4 FNZ-SS	10000 psig	Stainless Steel	Parker	1/4" CPI Plug
1	4-4 EBZ-SS	10000 psig	Stainless Steel	Parker	1/4" CPI/A-Lok Union Elbow
1	4-4 WBZ-SS	10000 psig	Stainless Steel	Parker	1/4 Bulkhead Union
1	4-4-4 FT-SS	5600 psig	Stainless Steel	Parker	1/4" FPT Female Tee
1	4-8 FBZ-SS	6600 psig	Stainless Steel	Parker	1/2" MPT to 1/4"CPI/A-Lok Male Connector
1	4-KBZ-SS	10000 psig	Stainless Steel	Parker	Union Cross - 1/4" CPI fittings
1	4F-B6XS2-SSP	6000psig	Stainless Steel	Parker	Three Way Spring Loaded Ball Valve
1	4Z(A)-V2LN-SS	5000 psig	Stainless Steel	Parker	1/4 Tube CPI General Purpose Needle Valve
1	680-S-E	3000psig	Stainless Steel/PTF	Pulsa Feeder	Diaphragm Recirculation Pump
1	6M24C8	10000 psig	Stainless Steel	Autoclave Engineers	1/8" AE SpeedBite to 1/4" FPT
1	8-6 MHN-B	3900 psig	Brass	Parker	1/2 MPT to 3/8 MPT Hex Nipple
1	AG-152	20000 psig	Carbon Steel	Haskel	Gas Booster Pump
1	FC372-03	3000 psig	Polyon	Aeroquip	Polyon High Pressure Gas Line
1	N/A	10000 psig (l)	SS/Copper	Custom	Cooling Coil
1	Series 1700	3000 psig	Stainless Steel	Tescom	Backpressure Regulator
2	H-915	10000 psig	Stainless Steel Fit	Boston Hydraulics	Non-Conductive High Pressure Hydraulic Hose
2		200 psig	PolyEthylene		1/4" OD Plastic Tube
2	4-4 GBZ-SS	5600 psig	Stainless Steel	Parker	1/4"FPT to 1/4"CPI/A-Lok Female Connector
2	4-4-4 MBZ-SS	10000 psig	Stainless Steel	Parker	1/4" Female Run Tee
2	4Z(A)-CO4L-10-V-SS	6000 psig	SS/Viton	Parker	O-Ring Poppet Check Valve
2	6-6 FBZ-SS	7200 psig	Stainless Steel	Parker	3/8" MPT to CPI Male Connector
2	P605-X	22500 psig	17-4 PH SS	Omega Engineering	0-15000 psig Transducer
2	P605-X	4500 psig	17-4 PH SS	Omega Engineering	0-3000psig Transducer
3	15M42B1	60000 psig	Stainless Steel	Autoclave Engineers	1/4" High Pressure to 1/8" SpeedBite
3	2-4 FBZ-SS	7500 psig	Stainless Steel	Parker	1/4" MPT to 1/4" CPI Male Connector
3	4-6 FBZ-SS	7200 psig	Stainless Steel	Parker	3/8"MPT to 1/4"CPI Male Connector
3	FZ-1630	10000 psig	Stainless Steel	Boston Hydraulics	3/8" FPT to 1/4" MPT Bushing
4	1-4 FBZ-SS	10000 psig	Stainless Steel	Parker	Male Connector - 1/4"MPT to 1/16"CPI/A-Lok
4	10V2081	11000 psig	Stainless Steel	Autoclave Engineers	2 Way 1/8" Isolation Valve
4	4-4-4 JBZ-SS	10000psig	Stainless Steel	Parker	1/4 CPI/A-Lok Union Tee
4	ST2220	11000	Stainless Steel	Autoclave Engineer	Tee - 1/8"
10	4-4 FBZ-SS	10000 psig	Stainless Steel	Parker	1/4" Male Connector
10	4Z(A)-B2LJ2-SSP	6000psig	Stainless Steel	Parker	Two Way Ball Valve - 1/4" CPI Fittings

Table A-3-1: Alloy 600 Test Platform Components Summary

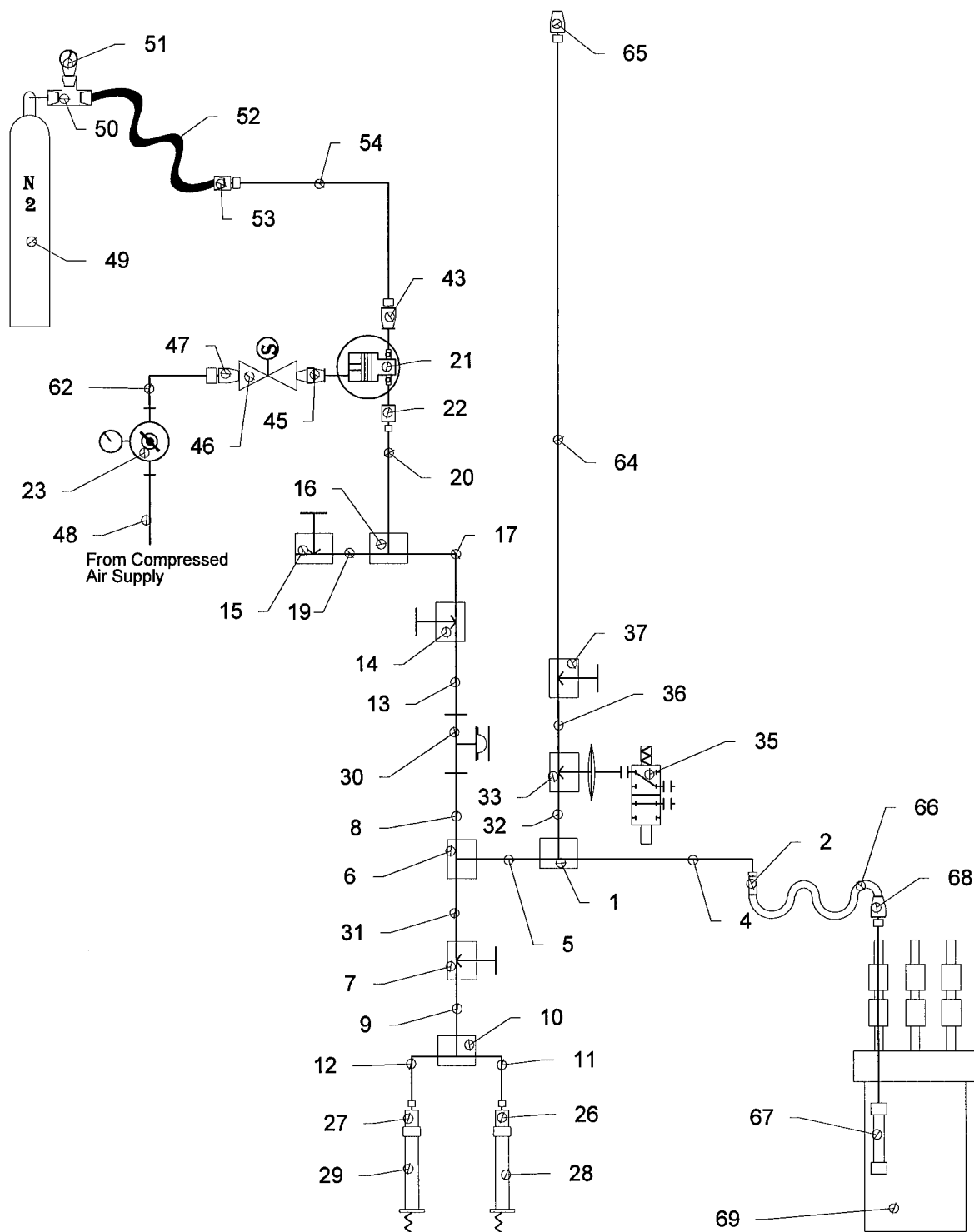


Figure A-3-5: Sample Pressurization System Component ID



Sample Pressurization Component Identification List					
UID	Part Number	MAWP	Material	Manufacturer	Description
1	ST2220	11000 psig	Stainless Steel	Autoclave Engineer	Tee - 1/8"
2	6M24C8	10000 psig	Stainless Steel	Autoclave Engineers	1/8" AE SpeedBite to 1/4" FPT
4		15000 psig	Stainless Steel	Metal Men	0.125" x .035" Tubing
5		15000 psig	Stainless Steel	Metal Men	0.125" x .035" Tubing
6	ST2220	11000	Stainless Steel	Autoclave Engineer	Tee - 1/8"
7	10V2081	11000 psig	Stainless Steel	Autoclave Engineers	2 Way 1/8" Isolation Valve
8		15000 psig	Stainless Steel	Metal Men	0.125" x .035" Tubing
9		15000 psig	Stainless Steel	Metal Men	0.125" x .035" Tubing
10	ST2220	11000 psig	Stainless Steel	Autoclave Engineer	Tee - 1/8"
11		15000 psig	Stainless Steel	Metal Men	0.125" x .035" Tubing
12		15000 psig	Stainless Steel	Metal Men	0.125" x .035" Tubing
13		15000 psig	Stainless Steel	Metal Men	0.125" x .035" Tubing
14	10V2081	11000 psig	Stainless Steel	Autoclave Engineers	2 Way 1/8" Isolation Valve
15	10V2081	11000 psig	Stainless Steel	Autoclave Engineers	2 Way 1/8" Isolation Valve
16	ST2220	11000 psig	Stainless Steel	Autoclave Engineer	Tee - 1/8"
17		15000 psig	Stainless Steel	Metal Men	0.125" x .035" Tubing
19		15000 psig	Stainless Steel	Metal Men	0.125" x .035" Tubing
20		15000 psig	Stainless Steel	Metal Men	0.125" x .035" Tubing
21	AG-152	20000 psig	Carbon Steel	Haskel	Gas Booster Pump
22	15M42B1	60000 psig	Stainless Steel	Autoclave Engineers	1/4" High Pressure to 1/8" SpeedBite
23	AMFLO 2100	150 psig	Steel	Bridge Products Inc	Single Stage Gas Regulator
26	15M42B1	60000 psig	Stainless Steel	Autoclave Engineers	1/4" High Pressure to 1/8" SpeedBite
27	15M42B1	60000 psig	Stainless Steel	Autoclave Engineers	1/4" High Pressure to 1/8" SpeedBite
28	P605-X	22500 psig	17-4 PH SS	Omega Engineering	0-15000 psig Transducer
29	P605-X	22500 psig	17-4 PH SS	Omega Engineering	0-15000 psig Transducer
30	15-63AF2	15000 psig	Stainless Steel	High Pressure Equipment	1/8" Tee Type Safety Head
31		15000 psig	Stainless Steel	Metal Men	0.125" x .035" Tubing
32		15000 psig	Stainless Steel	Metal Men	0.125" x .035" Tubing
33	10V2	11000 psig	Stainless Steel	Autoclave Engineers	Air-To-Close Diaphragm Valve
35	KIP 141161	100 psid	Brass	Minuteman Controls	Three Way Solenoid Valve
36		15000 psig	Stainless Steel	Metal Men	0.125" x .035" Tubing
37	10V2081	11000 psig	Stainless Steel	Autoclave Engineers	2 Way 1/8" Isolation Valve
43	2-4 FBZ-SS	7500 psig	Stainless Steel	Parker	1/4" MPT to 1/8" CPI Male Connector
45	8-6 MHN-B	3900 psig	Brass	Parker	1/2 MPT to 3/8 MPT Hex Nipple
46		150 psig	Brass		Solenoid Operated Two Way Valve
47	6-6 FBZ-SS	7200 psig	Stainless Steel	Parker	3/8" MPT to CPI Male Connector
48		10000 psig	Stainless Steel	Metal Men	0.25" x .065" Tubing
49		3000 psig	Nitrogen, Grade 4.8	Middlesex Gas	200 cuft Nitrogen Tank, Grade 4.8, w/Connector
50	4-4-4 FT-SS	5600 psig	Stainless Steel	Parker	1/4" FPT Female Tee
51		3000 psig	Brass Case		0-3000 psig Gage
52	FC372-03	3000 psig	Polyon	Aeroquip	Polyon High Pressure Gas Line
53	2-4 GBZ-SS	10000 psig	Stainless Steel	Parker	1/4" FPT to 1/8" CPI Female Connector
54		15000 psig	Stainless Steel	Metal Men	0.125" x .035" Tubing
62		10000 psig	Stainless Steel	Metal Men	0.25" x .065" Tubing
64		15000 psig	Stainless Steel	Metal Men	0.125" x .035" Tubing
65	2-4 FBZ-SS	7500 psig	Stainless Steel	Parker	1/4" MPT to 1/8" CPI Male Connector
66		10000 psig	Stainless Steel Fit	Boston Hydraulics	Non-Conductive High Pressure Hydraulic Hose
67			Alloy 600	Custom	Alloy 600 Sample
68	2-4 FBZ-SS	7500 psig	Stainless Steel	Parker	1/4" MPT to 1/8" CPI Male Connector
69		100psig@315C	Nickel-200	High Pressure Equipment	Autoclave w/ Cooling Jackets on Standoffs

Table A-3-2: Sample Pressurization System Component ID

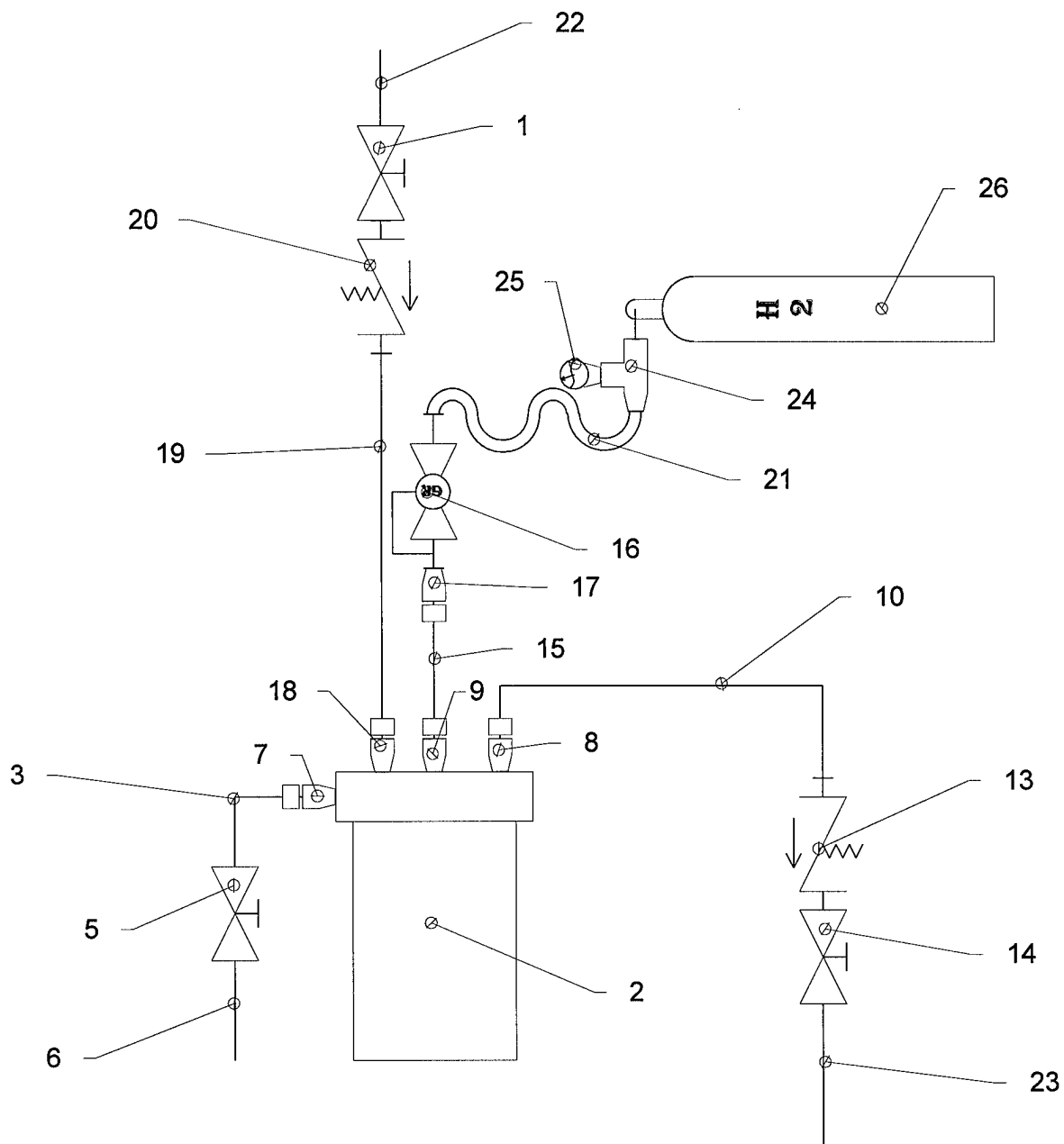


Figure A-3-6: Static System Component ID

Static System Component Identification List					
UID	Part Number	MAWP	Material	Manufacturer	Description
1	4Z(A)-B2LJ2-SSP	6000psig	Stainless Steel	Parker	Two Way Ball Valve - 1/4" CPI Fittings
2			Titanium	Autoclave Engineer	Autoclave - 4 liter
3		10000 psig	Stainless Steel	Metal Men	0.25" x 0.065" Tubing
5	4Z(A)-B2LJ2-SSP	6000 psig	Stainless Steel	Parker	Two Way Ball Valve - 1/4" CPI Fittings
6		10000 psig	Stainless Steel	Metal Men	0.25" x 0.065" Tubing
7	4-4 FBZ-SS	10000 psig	Stainless Steel	Parker	1/4" Male Connector
8	4-4 FBZ-SS	10000 psig	Stainless Steel	Parker	1/4" Male Connector
9	4-4 FBZ-SS	10000 psig	Stainless Steel	Parker	1/4" Male Connector
10		10000 psig	Stainless Steel	Metal Men	0.25" x 0.065" Tubing
13	4Z(A)-CO4L-10-V-SS	6000 psig	SS/Viton	Parker	O-Ring Poppet Check Valve
14	4Z(A)-B2LJ2-SSP	6000psig	Stainless Steel	Parker	Two Way Ball Valve - 1/4" CPI Fittings
15		10000 psig	Stainless Steel	Metal Men	0.25" x 0.065" Tubing
16		6000 psig	Stainless Steel	Grove	Gas Regulator
17	4-4 FBZ-SS	10000 psig	Stainless Steel	Parker	1/4" Male Connector
18	4-4 FBZ-SS	10000 psig	Stainless Steel	Parker	1/4" Male Connector
19		10000 psig	Stainless Steel	Metal Men	0.25" x 0.065" Tubing
20	4Z(A)-CO4L-10-V-SS	6000 psig	SS/Viton	Parker	O-Ring Poppet Check Valve
21		10000 psig	Stainless Steel Fit	Boston Hydraulics	Non-Conductive High Pressure Hydraulic Hose
22		10000 psig	Stainless Steel	Metal Men	0.25" x 0.065" Tubing
23		10000 psig	Stainless Steel	Metal Men	0.25" x 0.065" Tubing
24		10000 psig	Stainless Steel	Boston Hydraulics	1/4" Street Tee -Hydraulic Fitting
25		10000 psig	Stainless Steel	Boston Hydraulics	0-10000 psig Liquid Gage
26		6000 psig	Hydrogen	Middlesex Gas	500 cuft Grade 5 Hydrogen Tank with Connector

Table A-3-3 : Static System Component Identification

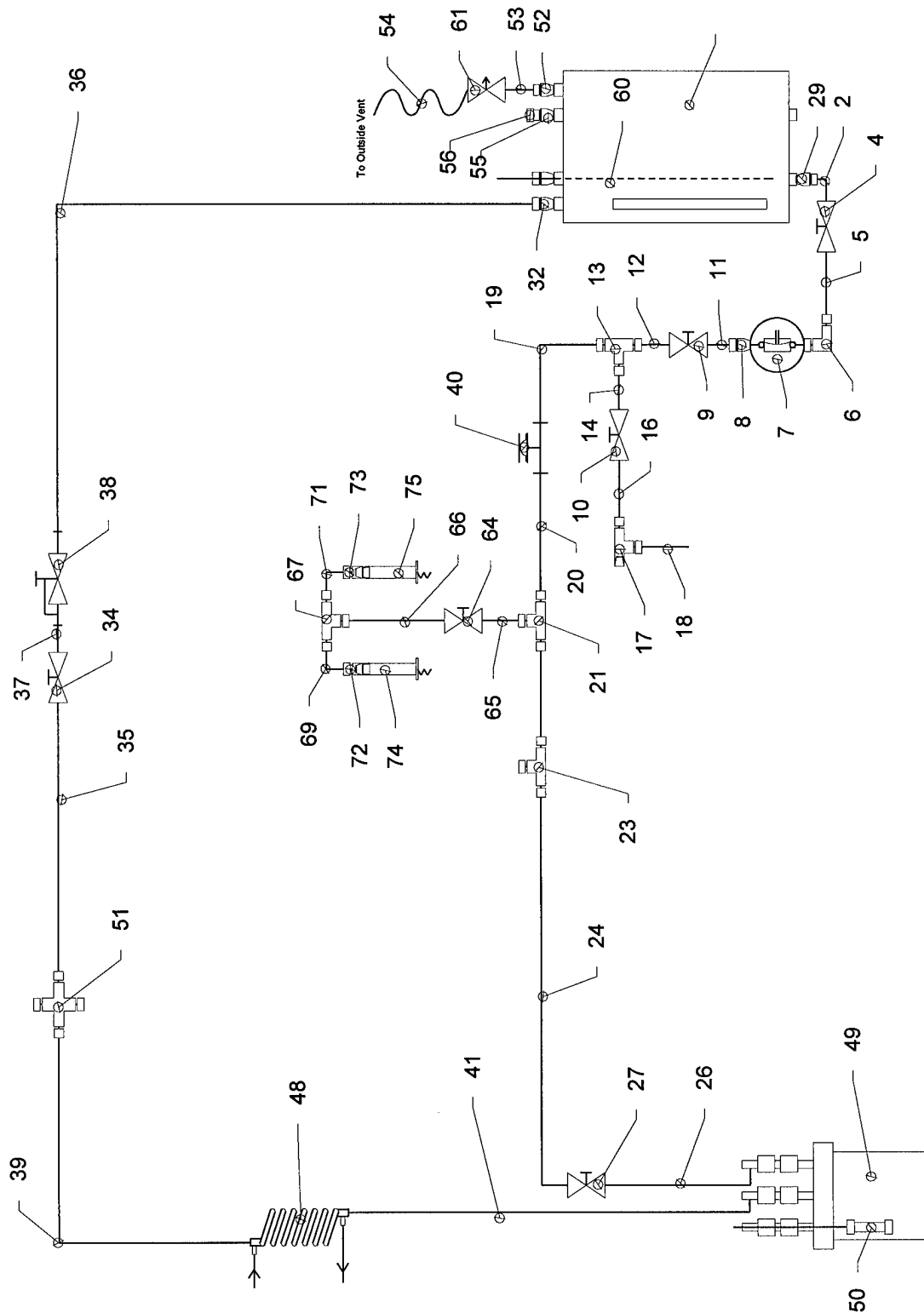


Figure A-3-7 : Recirculation System Component ID

Recirculation System Component Identification List					
UID	Part Number	MAWP	Material	Manufacturer	Description
1		10 psig	Stainless Steel	Custom	200 Liter Storage Tank w/ Sight Glass
2		10000 psig	Stainless Steel	Metal Men	0.25" x 0.065" Tubing
4	4Z(A)-B2LJ2-SSP	6000psig	Stainless Steel	Parker	Two Way Ball Valve - 1/4" CPI Fittings
5		10000 psig	Stainless Steel	Metal Men	0.25" x 0.065" Tubing
6	4-4 EBZ-SS	10000 psig	Stainless Steel	Parker	1/4" CPI/A-Lok Union Elbow
7	680-S-E	3000psig	Stainless Steel/PTF	Pulsa Feeder	Diaphragm Recirculation Pump
8	4-4 FBZ-SS	10000 psig	Stainless Steel	Parker	1/4" Male Connector
9	4Z(A)-B2LJ2-SSP	6000psig	Stainless Steel	Parker	Two Way Ball Valve - 1/4" CPI Fittings
10	4Z(A)-B2LJ2-SSP	6000psig	Stainless Steel	Parker	Two Way Ball Valve - 1/4" CPI Fittings
11		10000 psig	Stainless Steel	Metal Men	0.25" x 0.065" Tubing
12		10000 psig	Stainless Steel	Metal Men	0.25" x 0.065" Tubing
13	4-4-4 JBZ-SS	10000psig	Stainless Steel	Parker	1/4 CPI/A-Lok Union Tee
14		10000 psig	Stainless Steel	Metal Men	0.25" x 0.065" Tubing
15		10000 psig	Stainless Steel	Metal Men	0.25" x 0.065" Tubing
16		10000 psig	Stainless Steel	Metal Men	0.25" x 0.065" Tubing
17	4-4-4 MBZ-SS	10000 psig	Stainless Steel	Parker	1/4" Female Run Tee
18		10000 psig	Stainless Steel	Metal Men	0.25" x 0.065" Tubing
19		10000 psig	Stainless Steel	Metal Men	0.25" x 0.065" Tubing
20		10000 psig	Stainless Steel	Metal Men	0.25" x 0.065" Tubing
21	4-4-4 JBZ-SS	10000psig	Stainless Steel	Parker	1/4 CPI/A-Lok Union Tee
22		10000 psig	Stainless Steel	Metal Men	0.25" x 0.065" Tubing
23	4-4-4 JBZ-SS	10000psig	Stainless Steel	Parker	1/4 CPI/A-Lok Union Tee
24		10000 psig	Stainless Steel	Metal Men	0.25" x 0.065" Tubing
26		10000 psig	Stainless Steel	Metal Men	0.25" x 0.065" Tubing
27	4Z(A)-B2LJ2-SSP	6000psig	Stainless Steel	Parker	Two Way Ball Valve - 1/4" CPI Fittings
29	4-8 FBZ-SS	6600 psig	Stainless Steel	Parker	1/2" MPT to 1/4"CPI/A-Lok Male Connector
32	4-4 FBZ-SS	10000 psig	Stainless Steel	Parker	1/4" Male Connector
34	4Z(A)-B2LJ2-SSP	6000psig	Stainless Steel	Parker	Two Way Ball Valve - 1/4" CPI Fittings
35		10000 psig	Stainless Steel	Metal Men	0.25" x 0.065" Tubing
36		10000 psig	Stainless Steel	Metal Men	0.25" x 0.065" Tubing
37		10000 psig	Stainless Steel	Metal Men	0.25" x 0.065" Tubing
38	Series 1700	3000 psig	Stainless Steel	Tescom	Backpressure Regulator
39		10000 psig	Stainless Steel	Metal Men	0.25" x 0.065" Tubing
40	10-63AF4	10000 psig	Stainless Steel	High Pressure Equipment	1/4" Tee Type Safety Head
41		10000 psig	Stainless Steel	Metal Men	0.25" x 0.065" Tubing
48	N/A	10000 psig (l)	SS/Copper	Custom	Cooling Coil
49		100psig@315C	Nickel-200	High Pressure Equipment	Autoclave w/ Cooling Jackets on Standoffs
50			Alloy 600	Custom	Alloy 600 Sample
51	4-KBZ-SS	10000 psig	Stainless Steel	Parker	Union Cross - 1/4" CPI fittings
52	4-6 FBZ-SS	7200 psig	Stainless Steel	Parker	3/8"MPT to 1/4"CPI Male Connector
53		10000 psig	Stainless Steel	Metal Men	0.25" x 0.065" Tubing
54		200 psig	PolyEthylene		1/4" OD Plastic Tube
55	4-6 FBZ-SS	7200 psig	Stainless Steel	Parker	3/8"MPT to 1/4"CPI Male Connector
56	4 FNZ-SS	10000 psig	Stainless Steel	Parker	1/4" CPI Plug
60		10000 psig	Stainless Steel	Metal Men	0.25" x 0.065" Tubing
61	4Z(A)-V2LN-SS	5000 psig	Stainless Steel	Parker	1/4 Tube CPI General Purpose Needle Valve
62	6-6 FBZ-SS	7200 psig	Stainless Steel	Parker	3/8" MPT to CPI Male Connector
64	4Z(A)-B2LJ2-SSP	6000psig	Stainless Steel	Parker	Two Way Ball Valve - 1/4" CPI Fittings
65		10000 psig	Stainless Steel	Metal Men	0.25" x 0.065" Tubing
66		10000 psig	Stainless Steel	Metal Men	0.25" x 0.065" Tubing
67	4-4-4 JBZ-SS	10000psig	Stainless Steel	Parker	1/4 CPI/A-Lok Union Tee
69		10000 psig	Stainless Steel	Metal Men	0.25" x 0.065" Tubing
71		10000 psig	Stainless Steel	Metal Men	0.25" x 0.065" Tubing
72	4-4 GBZ-SS	5600 psig	Stainless Steel	Parker	1/4"FPT to 1/4"CPI/A-Lok Female Connector
73	4-4 GBZ-SS	5600 psig	Stainless Steel	Parker	1/4"FPT to 1/4"CPI/A-Lok Female Connector
74	P605-X	4500 psig	17-4 PH SS	Omega Engineering	0-3000psig Transducer
75	P605-X	4500 psig	17-4 PH SS	Omega Engineering	0-3000psig Transducer

Table A-3-4 : Recirculation System Component ID

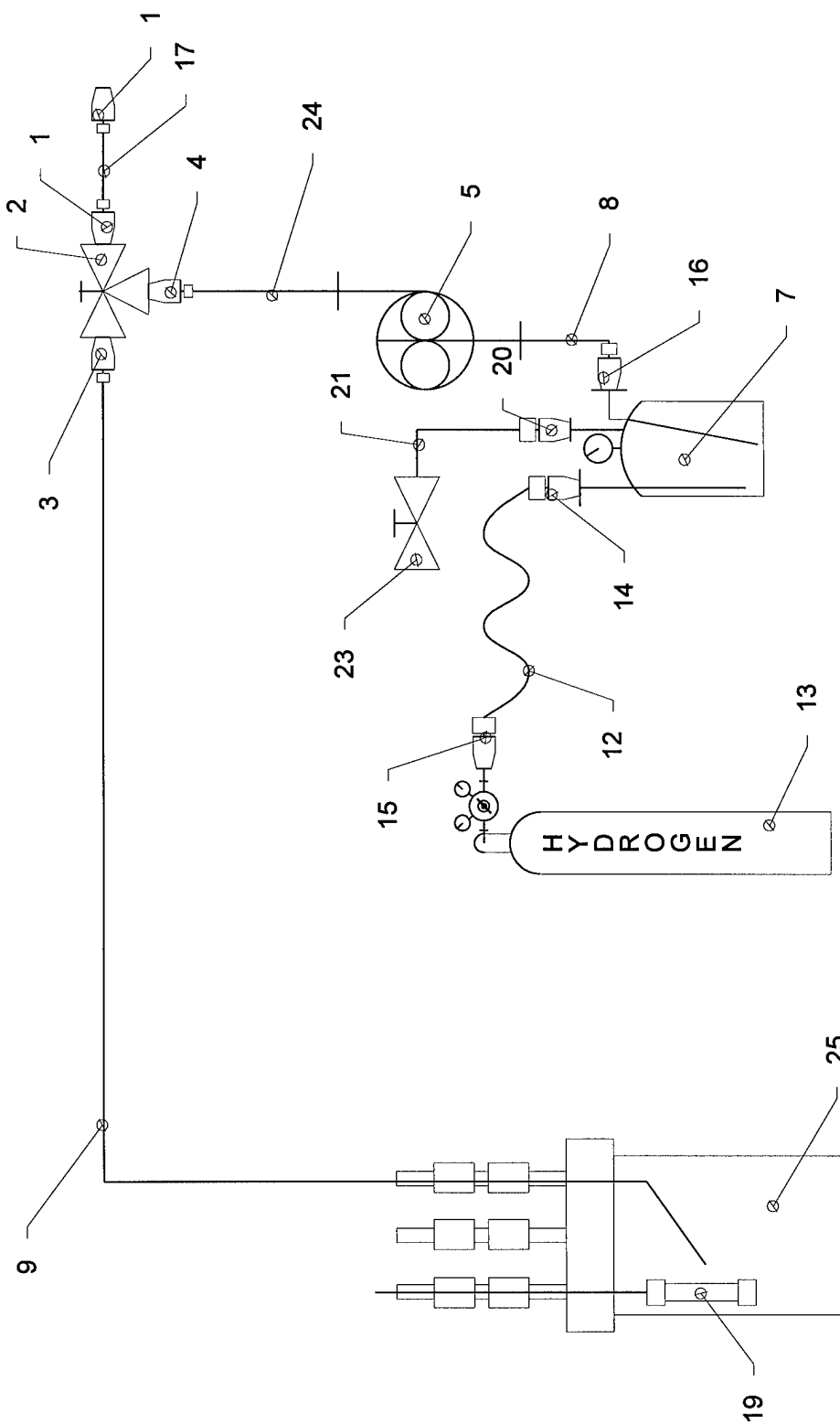


Figure A-3-8: Injection System Component ID

Injection System Component Identification List					
UID	Part Number	MAWP	Material	Manufacturer	Description
1	1-4 FBZ-SS	10000 psig	Stainless Steel	Parker	Male Connector - 1/4"MPT to 1/16"CPI/A-Lok
2	4F-B6XS2-SSP	6000psig	Stainless Steel	Parker	Three Way Spring Loaded Ball Valve
3	1-4 FBZ-SS	10000 psig	Stainless Steel	Parker	Male Connector - 1/4"MPT to 1/16"CPI/A-Lok
4	1-4 FBZ-SS	10000 psig	Stainless Steel	Parker	Male Connector - 1/4"MPT to 1/16"CPI/A-Lok
5	396-89	5000psig	Stainless Steel	LDC Analytical	MiniPump Metering Pump
6		15000 psig	Stainless Steel	Metal Men	0.125" x .035" Tubing
7		130 psig	Stainless Steel		9 liter SS Injection Tank
8		15000 psig	Stainless Steel	Metal Men	0.125" x .035" Tubing
12		200 psig	PolyEthylene		1/4" OD Plastic Tube
13		2000 psig	Hydrogen, Grade 5	Middlesex Gas	200 cuft Hydrogen w/ 2 Stage Reg
14	4-4 FBZ-SS	10000 psig	Stainless Steel	Parker	1/4" Male Connector
15	4-4 FBZ-SS	10000 psig	Stainless Steel	Parker	1/4" Male Connector
16	2-4 FBZ-SS	7500 psig	Stainless Steel	Parker	1/4" MPT to 1/8" CPI Male Connector
17		15000 psig	Stainless Steel	High Pressure Equipment	0.063" x 0.020" Tubing
18	1-4 FBZ-SS	10000 psig	Stainless Steel	Parker	Male Connector - 1/4"MPT to 1/16"CPI/A-Lok
19			Alloy 600	Custom	Alloy 600 Sample
20	4-4 FBZ-SS	10000 psig	Stainless Steel	Parker	1/4" Male Connector
21		10000 psig	Stainless Steel	Metal Men	0.25" x .065" Tubing
23	4Z(A)-B2LJ2-SSP	6000psig	Stainless Steel	Parker	Two Way Ball Valve - 1/4" CPI Fittings
24		15000 psig	Stainless Steel	High Pressure Equipment	0.063" x 0.020" Tubing
25		100psig@315C	Nickel-200	High Pressure Equipment	Autoclave w/ Cooling Jackets on Standoffs

Table A-3-5 : Injection System Component ID

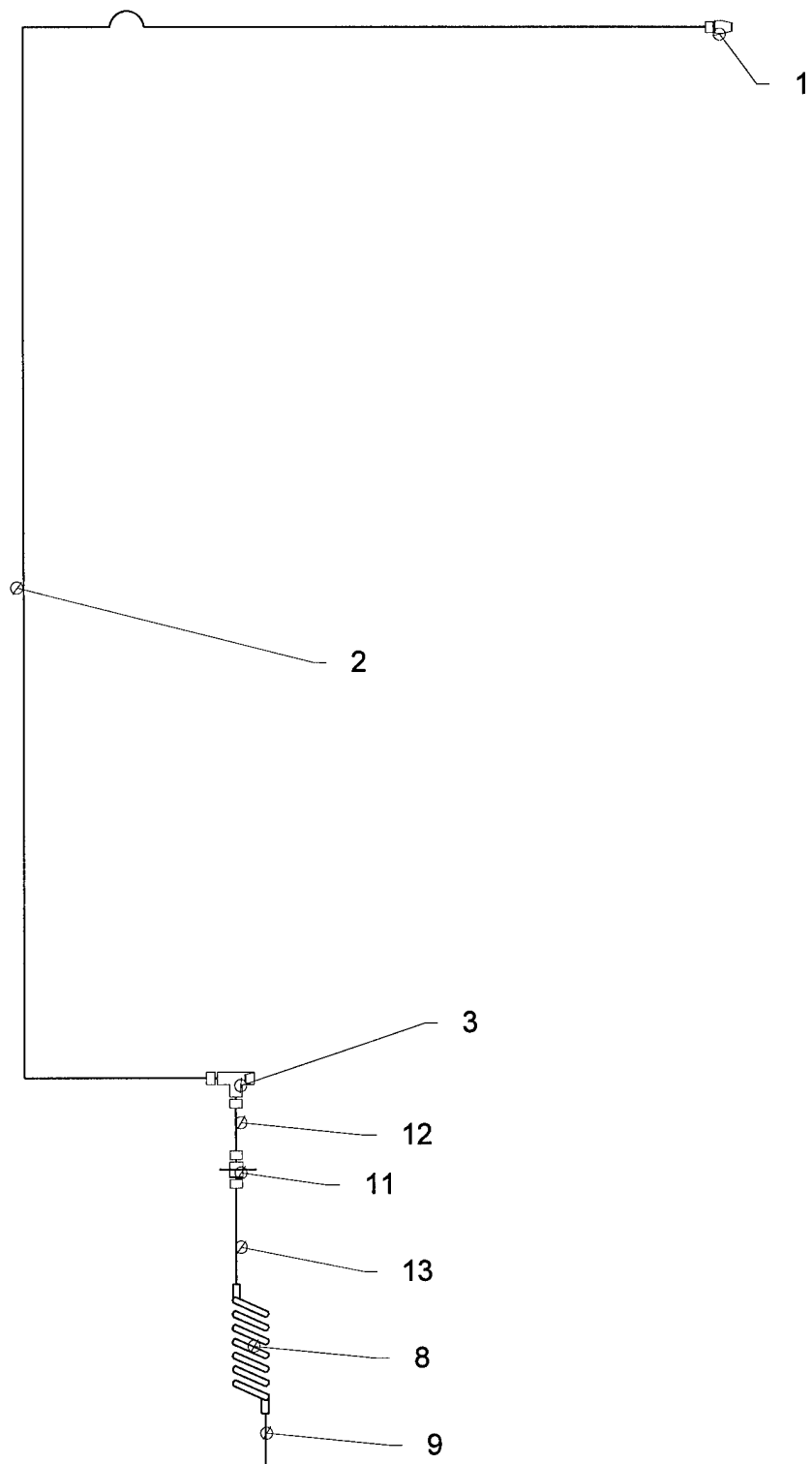


Figure A-3-9: Emergency Depressurization and Safety Collection System  
Component ID



Depressurization and Safety Collection System Component Identification List					
UID	Part Number	MAWP	Material	Manufacturer	Description
1	4-6 FBZ-SS	7200 psig	Stainless Steel	Parker	3/8"MPI to 1/4"CPI Male Connector
2		10000 psig	Stainless Steel	Metal Men	0.25" x 0.065" Tubing
3	4-4-4 MBZ-SS	10000 psig	Stainless Steel	Parker	1/4" Female Run Tee
8			Copper	Custom	Single Element Cooling Coil
9		10000 psig	Stainless Steel	Metal Men	0.25" x 0.065" Tubing
11	4-4 WBZ-SS	10000 psig	Stainless Steel	Parker	1/4 Bulkhead Union
12		10000 psig	Stainless Steel	Metal Men	0.25" x 0.065" Tubing
13		10000 psig	Stainless Steel	Metal Men	0.25" x 0.065" Tubing

Table A-3-6: Depressurization and Safety Collection System Component ID

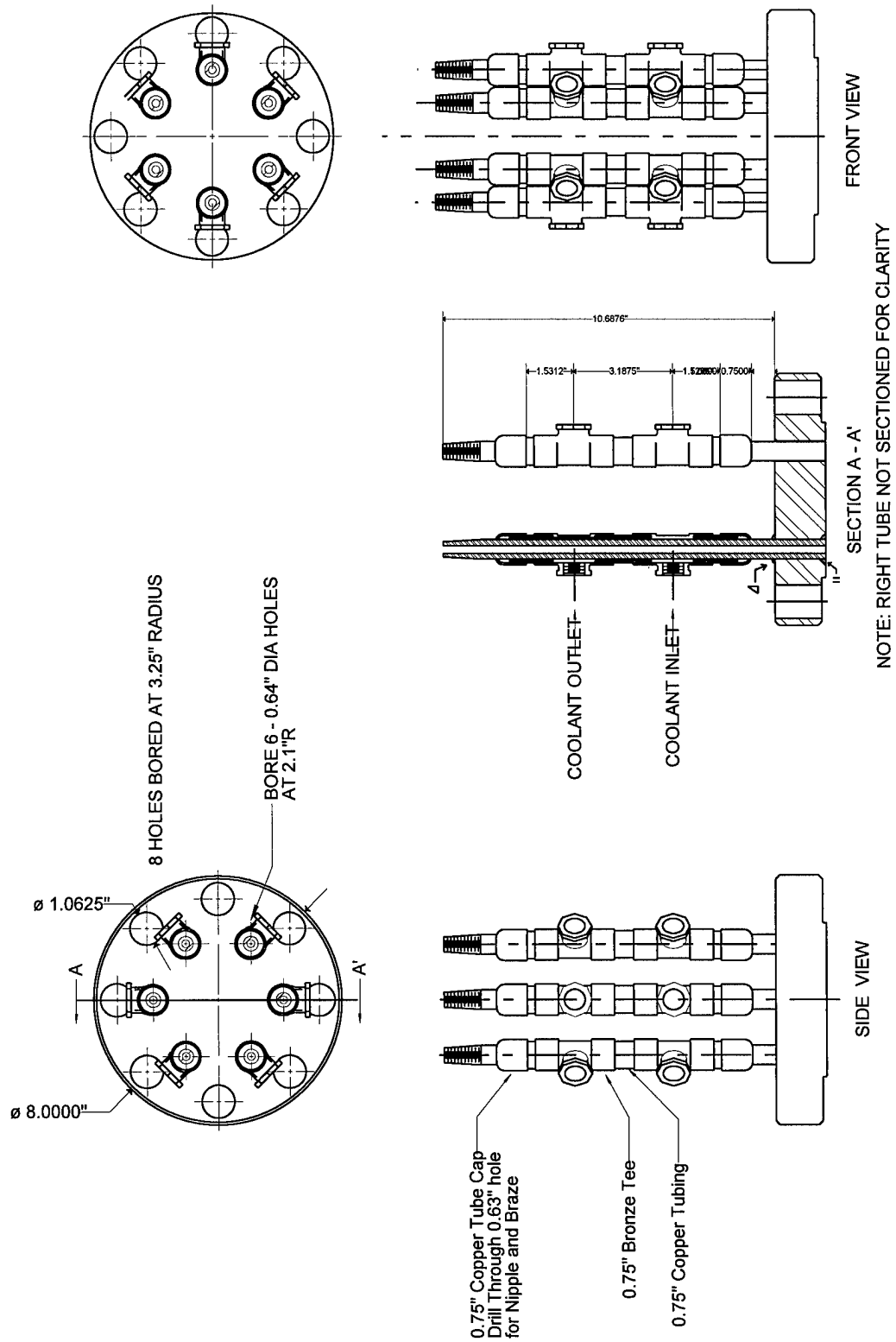


Figure A-3-10: Autoclave Head Detail

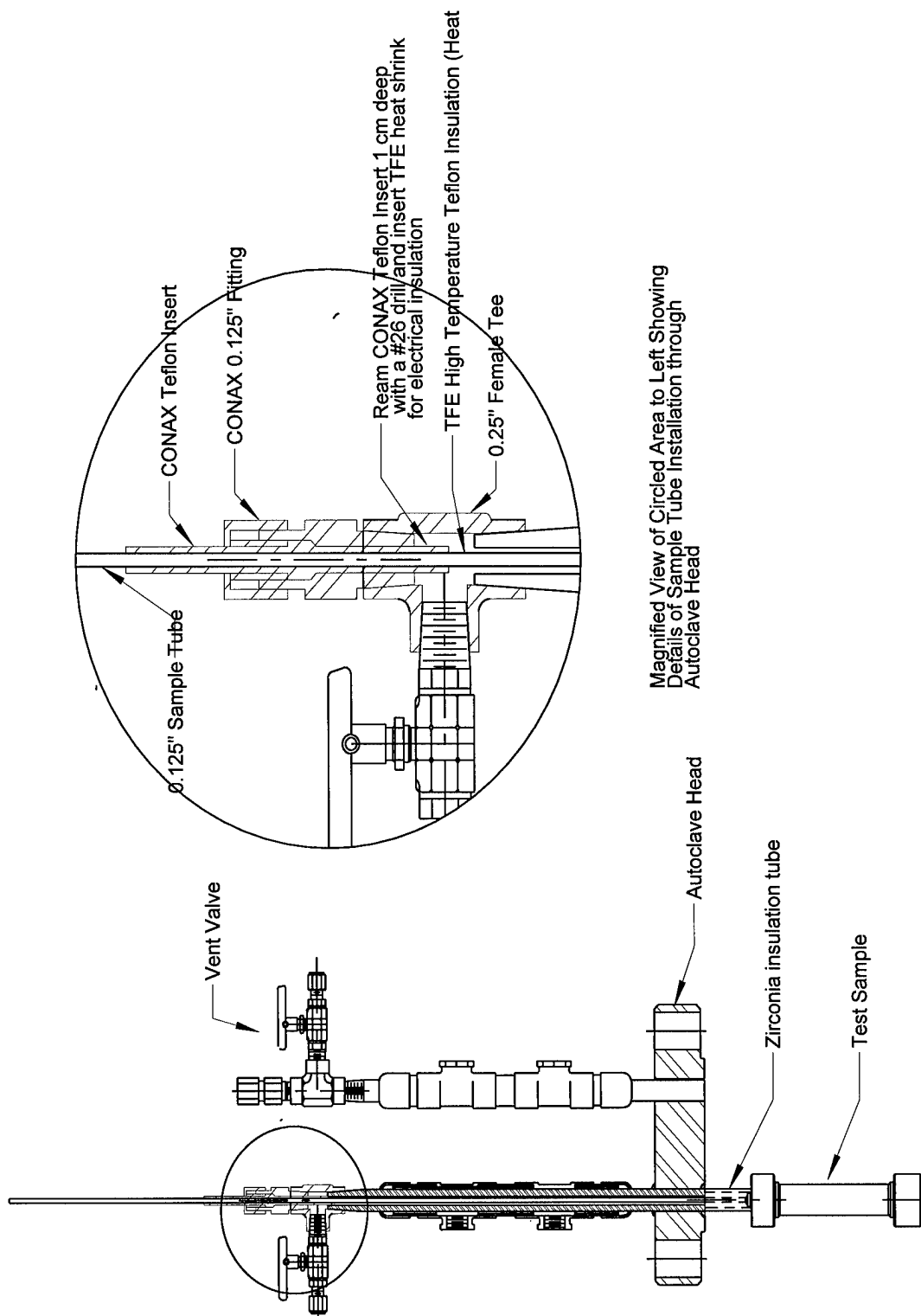


Figure A-3-11: Autoclave Head and Sample Assembly Detail

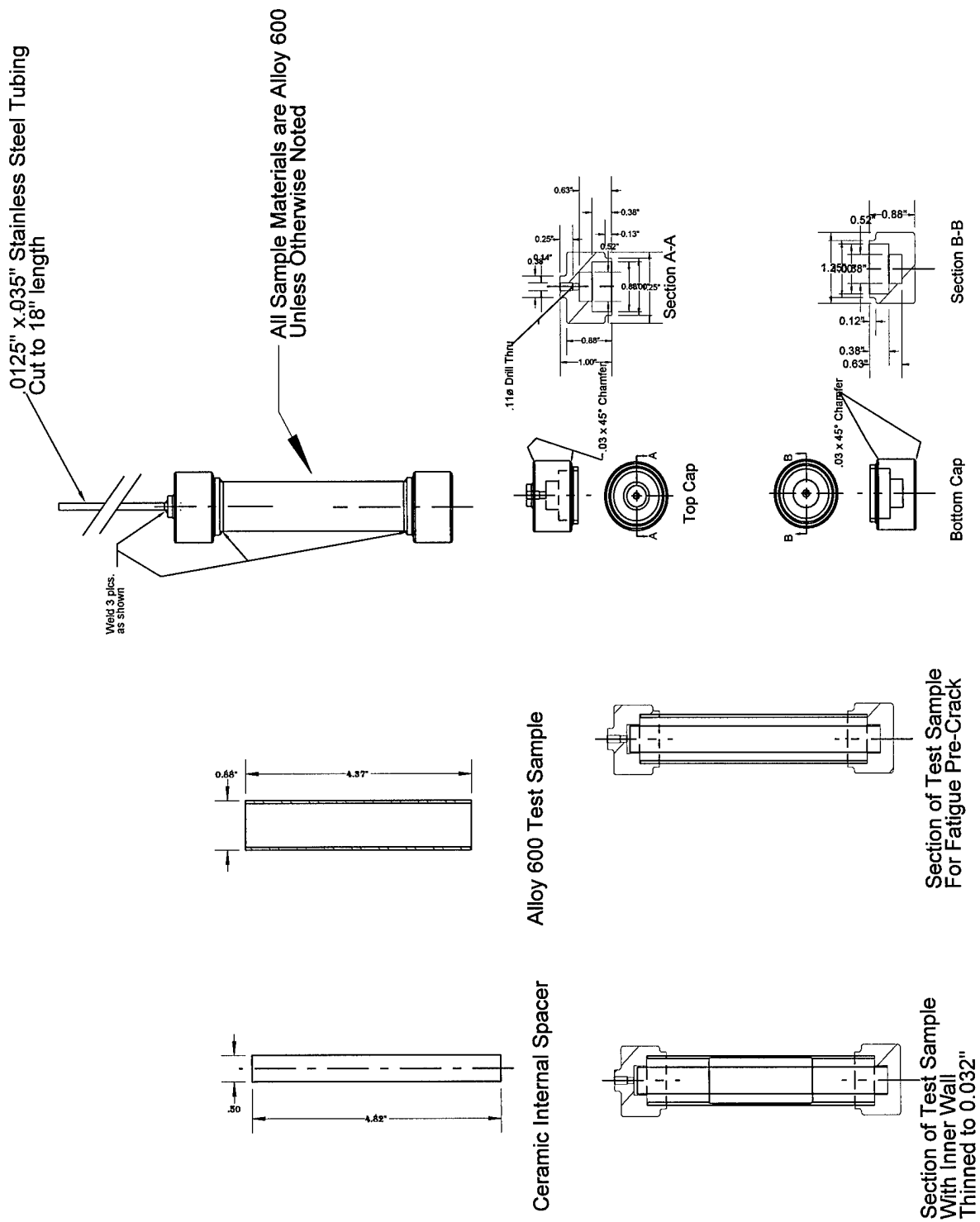


Figure A-3-12: Test Sample Assembly Detail

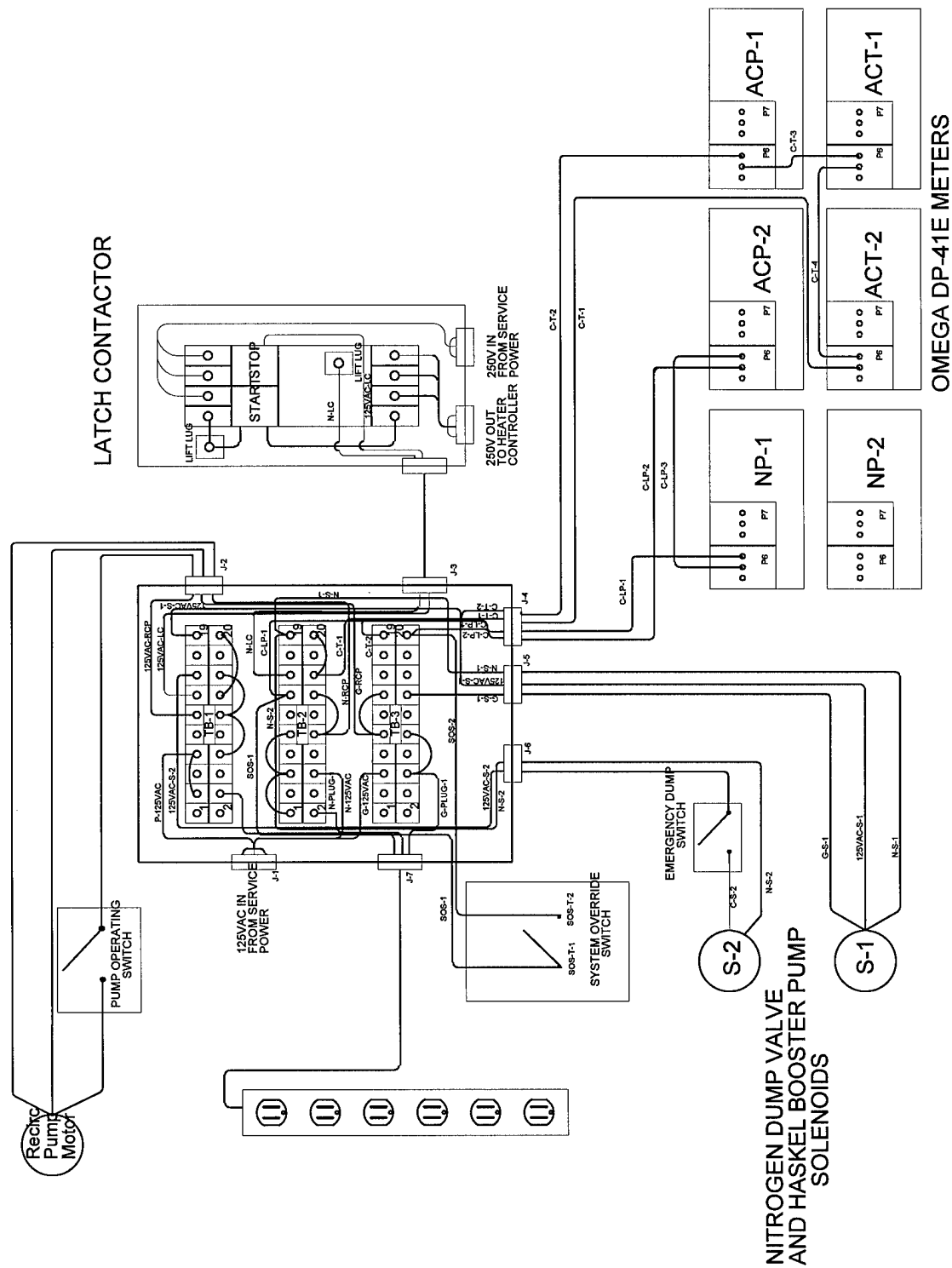


Figure A-3-13: Detailed Control Wiring Schematic

Alloy 600 Autoclave System Control System Wiring			
Wire Nomenclature	Terminal From	Terminal To	Description
P-125VAC	J-1	TB-1-7	125 VAC Hot Wire Input Lead
N-125VAC	J-1	TB-2-6	125 VAC Neutral Input Lead
G-125VAC	J-1	TB-3-5	System Ground
125VAC-RCP	TB-1-11	J-2	125VAC Service to RCP Via Switch
N-RCP	TB-2-10	J-2	Neutral Lead to RCP
G-RCP	TB-3-9	J-2	Ground to RCP
125VAC-LC	TB-1-13	J-3	125VAC Service Power to Latch Contactor
N-LC	TB-2-15	J-3	Neutral to Latch Contactor
125VAC-S-1	TB-1-19	J-5	125VAC Service Power to Solenoid S-1(Haskell Pump Air Shutoff)
N-S-1	TB-2-19	J-5	Neutral Lead to Solenoid S-1(Haskell Pump Air Shutoff)
G-S-1	TB-3-14	J-5	Ground for Solenoid S-1 (Haskell Pump Air Shutoff)
125VAC-PLUG-1	TB-1-4	J-7	125VAC Service Power to Power Strip
N-PLUG-1	TB-2-2	J-7	Neutral Lead to Power Strip
G-PLUG-1	TB-3-6	J-7	Ground to Power Strip
SOS-1	TB-2-13	SOS-T-1	Control Lead to System Override Switch
SOS-2	TB-3-20	SOS-T-2	Control Lead to System Override Switch
125VAC-S-2	TB-1-15	J-6	125VAC Service Power to Solenoid S-2
N-S-2	TB-2-19	J-6	Neutral to Solenoid S-2
C-LP-1	TB-2-13	ACP-2(P6)-COM	Control Lead to P6-COM on Meter ACP-2 via Jack J-6
C-LP-2	TB-3-20	NP-1(P6)-NC	Control Lead to P6-NC on Meter NP-1 via Jack J-6
C-LP-3	ACP-2(P6)-NC	NP-1(P6)-COM	Series Jumper from NC Terminal on Meter ACP-2 to COM on Meter NP-1
C-T-1	TB-2-16	ACT-2(P6)-COM	Control Lead to P6-COM on Meter ACT-2 via Jack J-6
C-T-3	ACP-1(P6)-COM	ACT-1(P6)-NC	Series Jumper from COM Terminal on Meter ACP-1 to NC on Meter ACT-1
C-T-4	ACT-1(P6)-COM	ACT-2(P6)-NC	Series Jumper from COM Terminal on Meter ACT-1 to NC on Meter ACT-2
C-T-2	TB-3-19	ACP-1(P6)-NC	Control Lead to P6-NC on Meter ACP-1 via Jack J-6

Table A-3-7: Control System Wiring Detail

#### A-4. Axial Fatigue Pre-crack Sample Preparation Procedure

Initiation times for SCC were found to be considerably shorter if the localized stress were increased. Axial fatigue cracks initiated in the test area provide the required localized stress and a crevice from which SCC can occur and grow. In order to evaluate fatigue growth in real time, the fatigue crack must initiate at 90 degrees to the applied load. However, calculations using MATHCAD®'s Roark's Formulas for Stress and Strain on a tube sample show stress levels are a factor of 1.7 times greater on the inside wall immediately under the point of load application than at 90 degrees to the point of application. Several early tests demonstrated this when axial fatigue cracks occurred and grew through-wall directly under the line of load application.

The stress at 90 degrees to the applied load was increased beyond that directly under the load application point by machining a thin notch 90 degrees to the load line with a DREMEL® tool and a 0.875 inch by 0.015 inch cutoff wheel. The depth of the notch can be estimated using figure A-4-1. Typical depths to initiate fatigue cracks at 90 degrees to the load line vice under the load line ranged from .030" to 0.035" in the Low Temperature Annealed Alloy 600 Heat 96834. Fatigue crack growth is induced by applying 90 percent of the yield stress load (approximately 1000 pounds) at 90 degrees to the machined notch in an MTS Model 810 Material Test System. To ensure even loading, the sample is held in a fixture illustrated in figure A-4-2. The MTS Test System is operated in a sinusoidal mode with minimum loading not less than 50 pounds compressive to prevent sample movement. Figures A-4-3 and A-4-4 illustrate the actual test setup. Initiation of fatigue cracking is noted at the edges of the machined notch

using a stroboscope and microscope to monitor the notch area. Typical growth should not exceed 0.1 mm to prevent excessive through wall crack growth and typically occurs in under  $10^6$  cycles.

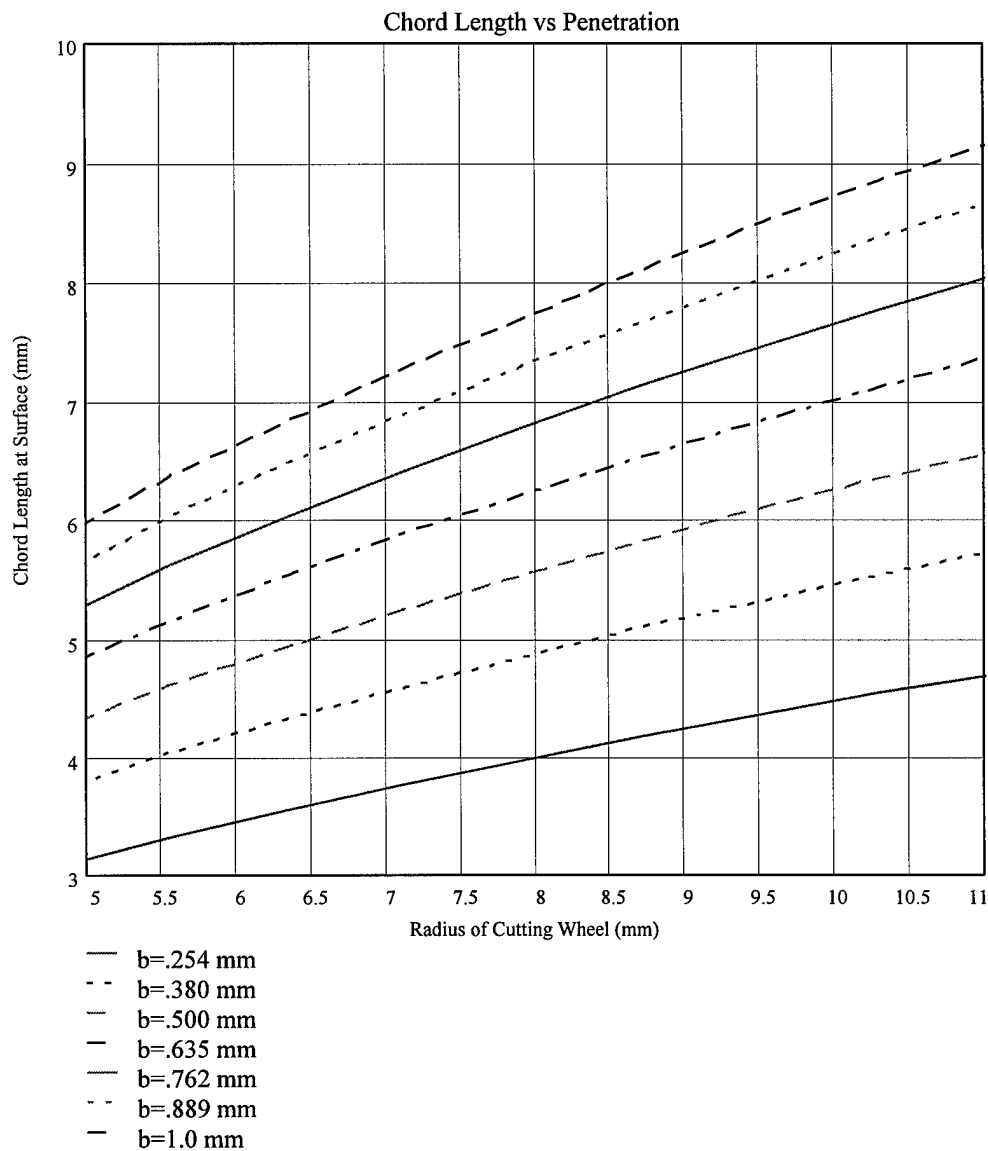


**Figure A-4-1: Notch Depth versus Surface Chord Length**



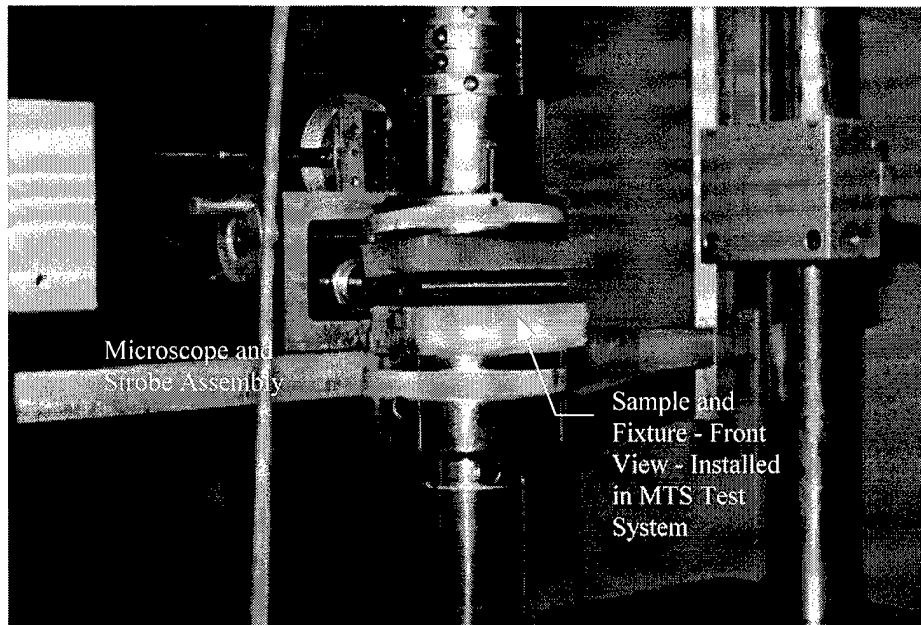


Figure A-4-4: Front View of Sample and Fixture Installed in MTS Test System

#### A-5. Error Analysis

An error analysis was performed on the crack growth rate and stress intensity data obtained from the tube tests. The errors associated with crack growth rates and stress intensity are illustrated in Section 6 (Discussion) and presented in Table A-5-1 below.

Errors associated with the stress intensity calculations consisted of analytical errors from the finite element analysis used to calculate the stress intensity. The estimated error associated with this analysis is  $\pm 5\%$ <sup>1</sup>. The plotted error bars in Figures 6-3 and 6-4 represent the range of stress intensities throughout the crack growth period with the upper and lower limits accounting for the 5% analytical error. Crack growth from a free surface is assumed to be dependent on  $K_I$  when stress intensities reach a value of 4 MPa $\sqrt{m}$ <sup>2</sup> and have no associated analytical error.

The error in the crack growth rate is primarily a function of determining the initiation time from the ACPD output. The determination of the initiation times is discussed in detail in section 5 (Results). However, in the case of surface crack initiation, the sensitivity of the ACPD may preclude detecting initiation until a large enough crack has propagated into the wall. Therefore, the worse case is initiation from time 0. The lower values of crack growth for

---

<sup>1</sup> J. C. Newman Jr., and I.S. Raju, "An Empirical Stress Intensity Factor Equation for the Surface Crack," *Engineering Fracture Mechanics*, Vol. 15, No. 1-2 (Great Britain: 1981), pp. 185-192.

<sup>2</sup> Electric Power Research Institute, *Steam generator Reference Handbook*, EPRI TR-103824, Project 2895;4044 Nuclear Power Group (Palo Alto: EPRI, Dec 1994), p. 13-26.

the first series of data reflects this estimate. However, the rise in potential on the 10kHz signal is most likely the upper limit and this is the plotted value, so there is no associated upper error.

In the case of the pre-fatigued samples with multiple growth areas, the average growth rate was plotted from visual measurements of the upper and lower bounds of each region. These upper and lower bounds are then used to determine the upper and lower growth rate errors.

Alloy 600 Test Data with Error Limits										
Test	K (lower)	K (upper)	K (avg)	(-) Error	(+) Error	dA/dt (Average)	dA/dt (lower)	dA/dt (upper)	(-) Error	(+) Error
950909C	4	7.3	5.7	1.7	2.0	1.6	1.1	11.2	0.5	0
950909C	4	9.2	6.6	2.6	3.1	2	1.3	13.6	0.7	0
950909C	4	8.3	6.2	2.2	2.6	2.1	1.4	14.1	0.7	0
950909C	4	9.1	6.6	2.6	3.0	2.3	1.5	15.6	0.8	0
950909C	4	15.3	9.7	5.7	6.4	2.7	1.8	18.5	0.9	0
960212	11.9	12.6	12.3	0.9	1.0	3.6	1.8	5.9	1.8	2.3
960212	12.6	22.8	17.7	5.7	6.2	14.2	10.1	17.4	4.1	3.2

Table A-5-1 : Test Data with Error Calculations